STUDY OF ISOSPIN EFFECTS IN HEAVY-ION COLLISION AT INTERMEDIATE ENERGIES

A THESIS

submitted to the

THAPAR UNIVERSITY, PATIALA

for the degree of

DOCTOR OF PHILOSOPHY

IN THE FACULTY OF SCIENCE

By

Rajni

Regn. No. 900912013

SCHOOL OF PHYSICS AND MATERIALS SCIENCE

THAPAR UNIVERSITY

PATIALA-147004, PUNJAB, (INDIA)

Dedicated with love to my parents and husband

THAPAR UNIVERSITY, PATIALA

CANDIDATE'S DECLARATION

I hereby certify that the work which is being presented in this thesis entitled "**STUDY OF ISOSPIN EFFECTS IN HEAVY ION COLLISIONS AT INTERMEDIATE ENERGIES**" in partial fulfillment of the requirements for the award of Degree of Doctor of Philosophy and submitted in the School of Physics and Materials Science, Thapar University, Patiala, is an authentic record of the my own work carried out during a period from January 2010 to June 2012 under the supervision of **Dr. Suneel Kumar**, Associate Professor, Thapar University Patiala and **Professor Rajeev Kumar Puri**, Department of Physics, Panjab University Chandigarh.

The matter presented in this thesis has not been submitted by me for the award of any other degree of this or any other university/institute.

Rajni

(Rajni)

This is to certify that the above statement made by the candidate is correct to the best of our knowledge.

S Kumar 26/10/12

Dr. Suneel Kumar

(Supervisor)

Prof. Dr. Rajeev K. Puri

(Co-Supervisor)

Signature of HOD

Signature of Dean R & SP

Signature of External Examiner

Date: 26/10/12

Acknowledgments

I would like to express my respectful thanks to my principal advisor **Dr. Suneel Kumar** *Associate Professor, Thapar University, Patiala* for his thoughtful guidance, many insightful suggestions and generous support (academically, morally, financially) throughout this research work. Without his blend of patience, encouragement, and enthusiasm it would not have been possible for me to complete each of the research objective. He is an unique combination of great intellects and genuine caring for those persons for whom he has some responsibility. He has always been present to support and encourage me and is the source of the endless inspiration. I am grateful to him for introducing me to the field and for his continued guidance and encouragement ever since. Working with him has been a very rewarding experience, both academically and otherwise. I am truly indebted to him for his unflagging support, his invaluable guidance, and his irrepressible sense of humor.

I am equally grateful to my co-advisor **Dr. Rajeev K. Puri** *Professor, Panjab University, Chandigarh* for his kind guidance and support and for sharing his insight on nuclear physics. It has been both a privilege and a pleasure to have been associated with them. I am indebted to **Professor Puri** for being my co-guide and my mentor during my research work. He brings his keen insight to bear on the many problems we presented before him. He has really contributed a lot during my research work and revising my thesis. It is pleasure to thank him for his guidance, instruction, advice, humor, and patience. His constant support and advice in the theoretical aspects of research make possible for me to bring this dissertation within reach.

I would like to acknowledge my gratitude to **Dr. Kulvir Singh**, *Head, School of Physics and Materials Science, Thapar University, Patiala*, and **Prof. O.P. Pandey** for giving me the opportunity to be a part of their esteem School of Physics and Material Science (SPMS). Also thankful to them for providing me all the necessary facilities in the department and fellowship as a teaching assistant well in time. Also, I wishes to express thankfulness to all the faculty and staff of the School for their kind support. I am thankful to Prof. K.K. Raina, Deputy Director, and Prof. Seema Bawa, Dean Student Welfare, for their encouragement and constant moral support to accomplish this task. I acknowledge the useful suggestions of the members of my doctoral committee Dr. Manoj Sharma and Dr. D. P. Singh, and Dr. Mahesh Kumar. Thanks to Dr. P. K. Bajpai, Dean, research and sponsored projects for providing the possible research facilities here at Thapar University campus. Many thanks to the head of computer science department, Thapar University, Patiala for providing me the supercomputing facility.

Thanks also to all my other friends (past and present) and most notably my lab mates Drs. Sanjeev Kumar, Varinderjit Kaur, Shefali Kanwar and Mr. Karan Vinayak, Ms. Anupriya Jain, Mandeep Kaur, Rubina Bansal, Gudveen Sawhney, Manpreet Kaur, Deepika Jain, Kiran, Gurvinder and many others research scholars here at Thapar University, Patiala for the pleasure of their company and for making the experience an enjoyable and memorable one. I acknowledge with thanks the co-operation and encouragement extended by my colleagues in the Heavy-ion Reactions Theory Group at Panjab University, Chandigarh, particularly, Sakshi, Supriya, Yogesh, Rajeev Chugh and Ishwar Dutt for their fruitful discussions and novel views.

I would like to express my deepest gratitude to my parents, **Mr. Madan Lal Bansal and Mrs. Madhu Bansal** for their unbounded support and affection, for all they have given me throughout the years, all they have given up for me and above all for being such inspiring role models. Of course, none of this could have happened without the support of my in laws **Mr. Mohinder Vikram Mittal and Sushma Mittal**, my brother-in-law and bhabhi, **Mr. Sonu Mittal and Gituka Mittal**, my sister-in-law and jiju **Mrs. Anu Goyal and Mr. Navneet Goyal**, my sister **Nisha Bansal** and my sister and jiju **Mrs. Preeti Goyal and Mr. Raj Kumar Goyal**. They all have been my backbone in all the difficult phases of my life. The smiling faces and tantrums of kids, Gaytri, Prabhjot, Maskeen, Kunsh, Shubhi and my little son **Mudit Mittal** have always made me refreshing.

I owe great debt to my husband **Mr. Mukul Mittal** whose love, patience, and understanding made the final finishing of the thesis a lot of easier and paved the way to achieve this academic goal. I am grateful to him for provided smiling and untiring support towards this end and always being there for me.

I feel that the chain of gratitude would be definitely incomplete without thanking the

Almighty, to be kind enough to shower his blessings on me and holding my hand to the path of success.

Rajni

(Rajni)

Date : 26/10/2012

Patiala

List of Publications :

A. International Journals :

1. Experimental balance energies and isospin-dependent nucleon-nucleon cross-sections.
   Sanjeev Kumar, Rajni, and Suneel Kumar,
   Physical Review C 82, 024610(7) (2010).

2. Correlation between balance energy and transition energy for symmetric colliding nuclei.
   Rajni, Suneel Kumar, and Rajeev K. Puri,
   Physical Review C 84, 037606(4) (2011).

3. On the multifragmentation around the energy of vanishing flow using isospin-dependent model.
   Rajni, Suneel Kumar, and Rajeev K. Puri,
   Nuclear Physics A 875, 173-180 (2012).

4. Effect of scaled Gaussian width (SGW) on fragment flow and multifragmentation in heavy-ion collisions.
   Rajni and Suneel Kumar,
   European Physical Journal A 48, 19(7) (2012).

5. Effect of spatial and momentum constraints on multifragmentation.
   Rajni and Suneel Kumar,
   Physica Scripta (2012) (submitted).

6. Comparative study of different parameters in heavy-ion collision by using isospin-dependent reduced cross-section.
   Rajni and Suneel Kumar,
   Physical Review C (to be submitted).

B. Symposia/Workshops/Conferences:

7. Isotropic cross-sections and balance energy.

   Rajni, Sanjeev Kumar, Suneel Kumar, and Rajeev K. Puri,

   National theme workshop on nuclear reaction mechanism, March 17-19, Panjab University, Chandigarh (2010).

8. Effect of isospin dependent cross sections on the transverse in-plane flow at intermediate energy.

   Suneel Kumar, Rajni Bansal, Sanjeev Kumar, and Rajeev K. Puri,

   International Nuclear Physics Conference, July 04-09, University of British Colombia, Vancouver, Canada (2010).

9. Reduced isospin dependent cross section and elliptic flow in heavy-ion collision.

   Suneel Kumar, Rajni, Sanjeev Kumar, and Rajeev K. Puri,

   DAE symposium on Nuclear Physics, December 20-24, Birla Institute of Technology and Science, Pilani, Rajasthan (India) **Vol. 55**, 476-477 (2010).

10. Effect of spatial constraints on fragment production.

    Pallavi Gupta, Rajni, and Suneel Kumar,

    DAE symposium on Nuclear Physics, December 26-30, Andhra University, Visakhapatnam, **Vol. 56**, 776-777 (2011).

11. Effect of Gaussian width on stability of nuclei in IQMD model.

    Suneel Kumar and Rajni,

    DAE symposium on Nuclear Physics, December 26-30, Andhra University, Visakhapatnam, **Vol. 56**, 802-803 (2011).

12. Effect of different Gaussian width on disappearance of flow.

    Rajni and Suneel Kumar,

DAE symposium on Nuclear Physics, December 26-30, Andhra University, Visakhapatnam, **Vol. 56**, 804-805 (2011).

13. Effect of position and momentum constraints on charge distribution in heavy-ion collisions.
    Rajni and Suneel Kumar,
    DAE symposium on Nuclear Physics, December 03-07, University of Delhi, North Campus, New Delhi (India) (**accepted for poster presentation**) (2012).

14. To optimize the spatial and momentum constraints for fragment production.
    Rajni and Suneel Kumar,
    DAE symposium on Nuclear Physics, December 03-07, University of Delhi, North Campus, New Delhi (India) (**accepted for poster presentation**) (2012).

15. To study the effect of energy dependence of directed flow by using clusters and for all particles of the system.
    Rajni and Suneel Kumar,
    International Conference on Recent Trends in Nuclear Physics, November 19-21, Chitkara University, Barotiwala, Solan (India) (**accepted for poster presentation**) (2012).

Contents

ABSTRACT

In this work, theoretical investigations are carried out using the microscopic *isospin-dependent quantum molecular dynamics* (IQMD) model. We have tried to study the influence of isospin dependent cross-section on the balance energy. For this study, we analyze the effect of isospin dependent cross-section on fragmentation and collective flow (directed and elliptic) in heavy-ion collisions. An attempt is also made to study the effect of Gaussian width on the disappearance of flow and multifragmentation. We also aim to present a systematic study for the cut in momentum and phase space needed for fragmentation and their correlation with impact parameter, energy and mass of colliding nuclei. The results obtained from these studies are then compared with the experimental data of ALADIN, NSCL, FOPI, INDRA, and PLASTIC BALL Collaborations.

The present thesis is divided into following eight chapters.

Chapter 1 presents the general outline of the present work. The various phenomena measured/predicted at intermediate energies are explained in this chapter. It outlines the status of the available experimental attempts for multifragmentation and collective flow by different collaborations. The attempts of different theoretical models for these phenomenon are also presented.

Chapter 2 gives the overview of various theoretical models (Primary and Secondary) used in the literature. Primary model generates the phase space of nucleons and can group them into Statistical and Dynamical models. In this chapter, different dynamical models are explained. These dynamical models at intermediate energies can be subdivided into two classes. One which follows the time evolution of one-body phase space distribution (BUU, IBUU, SMF) and others based on the N-body molecular dynamics (QMD and IQMD) are studied in detail. This chapter presents the idea about how one model overcome the limitation of the other one. In this chapter, IQMD model is explained in detail. Some secondary algorithms used for the study of clusterization of nucleons is also described in brief. These include Minimum Spanning Tree (MST), MST with momentum cut (MSTP), and Simulated Annealing Clusterization Algorithm (SACA). In this thesis, the MST and MSTP methods have been used for the clusterization of nucleons.

In **chapter 3**, we present a systematic optimization for isospin-dependent cross-section (σ= 0.7 to 1.3 σ_{NN}), on directed flow for a variety of systems $^{12}C_6$ + $^{12}C_6$, $^{20}Ne_{10}$ + $^{27}Al_{11}$, $^{40}Ar_{18}$ + $^{45}Sc_{21}$, $^{40}Ar_{18}$ + $^{51}V_{23}$, $^{86}Kr_{36}$ + $^{93}Nb_{41}$, $^{64}Zn_{30}$ + $^{58}Ni_{28}$, $^{93}Nb_{41}$ + $^{93}Nb_{41}$ $^{129}Xe_{54}$ + $^{118}Sn_{50}$, $^{139}La_{57}$ + $^{139}La_{57}$, and $^{197}Au_{79}$ + $^{197}Au_{79}$ (for which experimental balance energies are available) using an IQMD model. We show that balance energies are sensitive towards isospin-dependent cross-sections for light systems, while nearly no effect exists for the heavier nuclei. A reduced cross-section $\sigma = 0.9\sigma_{NN}$ with stiff equation of state is able to explain experimental balance energies for most of the systems. The interactions among the nucleons remain either attractive or repulsive throughout the time evolution which depends on the incident energy, isospin-dependent cross-section, as well as the composite mass of the system. We notice a change in the sign of the slope of transverse momentum when plotted as a function of the rapidity distribution. The directed flow goes from a negative to positive value with an increase in the incident energy. This is the general trend and is explained many times in the literature by taking the concept of mean field and NN cross-sections. Lighter systems remain in the environment of mean field compared to NN collisions at any given incident energy. It is also observed that a higher incident energy is needed in lighter nuclei to balance the attractive and repulsive forces compared to heavier systems. This is due to the dominance of Coulomb repulsion with an increase in the composite mass of the system. A power law behavior is also given for the mass dependence of balance energy, which also follows the N/Z dependence.

In **chapter 4**, we analyze the fragmentation of colliding nuclei $^{197}Au_{79} +^{197} Au_{79}$, $^{139}La_{57} +^{139} La_{57}$, $^{93}Nb_{41} +^{93} Nb_{41}$, $^{86}Kr_{36} +^{93} Nb_{41}$, $^{64}Zn_{30} +^{58} Ni_{28}$, $^{40}Ar_{18} +^{45} Sc_{21}$ using IQMD model. The corresponding energy of vanishing flow (EVF) for these system were reported to be 48, 58, 62, 56, 64, 80 MeV/nucleon respectively in chapter 3. The calculations are performed with the isospin-dependent reduced cross sections ($\sigma = 0.9\sigma_{NN}$) and are also done below and above the EVF. In the present calculations, mass dependent Gaussian width has been employed to achieve maximum stability of colliding nuclei. The free nucleons, light mass fragments (LMFs) are emitted from the participant source that scales with the size of the emitting source while medium mass fragments (MMFs) and intermediate mass fragments (IMFs) come from the spectator part showing well known universality in the multiplicity. Since for lighter system energy of vanishing flow is very high. The transition from the spectator to participant matter is swift and sudden. The reverse is true for heavy systems. Final results are compared with NSCL experimental data. It is found that no particular fragment structure found at the EVF.

In **chapter 5**, we study the correlation between the balance energy and transition energy of fragments in heavy-ion collisions for different systems ${}^{40}Ar_{18}$ + ${}^{45}Sc_{21}$, ${}^{93}Nb_{41}$ + ${}^{93}Nb_{41}$, ${}^{139}La_{57}$ + ${}^{139}La_{57}$, and ${}^{197}Au_{79}$ + ${}^{197}Au_{79}$ at incident energies between 40 and 1200 MeV/nucl. using the IQMD model. With increase in incident energy, elliptic flow shows a transition from positive (in-plane) to negative (out-of-plane) values. This is due to the fact that mean field at low energy, which contributes to the formation of a rotating compound system, becomes less important and the collective expansion process based on the nucleon-nucleon scattering starts to be predominant. This transition energy is found to depend on the size of the fragments, composite mass of the reacting system, and the impact parameter of the reaction. The free and LMFs feel the mean field directly, while heavy fragments have weaker sensitivity. The free particles and LMFs, which originate from the participant zone, show a systematic behavior with the beam energy and with the composite mass of the system. The heavier the system is, the greater the Coulomb repulsion is and the more negative the elliptical flow is.

A close agreement with experimental data of INDRA, FOPI, and PLASTIC Ball collaboration is obtained in the presence of the hard equation of state and with $\sigma = 0.9\sigma_{NN}$ for Z=2 particles. There is a correlation between transition energy and balance energy as their difference decreases with an increase in the total mass of colliding nuclei.

In **chapter 6**, we present the analysis for different system size effects, excitation energies and colliding geometries. We study the multifragmentation using a soft equation of state along with enhanced and reduced clusterization range (R_{clus}) and momentum constraints (P_{clus}) with an isospin-dependent reduced cross-section. For a given set of input parameters, we find that effect of a different range of momentum and spatial constraints depends on the mass, energy and colliding geometry of the system. We note that all model ingredients have sizable effect on the fragmentation pattern. Fragments are formed with minimum spanning tree method. For R_{clus} = 4 fm there is a systematic trend for different value of P_{clus} compared to other clusterization parameters. In this clusterization range, there is no change in the production of the $\langle M_{IMF} \rangle$ above P_{clus} = 240 MeV/c. Our analysis indicates that the effect on fragment production is stronger if a cut in the relative momentum of two nucleons is 240 MeV/c at a spatial separation of 4 fm. Our results for ${}^{197}Au +{}^{197} Au$ collisions are in good agreement with the experimental data of ALADIN and for ${}^{129}Xe +{}^{139} La$, ${}^{86}Kr +{}^{93} Nb$, ${}^{40}Ar +{}^{45} Sc$ with the NSCL data.

In **chapter 7**, we simulate for different system size effect, excitation energy, colliding geometry and study the role of interaction range on multifragmentation using $\sigma = 0.9\sigma_{NN}$ and soft equation of state. We change the value of scaled Gaussian width (SGW) by reducing and enhancing SGW from normal SGW. In the case of broader Gaussian, the particles in a cluster are bound to a large number of other nucleons inside a cluster. A reduced width leads to fluctuations which results in a large number of light and intermediate mass fragments. Broader Gaussian produces more excited fragments compared to narrow Gaussian. We find that the effect of the width of Gaussian wave packet associated with a nucleon depends on the mass of colliding system. We noted the range of SGW from time evolution of largest fragment and see its effect on balance energy. This range is then compared with the experimental data of ALADIN and NSCL. It is noted that either the highest or lowest range is in agreement with the experimental data. The lowest SGW gives more positive value of flow and also gives large multiplicity of IMF $\langle M_{IMF} \rangle$ as compared to highest SGW. The reason is that as we decrease the Gaussian width, the probability of reaction taking place increases, which further results in an increase in NN collisions and hence more positive value of directed flow. For a given set of input parameters, we find that width has a sizable effect. At the same time, we know that different set of parameter can influence the reaction dynamics drastically. Hence, in our opinion it may not be possible to pin down the width to a very narrow level. Our studies shows that SGW influence the reaction dynamics.

Finally, we will summarize our results and outlook of the present work in chapter 8.

Chapter 1

Introduction

The heavy-ion collisions (HIC) at intermediate energies (10 MeV/nucleon $\leq$ E $\leq$ 2 GeV/ nucleon) produce a piece of hot and dense nuclear matter. HIC are unique tool to produce a large volume of nuclear matter at high temperature and densities in a laboratory [1-4]. In addition to this, several phenomena like the multifragmentation, collective flow and sub-threshold particle production are also observed [1, 5]. Two heavy nuclei can be compressed to produce higher densities than the ground state saturation density in head-on collisions at high energies. A flow pattern will develop as system subsequently expands which is used to study the properties of the hot and compressed nuclear matter over a wide range of densities [6-8].

1.1 Phase transition in nuclear matter

The dramatic changes of the properties of a substance undergoing a phase transition fascinated mankind since the early beginnings of the science. Empedokles of Agragas -the Greek philosopher, statesman and poet -suggested nearly 2500 years ago that world is composed of four primal elements: earth, water, air and fire [9]. Indeed, a glass of liquid water cooled below 0^0C will freeze to ice showing the solid character of the liquid. Water when heated above 100^0C will build an airy gas. Finally at high temperatures, atoms disintegrate into a plasma of electrons and ions which loosely speaking may be considered as analog of the fire. In that sense, the four roots earth, water, air and fire can be considered as a symbol for what we call now solid, liquid, gas and plasma phase. The prospect of creating a phase of matter resembling that of the pre-hadronic phase of the early universe or of the core of today's neutron stars [10] is one of the **prime motivations to study the relativistic heavy ion collisions** [8]. Unquestionable, the transition to the quark-gluon plasma represents the most spectacular example of the phase transition in nuclear matter. The study of the nuclear matter is possible only by the means of small excited pieces produced in nuclear collisions. Therefore, the major difficulties arise due to the fact that the phase transitions in finite systems are not as well defined as in infinite matter. In the case of excited nuclei, the liquid phase may be tentatively identified with fragments and the gas phase with light particles. Already two decades ago, Vander Walls behavior of the nucleon-nucleon force inspired the idea of a liquid-gas phase (LGP) transition in nuclear matter [11-14]. Nuclear forces have a long range attractive potential and a short range repulsive core, a LGP is expected to occur in infinite nuclear matter. The phase transition is among the various phenomena that has lead to the study of heavy ion collisions at a deeper level. The benefit of the study of heavy ion collisions in a laboratory is that it can be controlled and noise can be minimized. The heavy-ion reaction, during which the matter undergoes compression and expansion stages, are true testing grounds for the hot and dense nuclear matter. The expansion of the nuclear matter (after compression stage) usually leads to freeze out for the interactions at sub-normal densities ($\rho < \rho_0$). The freeze-out temperature and density could be in the phase transition region (Quark-Gluon Plasma (QGP) to hadron gas (HG) phase transition, or LGP), or in HG phase. The specific region of the phase-diagram and corresponding physics depends crucially on the incident energy as well as on the geometry of a collision.

1.2 Central and peripheral collisions

In order to heat a nucleus up to the excitation energy where the phase transition is expected, two different classes of the experiments are possible:-

- Central collision of two equally sized nuclei at intermediate energies.
- Peripheral collision at a much higher incident energies.

In the first case, generally overlap region is investigated whereas in the second case, the spectator nuclei emerging from the primary collisions is of interest and is investigated. Fig.1.1 shows the definition of the impact parameter (b) as well as of participant and the spectator matter. Participant are those nucleons which take part in the reaction whereas spectator matter does not take part directly in the collision. According to transport model calculations, participant nucleons create the fireball (the hot and dense nuclear matter) that cools down in about 10-15 fm/c after the phase of higher density.

As noted, the internal memory of the nucleons is often erased and new dynamics take

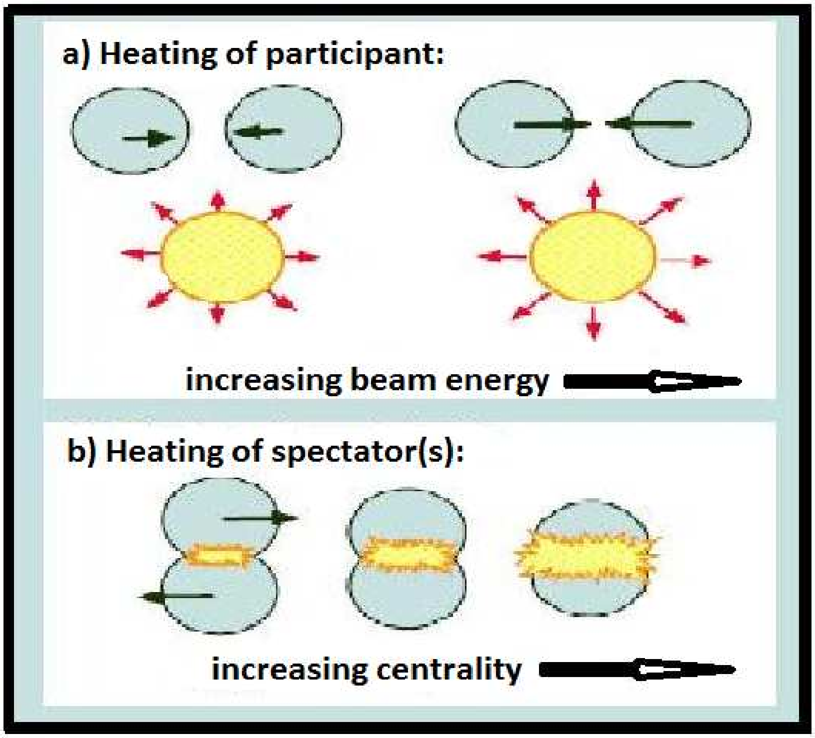

Figure 1.1: Pictorial view of the two different ways to produce boiling nuclei [15].

place. Impact parameter is given for the occurrence of a particular phenomena. In central collision, most of the matter ends up as participant whereas in peripheral collision one has large portion as spectator matter. In a head on collision between equally heavy nuclei, the excitation is determined by the incident beam energy. The clear advantage of this method is that, for a given target-beam combination, system with nearly constant mass number can be produced. However, a significant fraction of the energy is not converted into the heat but in collective explosive motion, thus introducing an additional degree of the freedom which also depends on the incident energy. As noted above, spectators are produced in peripheral collisions that do not show this collective motion in the initial stage, though some radial flow may arise during the thermally driven expansion prior to the breakup [16, 17] and may contribute to the kinetic energy of the fragments.

1.3 The Nuclear Equation of State (NEOS)

The equation of state shows the region of the instability for a first order liquid-gas phase transition that terminates at a critical point. If an equilibrium is reached during a heavy-ion collision, the system can be described by the nuclear equation of state (NEOS), i.e., a relation between three thermodynamical variables, namely, pressure, volume and temperature. For the nuclear matter, these are replaced by the internal energy E, temperature T and density ρ. The internal energy can be decomposed into thermal (E_{th}) and a compressional (E_c) parts.

$$E(\rho, T) = E_{th}(\rho, T) + E_c(\rho, T = 0) + E_0, \tag{1.1}$$

where compressional part (E_c) is defined at zero temperature and E_0 is the ground state energy. There are two possible means to explore the dependence of the compressional energy per nucleon on the density ρ and temperature T in astrophysical observations [18] and heavy-ion collisions. The $E(\rho, T)$ region explored by the astrophysical observations is, however, quite different than that of accessible in heavy-ion collisions. The astrophysical objects are usually cold, whereas in heavy-ion collisions compression goes along with the excitation. Therefore, NEOS offers an insight into the new phases of the nuclear matter and conditions inside a supernova explosions, neutron stars, big-bang and heavy-ion collisions. Generally the interactions in heavy ion collision can be described within the G-matrix, where real part of the G-matrix define the mean field and imaginary part is responsible for the collision dynamics. The real part of the G-matrix is often parametrized in terms of the Skyrme interactions. In the study of heavy-ion collisions, one usually employ the so-called the Skyrme parametrization of NEOS, which contains two sets of the parameter giving the same correct binding energy and saturation density, but, two different incompressibility K(one corresponds to soft equation of state with $K = 200$ MeV(at smaller value of γ), another corresponds to the hard equation of state with $K = 380$ MeV (at larger value of γ)). The density dependence of the compressional energy per nucleon is shown in Fig.1.2 for the soft and hard interactions.

When the momentum dependence of the mean field is introduced, we have to readjust the parameters of the Skyrme forces to have correct saturation properties for the normal nuclear matter [19] and the same incompressibilities as those of the soft and hard equation of state. The new parameter sets with the momentum dependence are called soft momentum dependent (SMD) and hard momentum dependent (HMD), respectively. These four sets of parameters are listed in table 1.1 together with the incompressibilities. The meaning of these parameters is given on page 29 in Eqn.(2.3). There are other studies reported in literature where different values of incompressibility have been used as shown in table 1.2,

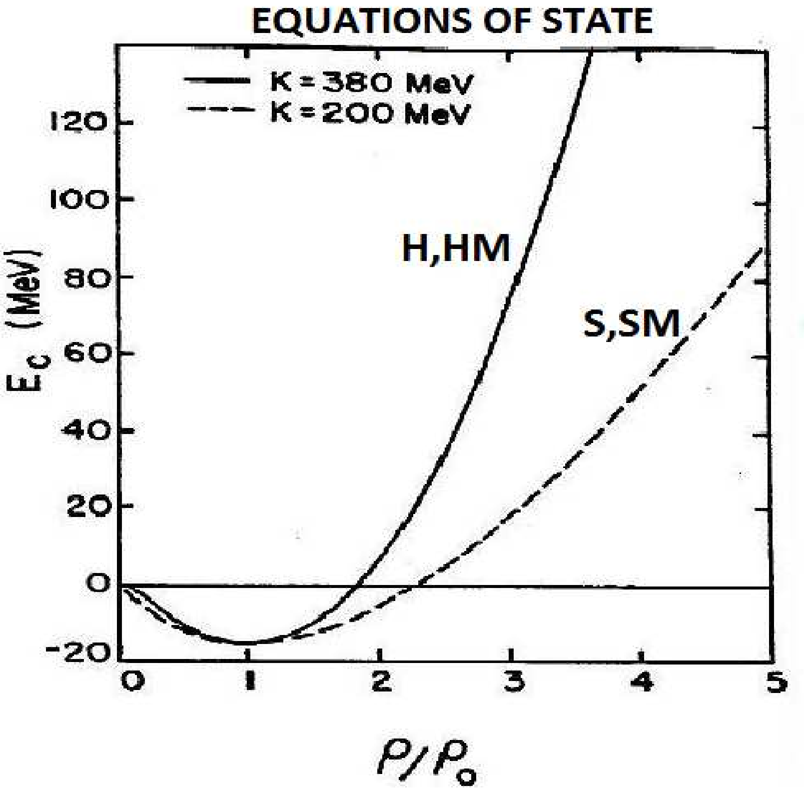

Figure 1.2: The density dependence of compression energy per nucleon. The Soft and Hard interactions are shown by dash and solid lines, respectively. The figure is taken from Ref. [20].

also the incompressibility values can be extracted from monopole resonances by formulae $E_{GMR} = (\hbar^2 K_A/m < r^2 >)^{1/2}$, where m is the nucleon mass and $< r^2 >$ is the mean square nucleus radius. Using the $A^{1/3}$ expansion of K_A, the compressibility of nuclear matter, K_{NM}, which is one of the important parameters in understanding the behaviour of heavy ion reactions, can be obtained [21, 22].

Table 1.1: Parameters of static potentials [5]

K(MeV)	$\alpha(MeV)$	$\beta(MeV)$	γ	EOS
200	-356	303	1.17	Soft(S)
380	-124	70.5	2	Hard(H)
200	-390	320	1.14	SMD
380	-130	59	2.09	HMD

Table 1.2: Other suggested parameters for different EOS [21, 22]

K(MeV)	$\alpha(MeV)$	$\beta(MeV)$	γ	EOS
200	-382.52	328.27	1.155	Soft(S)
380	-125.16	70.91	2.0	Hard(H)
200	-3189	3176	1.011	SMD
380	-63.13	49.42	2.12	HMD

1.4 Isospin physics

During the earlier days, the heavy-ion physics attempts were made to understand the matter and properties of the nuclei which are stable in nature, all lighter nuclei have either equal number of protons and neutrons or are close to this line. After the detailed investigation of the stable nuclei with $N \approx Z$, structural physics was then diverts to produce nuclei away from the line of stability. Those nuclei were produced with large neutron rich/deficient content. In a similar fashion the physics of intermediate energies was divert in recent time to understand the dynamics for nuclei away from the line of stability. We have collision of nuclei with larger neutron/proton content. To understand the phenomena emerging from these neutron rich/deficient nuclei, many existing models are developed for heavy-ion collision (HIC), such as the isospin-dependent percolation [23], isospin-dependent lattice gas model [24] and isospin-dependent transport models, have been extended to include the isospin degree of freedom. It is worth mentioning that the transport models are particularly useful for studying the isospin-dependent equation of state and the in-medium nucleon-nucleon cross-sections. Besides the many radioactive beam facilities that already exist in the world, a number of next generation radioactive beam facilities are being constructed or planned. At these facilities, nuclear reactions involving the nuclei with large neutron or proton excess can be studied, thus providing a great opportunity to study both the structure of rare isotopes and the properties of the isospin asymmetric nuclear matter that has a large neutron to proton ratio. This has stimulated new interest on the subfield emerging from the study, called isospin physics. In this thesis, we will focus on the reaction aspect of the isospin physics, especially heavy-ion reactions induced by the neutron-rich beams at intermediate energies. The ultimate goal of this branch of isospin physics is to determine the isospin dependence of the in-medium nuclear effective interactions and the equation of state of isospin symmetric nuclear matter, particularly its isospin dependent term, i.e. the density dependence of the nucleon symmetry energy. The components of the atomic nuclei, the neutron

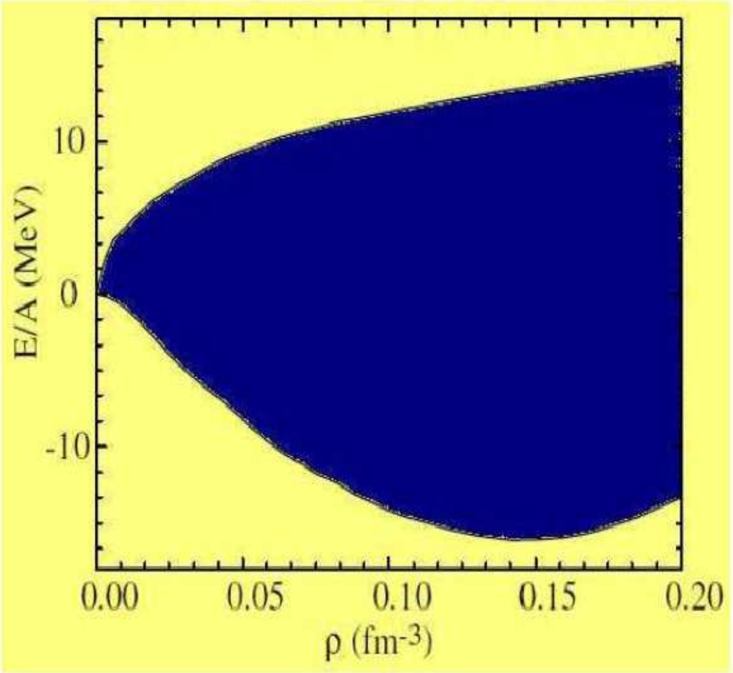

Figure 1.3: The concept of symmetry energy: The top line is the energy density for pure neutron matter and lower line is that for symmetric nuclear matter. The difference of two lines is the symmetry energy. The figure is taken from Ref. [25].

and the proton, form an isospin doublet since they differ only in the electric charge.

The isospin dependence of the NEOS is often expressed in terms of symmetry energy. Considerable efforts are being made to experimentally extract the symmetry energy and its dependence on the nuclear density and temperature [26]. A binding energy formula expresses the energy E of a nucleus in terms of charge Z and mass A i.e. $E = E(A, Z)$. The Bethe-Weizsacker (BW) mass [27, 28], formula is sum of five terms namely,

$$E = -a_V A \ + \ a_S A^{2/3} \ + \ \frac{a_C Z(Z-1)}{A^{1/3}} \ + \ \frac{a_A (N-Z)^2}{A} \ + \ \delta. \tag{1.2}$$

For the details of these terms, reader is referred to the Ref. [28]. The fourth term in the formula, $a_A(N-Z)^2/A$, with $a_A \approx 21$ MeV, is commonly known as symmetry energy term. This symmetry energy as a function of density has been parametrized in different terms as [29]

$$V^1_{Sym} \ = \ cF_1(u)\delta\tau_z, \tag{1.3}$$

$$V^2_{Sym} \ = \ cF_2(u)\delta\tau_z \ + \ \frac{1}{2}cF_2(u)\delta^2, \tag{1.4}$$

$$V^3_{Sym} \;=\; cF_3(u)\left[\delta\tau_z \;-\; \frac{1}{4}\delta^2\right], \tag{1.5}$$

with $\tau_z \;=\; 1$ for neutrons, and -1 for protons.

where $F_1(u) \;=\; u$, $F_2(u) \;=\; u^2$ and $F_3(u) \;=\; u^{1/2}$ and, $u \;=\; \frac{\rho}{\rho_0}$; δ is the relative neutron excess $\delta \;=\; \frac{\rho_n-\rho_p}{\rho_n+\rho_p} \;=\; \frac{\rho_n-\rho_p}{\rho}$; ρ, ρ_0, ρ_n and ρ_p are the total, normal, neutron and proton densities respectively. The strength of c is of the order of 32 MeV to reproduce the 4^{th} term of the Bethe Weizsacker mass formula.

The isospin-dependent quantum molecular dynamic (IQMD) model [2, 30] developed by C. Hartnack and collaborators reduces the above symmetry potentials into a form:

$$V_{Sym} = t_6\frac{1}{\varrho_0}T_3^iT_3^j\delta(r_i{}' - r_j), \tag{1.6}$$

where, T_3^i, T_3^j are their respective T_3 components (i.e. 1/2 for protons and -1/2 for neutrons), $t_6 \;=\; 100$ MeV and $\delta(r_i{}' - r_j)$ represents the distance between two nucleons. Here again the strength of the symmetry energy is found to be of the order of 32 MeV.

An elementary illustration of the concept of symmetry energy is shown in Fig.1.3. Symmetric matter is represented by the lower line, while pure neutron matter is expressed by the upper line. The difference between the two lines is the symmetry energy, which express the effect of the isospin on nuclear matter energy density. The effect of the isospin content on multifragmentation, directed transverse flow, elliptical flow shall be discussed in this thesis. In the following section, we will introduce some of the basic concepts that will allow better understanding of the topics to be discussed in the following chapters.

1.5 PHENOMENOLOGY AND DEFINITION

1.5.1 Multifragmentation

Nuclear fragmentation appears as an intermediate mechanism bringing the low-energy decay modes dominated by the evaporation (and fission for heavy systems) leading to the formation and decay of a long-lived compound like nuclear system and the high-energy decay modes characterized by the complete vaporization of the system leading to the fast disintegration of the system into fragments. The nuclear fragmentation reaction in which excited nuclei break up into intermediate size fragments are believed to be associated with a liquid-gas type phase transition in nuclear matter. The formation of the various phases of nuclear matter in heavy-ion collisions has been investigated by measuring the nuclear species emitted from the excited systems. Theoretical studies indicate that it is most feasible to study

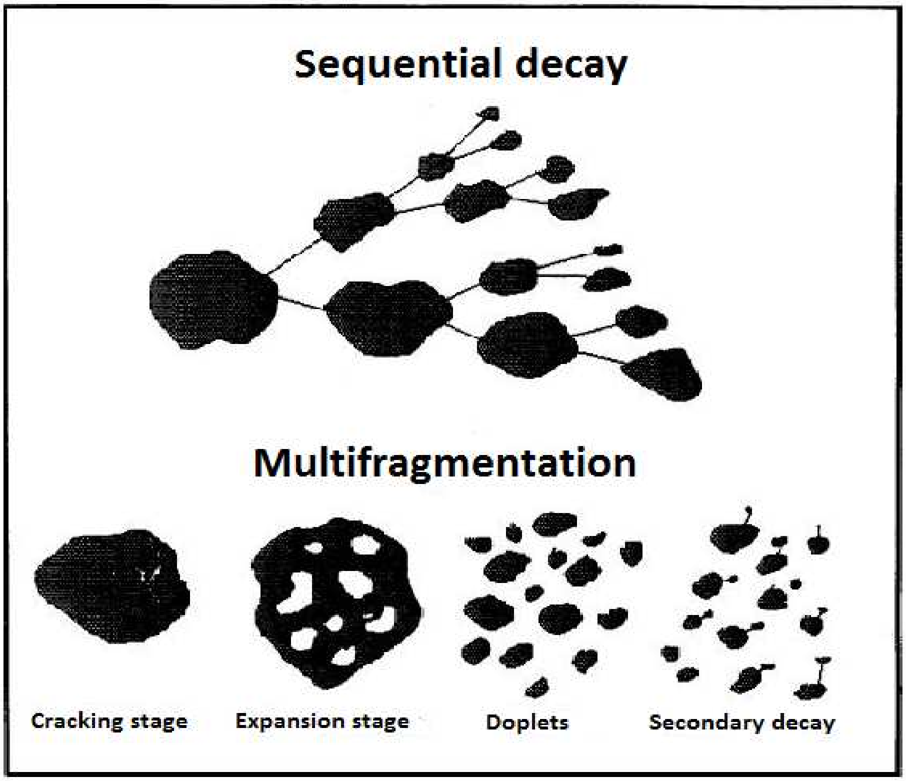

Figure 1.4: At low energy, particle emission is dominated by the sequential decay and at high energy, particle emission is dominated by the multifragmentation. The figure is taken from Ref. [31].

the liquid-gas phase transition by observing multifragment emission from nucleus-nucleus collisions [12, 32, 33]. The probability of multifragment emission is expected to increase as the excitation energy increases because of the available phase space. Statistical nuclear multifragmentation is a signature of the transition of nuclear matter from a liquid phase into a phase of several nuclear fragments with a broad mass distribution. There are two extreme approaches in statistical theories, sequential decay approach and the simultaneous breakup approach [31] in describing the heavy-ion reactions as shown in Fig.1.4. In the sequential statistical theory, one assumes that the compound system de-excite through a sequence of binary breakup. The final fragments are the sum of the chain binary decay. While in the simultaneous breakup approach, the fragments are in equilibrium with each other as the system expands. It is observed that at low beam energies (below 10 MeV/nucleon), the particle emission is dominated by the sequential decays and at high incident energies, the multifragmentation takes place and the particle emission is dominated by the simultaneous decay. Nuclear fragmentation and its connection to the behavior of the nuclear matter at high excitation energy is the subject of intensive theoretical and experimental investigations. Multifragmentation reaction can be thought of as three-step process:-

- In the first step, excitation energy is deposited in the target nucleus and preequilibrium particles are emitted.
- In the second step, thermalized source breaks up into intermediate mass fragments.
- In the final step, excited prefragments decay via standard sequential decay channels into fragments that can be observed by the detector.

The main physical issues related to the nuclear multifragmentation are associated with the properties of the nuclear equation of state (NEOS) at finite temperature T and low density ρ.

1.5.2 Collective motion

Collective flow is a measure of the transverse motion imparted to the particles and fragments during the collision of two nuclei and is characterized by the correlation between the particle positions and momenta of a dynamic origin. As already stated, if two heavy nuclei can be compressed to more than ground state saturation density and heated in head-on collisions at high energies then the flow pattern will develop as system subsequently expands. During the decompression stage, the direction and the speed of the particles is towards the region of the lower pressure i.e. number of ejectiles exhibit a common property (e.g. the emission of the many particles of the same kind or the emission of many ejectiles with a common velocity field or into a common direction). This pressure-dependent correlation between the particle position and momentum is known as collective flow. The meaning of the flow in classical and nuclear physics is different. In classical physics, final state of the particles in flow are linked to the properties of the fluid such as the equation of state and viscosity. In nuclear physics, flow of the particles is described in terms of dynamical properties of the collisions such as the in-medium nucleon-nucleon cross-section and the nuclear compressibility. The three types of the flow generally discussed in nuclear collision, are as radial, directed and elliptic flows. In this thesis, we shall discussed the directed and elliptic flows. The **directed flow** refers to the preferential emission of the particles within and to a particular side of the reaction plane (The reaction plane is defined as the plane that contains the beam axis and a line joining the centres of two nuclei). The directed flow is used whenever the velocity field is found to be independent of the azimuthal angle. The left part of Fig.1.5 shows the

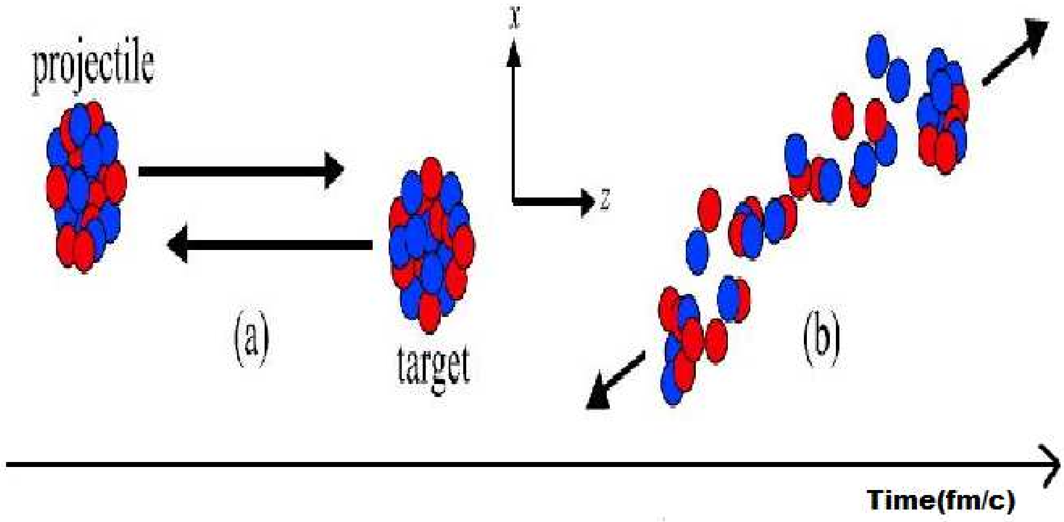

Figure 1.5: Diagramatic representation of the directed flow to the particular side of a reaction plane. After collision of two nuclei, projectile or target nucleons are directed in one particular direction [34].

emission of the particles to a particular side of the reaction plane. Two heavy nuclei in the center-of-mass frame are incident upon each other with non-zero impact parameter and the reaction plane is taken as the plane of the paper. After the collision, projectile (target) nucleon are directed mostly in the positive (or negative) direction shown in the right part of the Fig.1.5. In the transverse plane, this corresponds to the azimuthal ϕ distribution that are peaked at 0^0 (or 180^0) for the projectile (or target) nucleons.

On the other hand, the **elliptic flow** describes the preferential emission of the particles with respect to certain azimuthal angle and with back-to-back symmetry. Note that the elliptic flow has same distribution in both rapidity regions. Elliptic flow refers to the anisotropy of the ϕ distribution at midrapidity and its value indicates whether the particle emission is in-plane or out-of-plane. The azimuthal distribution which is peaked at 0^0 and 180^0 exhibits an in-plane emission on the other hand, the azimuthal ϕ distribution peaked at $\pm 90^0$ signifies the out-of-plane emission. Fig.1.6 illustrates the formation of the compression region in a noncentral collision and the subsequent emission of the particles from the midrapidity

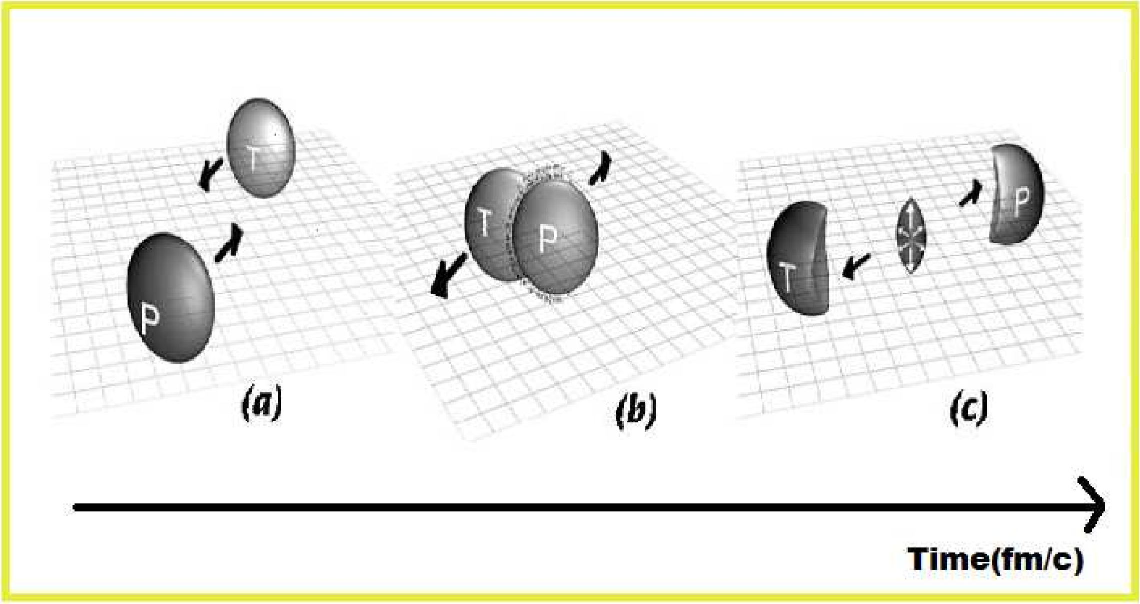

Figure 1.6: Illustration of two colliding nuclei before collision, early collision and late collisions and resulting elliptic flow of the participant zone. The figure is taken from Ref. [34]

region.

1.6 Review of experimental attempts for collective flow and multifragmentation

Until seventies, one could accelerate the light-ions only, therefore the field was dominated by shooting the light particles on heavy targets. In other words the study of the nuclear physics was confined to phenomena such as fusion, fission, and particle transfer etc. At present, new and larger accelerators are built that could accelerate heavy nuclei upto several hundred of GeV. These accelerators were built at the Michigan State University (USA), GANIL (France), GSI (Germany), relativistic heavy-ion collider (RHIC) and superconducting supercollider (SSC) at BNL (USA), NSF-Arizona accelerator mass spectrometry laboratory at the University of Arizona (USA), Vivitron accelerator in Strasbourg (France). These accelerators have contributed a lot to the field of heavy-ion collision. This development has opened a new vistas in the field of intermediate and high energy heavy-ion reactions.

Nuclear fragmentation, discovered in the cosmic rays, was a puzzling phenomena accompanying the collision of relativistic protons with a target and consisted of the emission of the slow nuclear fragments. These fragments were in the range of $3 \leq Z \leq 30$, dubbed as intermediate mass fragments (IMFs). In 1980's, Jakobsson *et.al.*, [35] observed the multiple emission of the IMFs in the emulsions irradiated by the carbon beam of 250 MeV/nucleon. This result created an interest towards multifragmentation. Using the radiochemical methods, a total cross-section of the fragmentation could not be determined and the process has been considered quite rare and exotic.

Experimentally, the first convincing evidence for the occurrence of sideward flow [36, 37] was obtained by so-called 4 π detectors, the Streamer Chamber [38] and the Plastic-Ball/Wall [39] at the Bevalac in Berkeley. In this review, we restrict ourselves to the description of FOPI and ALADIN detector at the SIS (GSI), INDRA at GANIL (France), NSCL at Michigan State University (USA). We compare our theoretical results with the experimental result of these detectors.

ALADIN spectrometer The experiment was performed at SIS accelerator at GSI, Darmstadt with ALADIN forward spectrometer. We have studied multifragment decays of $^{197}Au_{79}$ projectiles after the collision with C, Al, Cu and Pb targets at bombarding energy of 400 and 1000 MeV/nucleon [40-42]. In these collisions, energy deposition are reached which covers the range from particle evaporation to multifragment emission and further to total disassembly of nuclear matter, the so called 'rise and fall of multifragment emission' [43]. The ALADiN (A Large Acceptance Dipole magNet) spectrometer was designed to study projectile fragments produced in heavy ion collisions at relativistic energies. In the Fig.1.7 beam enters from the left and is monitored by the beam counters before reaching the target. The entrance to the dipole magnet is surrounded by the Si-CsI(TI) array. Projectile fragments are tracked and identified in TP-MUSIC III detector and in the time-of-flight wall. Coincident neutron emitted approximately in the direction of the incident beam (dashed line) are detected with the large area neutron detector (LAND). The dash-dotted line represents the trajectory of beam particles after they were deflected by an angle of 8^0. The Au beam with an energy of 600 MeV/nucleon was collided with targets of C, Al, Cu and Pb with a thickness of 200 to 500 mg/cm^2. The inverse kinematics focuses the fragmentation products of the Au projectiles into the forward direction. The charge and multiplicity of nuclear fragments were determined by means of time-of-flight (TOF) wall, with unit charge

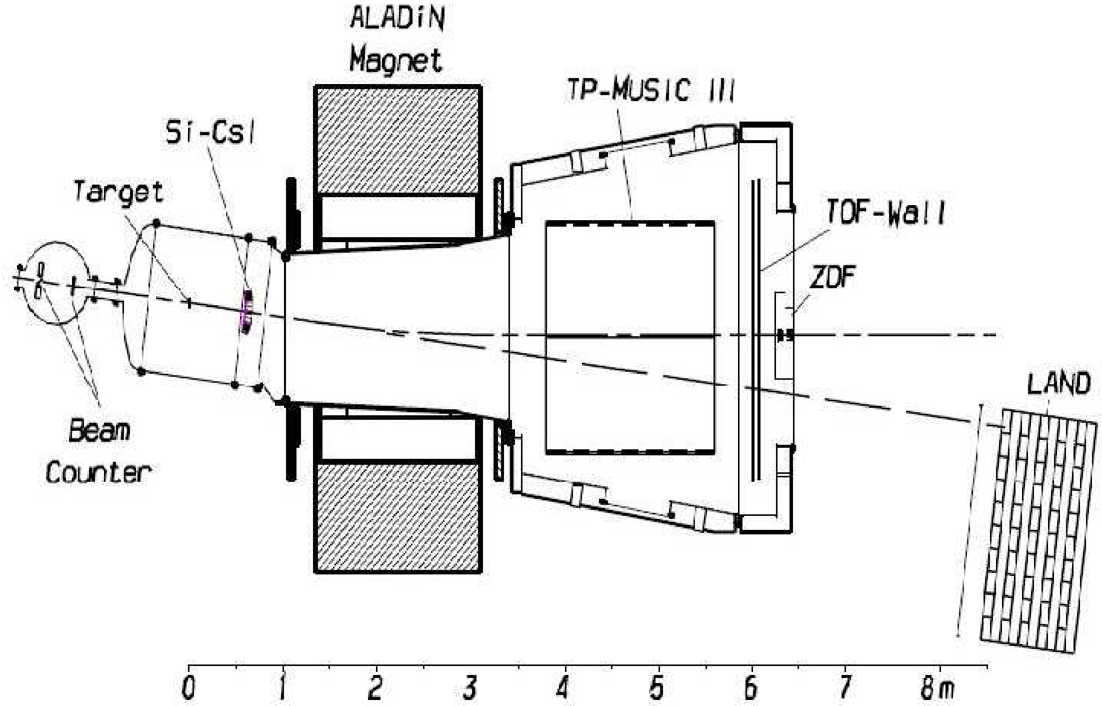

Figure 1.7: Cross sectional view of ALADIN setup. The figure is taken from Ref. [44]

resolution for $Z \leq 8$ fragments and $\Delta Z = 2$ for the heavier fragments. The TOF wall covered an area of 1m × 1m with two layers of 40 scintillators each. This corresponds to an acceptance for beam velocity N=Z fragments of $\pm 4.7^0$ the horizontal and $\pm 4.2^0$ in the vertical direction. Fragments with $Z \geq 10$ were identified by the Time Projection - Multiple Sampling Ionization Chamber (TP-MUSIC) detector positioned between the magnet and the TOF wall. This information was used to determine the emission angle of the fragments and to calibrate the charge response of the TOF wall for heavier elements. Light particles, predominantly originating from the fire-ball region, were detected by a 64 element Si-CsI hodoscope in the angular region between 7^0 and 40^0.

INDRA multidetector The 4π multidetector INDRA [45] was commissioned in 1992 to perform multifragmentation studies with heavy-ion beams in the Fermi energy domain at the GANIL Laboratory. In 1997 INDRA has been transported to GSI (Darmstadt) in order to extend multifragmentation studies into the domain of higher projectile energies available from the heavy-ion synchrotron SIS-18 synchrotron. The study has been partly motivated by previous results obtained by the ALADIN collaboration for $^{197}Au +^{197} Au$ collisions at

600, 800 and 1000 MeV/nucleon [40-42].

FOPI Detector The FOPI collaboration has reported on the disappearance of the elliptic flow [46] at beam energies close to 100 MeV/nucleon for the system Au + Au. At higher energies, elliptic flow was observed for charged nucleons and light fragments by the Diogene collaboration and later by the Plastic Ball, FOPI, EOS, and KAOS collaborations [46-48]. However, this elliptic flow was found to be oriented out-of-plane. It can be understood in terms of the shadowing effect of the passing spectators, which reduce the mean free path of particles emitted into the reaction plane with respect to the emission out of plane. Nevertheless, the occurrence of elliptic flow was predicted by hydrodynamic calculations and other transport calculations that also point out its sensitivity to the equation of state [49, 21]. Measurements of neutron elliptic flow by the LAND collaboration [50] report no isospin dependence (when compared with protons). An excitation function of the elliptic out-of-plane flow for light particles measured by the Plastic Ball collaboration shows a rise and fall in the energy range from 150 MeV/nucleon to 1150 MeV/nucleon. The fall of the signal could be expected within the shadowing scenario because the effective shadowing time is reduced at higher energies. In all measurements, the elliptic flow was found to increase with the transverse momentum of the particle.

NSCL at MSU Even though the first pioneering fragmentation experiments were performed more than 30 years ago in Berkeley [51], we still do not fully understand the reaction mechanism. To understand the fragmentation experiments with ^{64}Ni, ^{68}Ni, ^{69}Cu, and ^{72}Zn beams were performed with the Coupled Cyclotron Facility (CCF) [52] at the National Superconducting Cyclotron Laboratory (NSCL) [53, 54] at Michigan State University (MSU).

1.7 Review of theoretical models for multifragmentation and flow

Several new and interesting phenomena related to the isospin physics have been observed in heavy-ion collisions recently. To understand such phenomena, many models have been developed. Most of the studies are concentrated to study the process of multifragmentation and flows observed in heavy-ion collisions at intermediate energies. At low incident energies, due to the lack of the free phase space, about 98 % of the attempted collisions are blocked. The whole dynamics at low incident energies is governed by the mean field or by the mutual two and three body interactions. On the contrary, the availability of large phase space at relativistic energies ($\geq$ GeV/nucleon) makes the Pauli-blocking [55] an effective (roughly 4% collisions are blocked) and hence the dynamics of a reaction is governed by the cascade picture. On the other hand, both cascade and mean field pictures emerges at intermediate energies. Beside cascade and mean field picture, isospin picture is used to extract the information about equation of state. Isospin degree of the freedom enters via quantities such as the iso-vector (symmetry) potential, and isospin-dependent in-medium nucleon-nucleon (NN) cross-sections and Pauli blocking.

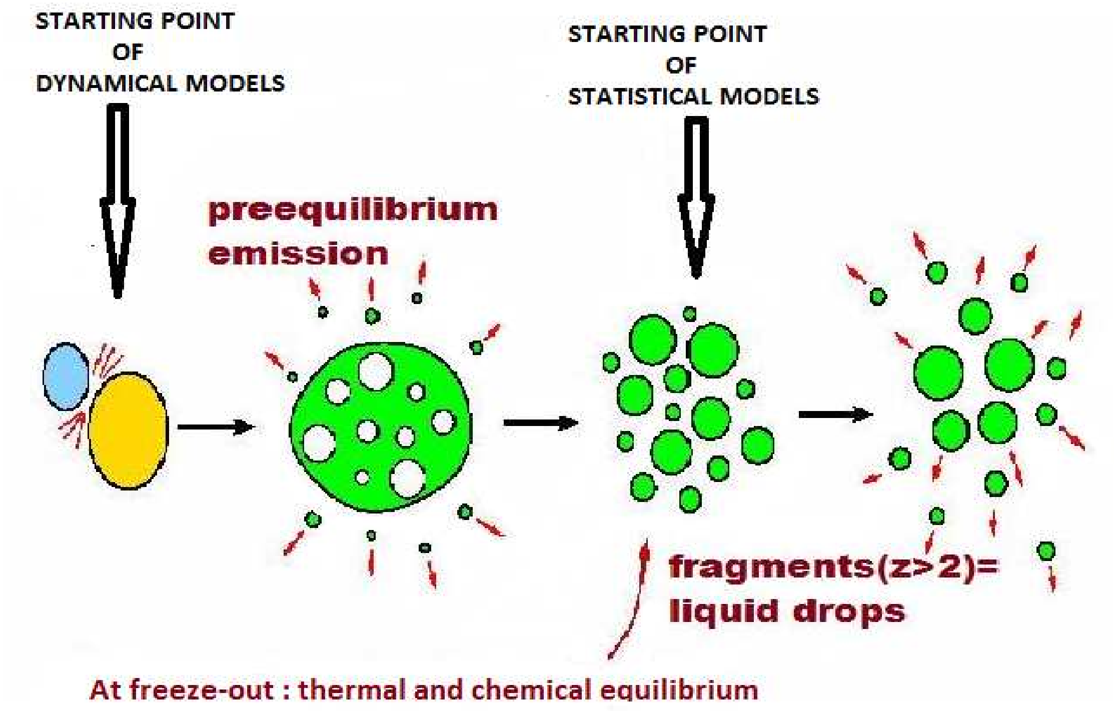

Figure 1.8: Schematic view of various statistical and dynamical models [56].

A native picture of the nuclear reactions at intermediate energies undergoes three important steps:-

- Initial stage where the target and projectile are boosted toward each other with proper center-of-mass energy.
- Compression and expansion stage, after which a pre-fragment source is formed and reaches an equilibrium.

- A secondary decay process of various emitted fragments.

The theoretical models for various processes at intermediate energies can be divided into two categories: Primary models and Secondary models. "Primary models" that generate the phase-space of the nucleons can be group into (i) static or statistical models and (ii) dynamical models. As depicted in Fig.1.8, statistical models rely on the final break-up, neglecting the dynamics of a reaction. On the other hand, dynamical models follow the reaction from two well separated nuclei to the final state where matter is separated, fragmented and cold. Some of the statistical models are based on the droplet description of a nucleus, while the other ones are based on the percolation theory. Examples of statistical models include multi-particle phase space models, such as the *Statistical Multi-fragmentation Model (SMM)* [57-60] and the *Berlin Multi-fragmentation Model (BMM)* [61]. Additional static models include *Percolation* [62], *Lattice Gas (LG) Approach* [63] and *Expanding Emitting Source (EES) model* [64]. These statistical models have been extensively used to study the phenomena of the multi-fragmentation. The limitation of the statistical models are: (i) The situation at the start of a reaction is based on some assumption accounting for the degree of thermalization [57, 60] and (ii) The statistical models give better description only of the final stage of a reaction. Since no dynamical information is possible, these models provide limited information. The study of the dynamics of a reaction including correlations and fluctuations is possible within dynamical model only.

The dynamical approaches such as the *Time Dependent Hartree Fock (TDHF)* [2, 5, 65] or its semi-classical version called *Vlasov equation* (in phase space) [66-70] are suitable at low incident energies where nucleon-nucleon collisions are negligible. However, a suitable and reasonable approach for the intermediate energy heavy-ion physics should treat the nucleon-nucleon scattering and mean field on equal footing. Some attempts were made in the literature to extend the *TDHF* theory to take care of the residual NN interactions, which are responsible for the two-body collisions. This was dubbed as *Extended Time dependent Hartree-Fock (ETDHF)* theory [71]. However, its numerical implementation prohibited its use for large scale investigations of heavy-ion collisions.

In the first attempt, the semi-classical version of *ETDHF* theory i.e. *Vlasov equation* [66-68] was coupled with the nucleon-nucleon collisions and thus, a new realization named as, *Boltzmann -Uehling - Uhlenbeck equation (BUU)*, was developed to study the large deviation problems of low, intermediate and relativistic heavy-ion collisions. The *BUU* equation was solved by the test particle method. The one body distribution function is described as a collection of NA test particles, where A is the mass number and N is event number. All possible collisions between the test particles are considered, i.e., there is no division of the test particles. In other words, N parallel runs communicate with each other, therefore, event by event correlation can not be analyzed.

Keeping in the mind the requirement of intermediate energy region, one would like to have those methods where correlations and fluctuations among nucleon can be preserved. Based on this, these dynamical models are further categorized into Classical Molecular Dynamics and Quantum Molecular Dynamics Models. *Classical Molecular Dynamics (CMD)* [72] approach, in principle, is capable of predicting the fragments production. It also incorporates complete classical N-body dynamics which is necessary to describe the formation of the fragments. The simple Classical Molecular Dynamics model, however, needs major refinements (including quantum features) that play a very important role at low incident energies.

The Classical Molecular Dynamics (CMD) approach was later extended to incorporate the quantum features by Aichelin and Stocker [1, 73]. This new approach, that explicitly incorporates the N-body correlations as well as nuclear matter equation of state and important quantum features (like the Pauli blocking, symmetry potential, nucleon-nucleon cross-section and particle production), was dubbed as *Quantum Molecular Dynamics (QMD)* model [1, 73, 74].

To extract the information of the NEOS of neutron-rich matter, especially the density dependence of the nuclear symmetry energy from heavy-ion reactions induced by the neutron rich (stable and/or radioactive) beams, one needs reliable theoretical tools. For this purpose, one must have transport models that include explicitly the isospin degree of freedom and thus the isospin-dependent physical quantities such as the iso-vector (symmetry) potential and isospin-dependent in-medium nucleon-nucleon (NN) cross-sections and Pauli-blocking. As discussed above, the semi-classical models include mainly the two types: the BUU and the QMD models. With the development of the radioactive ion-beams, several rather comprehensive isospin-dependent, but mostly semi-classical transport model such as IBUU [29], SMF [75] and IQMD [30] have been successfully developed in recent years to describe the nuclear reactions induced by the neutron-rich nuclei at intermediate energies.

The *isospin-dependent Boltzmann-Uehling-Uhlenbeck (IBUU)* transport model has successfully explained several isospin dependent phenomena in heavy-ion collisions at intermediate energies [29]. In this model, the isospin dependence was included in the dynamics through nucleon-nucleon collisions by using isospin-dependent cross-section, Pauli blocking factor, the symmetry potential $V_{sym}(\rho, \delta)$, and the Coulomb potential. This model was used to calculate the ratio of the yield of neutrons and protons in pre-equilibrium emission [76]. The density fluctuations that lead to the fragment production are suppressed in the BUU equation, so the calculation of the fragment yield directly via BUU model is not feasible. Therefore, alternate model such as, *Stochastic Mean Field (SMF)* model [75] and *Isospin Quantum Molecular Dynamics (IQMD)* model [30] have been developed to address the density fluctuations.

The *IQMD* model [30] treats different charged states of the nucleons, deltas and pions explicitly [77], as inherited from the *VUU* model [69, 70]. The isospin degree of freedom enters into the calculations via symmetry potential and cross-sections [69, 70]. This model has been proven to be successful to study the isospin effects in intermediate energy heavy-ion collisions. The model incorporate the N-body correlations, reduces the fluctuations to minimum extent, explains the NEOS and includes the many quantum features like Pauli blocking, Stochastic scattering, particle production and isospin.

All these dynamical models can follow the time evolution of the nucleons only. Now one needs a procedure to define clusters. These algorithms are termed as “secondary models”. In a very simple picture, nucleons are connected to a cluster using the space correlation method. This method identifies two nucleons in a fragment if their centroids are less than some distance. This method is known as *Minimum Spanning Tree (MST)* method [5, 78-81]. Till today, it is one of the most extensively used methods. Several refinements to this method have been proposed including a momentum and binding energy cut [82]. One more and newly developed secondary model is the *Simulated Annealing Clusterization Algorithm (SACA)*, developed by Puri, Hartnack and Aichelin [83, 84], which is based on the minimization of the energy of a system.

As discussed in the above paragraphs, we have several theoretical models that are available to study the heavy-ion collisions at intermediate energies. We shall study the phenomena of multifragmentation and collective flow using the *IQMD* model which generates the phase space of nucleons. The clusterization of the nucleons into fragments is done by secondary models such as minimum spanning tree (MST) and minimum spanning tree with momentum cut (MSTP). The results obtained from these methods are discussed in respective chapters.

The thesis is organized as follows:

In **Chapter 2**, we will describe various theoretical models for one-body distribution function BUU, IBUU and Stochastic Mean Field (SMF) and N-body distribution function QMD and IQMD in brief. The primary model, Isospin-dependent Quantum Molecular Dynamics *(IQMD)* will be discussed in detail in this chapter. In addition, the secondary model or clusterization algorithms such as *MST*, *MSTM* and *SACA*, will also be discussed in brief.

In **chapter 3**, we study the directed flow using a stiff equation of state along with enhanced and reduced isospin-dependent cross-sections (σ= 0.7 to 1.3 σ_{NN}), by simulating various reactions of $^{12}C_6$ + $^{12}C_6$, $^{20}Ne_{10}$ + $^{27}Al_{11}$, $^{40}Ar_{18}$ + $^{45}Sc_{21}$, $^{40}Ar_{18}$ + $^{51}V_{23}$, $^{86}Kr_{36}$ + $^{93}Nb_{41}$, $^{64}Zn_{30}$ + $^{58}Ni_{28}$, $^{93}Nb_{41}$ + $^{93}Nb_{41}$, $^{129}Xe_{54}$ + $^{118}Sn_{50}$, $^{139}La_{57}$ + $^{139}La_{57}$, and $^{197}Au_{79}$ + $^{197}Au_{79}$. The above reactions were simulated between 45 and 200 MeV/nucleon. First of all, we check the effect of cross-section on the number of collision, number of particles in the particular rapidity distribution and on the directed flow. Then transverse momentum $\langle P_x/A\rangle$ is plotted as a function of the rapidity distribution. Also time evolution of directed flow $\langle P_x^{dir}\rangle$ at E=60 MeV/nucleon and E=200MeV/nucleon is studied. After this, we have analyzed the energy dependence of the directed flow. All these parameters are studied for different cross-section and for different systems. A power law behavior is given for the mass dependence of balance energy which also follows the N/Z dependence. Finally, we attempted to fit the observation obtained using reduced isospin-dependent cross-section in the presence of a stiff equation of state with the experimental findings.

In the **chapter 4**, we study the fragmentation of colliding nuclei $^{197}Au_{79} +^{197} Au_{79}$, $^{139}La_{57} +^{139} La_{57}$, $^{93}Nb_{41} +^{93} Nb_{41}$, $^{86}Kr_{36} +^{93} Nb_{41}$, $^{64}Zn_{30} +^{58} Ni_{28}$, $^{40}Ar_{18} +^{45} Sc_{21}$ at, above and below the energy of vanishing flow. The corresponding energy of vanishing flow (EVF) for these system were reported to be 48, 58, 62, 56, 64, 80 MeV/nucleon respectively. Firstly we analyze the time evolution of different fragments A_{max}, free nucleons (FNs) (A=1), light mass fragments (LMFs) ($2 \leq A \leq 4$), medium mass fragments (MMFs) ($5 \leq A \leq 11$) and intermediate mass fragments (IMFs) ($5 \leq A \leq A_{tot}/6$) around the energy of vanishing flow. Then multiplicity of different fragments is plotted as a function of composite mass of colliding nuclei at, above, below and at EVF with $E_{sym} = 0MeV$. Further, we study the average multiplicity of IMFs vs incident beam energy in the reaction ^{86}Kr+^{93}Nb, ^{40}Ar+^{45}Sc at scaled impact parameter $\hat{b} = 0.3$ (semi central collisions) using isospin dependent reduced cross section ($\sigma = 0.9\sigma_{NN}$) and the results are compared with NSCL experimental data.

In **chapter 5**, we study the correlation between balance energy and transition energy of fragments in heavy-ion collisions. In nearly symmetric reactions $^{40}Ar_{18}$ + $^{45}Sc_{21}$, $^{93}Nb_{41}$ + $^{93}Nb_{41}$, $^{139}La_{57}$ + $^{139}La_{57}$, and $^{197}Au_{79}$ + $^{197}Au_{79}$, we have analyzed the transverse momentum dependence of elliptical flow and anisotropy ratio for different fragments i.e. FNs (A=1), LMFs* ($1 \leq A \leq 4$) and for LMFs ($2 \leq A \leq 4$) using a hard equation of state along with isospin-dependent reduced cross sections (σ= 0.9 σ_{NN}) at incident energies between 40 and 1200 MeV/nucleon. Then system mass dependence of transverse momentum is explained, after this the correlation between transition energy and balance energy is shown as their difference decreases with an increase in the total mass of colliding nuclei. This dependence is fitted with the power law. Moreover, to observe the transition from in-plane to out-of-plane emission, energy dependence of elliptical flow is shown for different systems and for different fragments. At last results are compared with the experimental data of different collaboration for $^{197}Au_{79}$ + $^{197}Au_{79}$ system at impact parameter (b=5 fm) for Z=2 particles.

In **chapter 6**, we discuss the multifragmentation using a soft equation of state along with enhanced and reduced clusterization range (R_{clus}) and momentum constraints (P_{clus}) with (σ= 0.9 σ_{NN}) at incident energies between 35 and 200 MeV/nucleon. Since we are interested to predict the clusterization range for which systematic trend of $\langle M_{IMF} \rangle$ is obtained at different values of P_{clus} and also to predict momentum constraints at which the multiplicity of IMF $\langle M_{IMF} \rangle$ remains same for fix value of R_{clus}. For this, first of all, we analyze the multiplicity of different fragments A_{max}, FNs, LMFs and IMFs as a function of P_{clus} and R_{clus} for different systems at energy 150 and 200 MeV/nucleon. We observe that multiplicity of various fragments saturates for P_{clus} = 240 MeV/c and R_{clus} = 4 fm for various systems. To further clarify our results we discuss the mean multiplicity of intermediate mass fragments $\langle M_{IMF} \rangle$ as a function of Z_{bound} for the reaction of ^{197}Au on ^{197}Au at E/A=400 MeV. For R_{clus} = 4 fm there is a systematic trend for different value of P_{clus} compared to other clusterization parameters. For this clusterization range there is no change in production of $\langle M_{IMF} \rangle$ above P_{clus} = 240 MeV/c. Energy dependence and time dependence of different fragment for different systems is also studied for the predicted value of P_{clus} and R_{clus}. Finally we see that our results for $^{197}Au +^{197} Au$ collisions are in good agreement with the experimental data of ALADIN data and for $^{129}Xe +^{139} La$, $^{86}Kr +^{93} Nb$, $^{40}Ar +^{45} Sc$ with the NSCL data.

In **chapter 7**, we analyze the results by optimizing the scaled Gaussian width (SGW) for different colliding nuclei. Since we are interested to find Gaussian width which show stability for all colliding nuclei in IQMD model. For this, we analyze the results of root mean square radii of Ca and Au as a function of time for different scaled Gaussian width (SGW). Then we noted the range of SGW from time evolution of largest fragment and see its effect on balance energy which is extracted from $\langle P_x/A \rangle$ and $\langle P_x^{dir} \rangle$. The energy at which slope of rapidity distribution $\langle P_x/A \rangle$ approaches to zero is the balance energy. The energy dependence of directed flow is displayed for different system for SGW range which is then compared with the experimental data. At last, multiplicity of IMFs as a function of beam energy and Z_{bound} for different systems for SGW range is analyzed. This range is then compared with the experimental data of ALADIN and NSCL.

Our results are summarized in **chapter 8**, which also contains an outlook of the work.

Chapter 2

Methodology

2.1 Introduction

The system will reach hydrodynamic regime when equilibration is fast and local equilibrium is reached in the course of the reaction. This offers tremendous theoretical simplification, since it allows a quasimacroscopic description. This treatment of heavy-ion collisions was the first to predict nucleonic collective behavior [49, 85]. However, it soon became clear that the assumption of instantaneous local equilibrium in ideal fluid hydrodynamics is not fulfilled in heavy-ion collisions. While the theory can be saved to certain extent by the introduction of different fluids, representing target, projectile and participant matter individually [86], comparison to the data required even more sophistication with the introduction of viscosity [87] and freeze-out concepts [16, 88]. To overcome the growing complication caused by the macroscopic Ansatz of hydrodynamics, models based on the superposition of individual NN collisions were developed. This started with the simple case of overlaying independent NN collisions [89]. Because the conventional mean field theory [2, 90] like the Hartree-Fock and Schröedinger equation are suitable for the low energy reactions. On the other hand, contrary to the TDHF approach, the cascade model [89, 91] describes very high energy heavy-ion collisions. It neglects mean field completely and take only nucleon-nucleon collisions without Pauli-blocking into account. The dynamics at intermediate energies, however, requires the equal weightage to nucleon-nucleon binary and mean field. This demands exact information about the real (trajectory of nucleons) and imaginary (nucleon-nucleon collisions) parts of the potential. Furthermore, to extract the information of the nuclear equation of state (NEOS) from heavy-ion reactions, one must include explicitly the isospin degree of freedom. This isospin degree of freedom enters into real and imaginary parts in term of isovector (symmetry) potential, isospin-dependent in-medium nucleon-nucleon cross-sections, and Pauli-blocking, respectively. In addition, one has also to start from the initial state (where matter is non-equilibrated) to the final state (where matter is cold and fragmented). The dynamical transport models employed at intermediate energies are supposed to include essential collision physics. These dynamical models at intermediate energies can be subdivided into two classes: Those which follow the time evolution of the one-body phase space distribution i.e. VUU type, IBUU and SMF and those which are based on N-body molecular dynamics or cascade schemes i.e QMD and IQMD. In the present chapter, we shall explain IQMD model in detail. Some secondary clusterization algorithms shall also be explained.

2.2 Boltzmann-Uehling-Uhlenbeck (BUU) model

Any model derives its strength from its ability to reproduce experimental quantities when initial condition are varied. For example, experimental measurement show how multiplicity of fragments varies with mass, impact parameter as well as with incident energy. A model that claims to simulate accurately fragmentation in nuclear collisions must reproduce these dependencies. A numerical implementation of the Boltzmann-Uehling-Uhlenbeck (BUU) model [92, 93] has been successful in reproducing various collective flow phenomena such as balance energy. These transport models for the one-body Wigner phase space density distribution obtained different names although they solve the same equation. They differ in the technical realization, i.e. the computer program, and are known as BUU model [69, 94] or Vlasov-Uehling-Uhlenbeck, Landau-Vlasov (VUU[66, 95], LV [96]). Any one-body observable can be calculated by averaging the values weighted with the distribution function. In brief, the BUU model is useful when the behavior of the nuclear matter collectively is of interest; however, BUU model does not coalesce nucleons into fragments and therefore is not suited for the study of fragmentation. The recent developments in the BUU model incorporate the momentum dependent potential [68, 97-99] isospin dependent potential as well as isospin dependent nucleon-nucleon (NN) scattering cross section [29]. In order to study, isospin effects in neutron-rich systems, for one-body distribution function, the BUU model with isospin effects and *Stochastic Mean Field (SMF)* [75] is used in literature. Additionally, for N-body distribution, *isospin dependent quantum molecular model (IQMD)* [30] is used. These models are discussed later in the coming sections.

2.2.1 Isospin-dependent Boltzmann-Uehling-Uhlenbeck (IBUU) Model

In IBUU model [29], just like BUU model [66, 95], the Boltzmann-Uehling-Uhlenbeck equation describes the time evolution of the single particle phase-space distribution function and reads as follow:

$$\begin{aligned} \frac{\partial f_1}{\partial t} + v \cdot \nabla_r f_1 - \nabla_r U \cdot \nabla_p f_1 &= \int \frac{d^3\acute{p}_1 d^3 p_2 d^3 \acute{p}_2}{(2\pi)^9} \sigma_{12} v_{12} (2\pi)^3 \delta^3 (p_1 + p_2 - \acute{p}_1 - \acute{p}_2) \\ &\times \left[\acute{f}_1 \acute{f}_2 (1 - f_1)(1 - f_2) - f_1 f_2 (1 - \acute{f}_1)(1 - \acute{f}_2) \right]. \end{aligned} \tag{2.1}$$

Here σ_{12} is the differential cross-section for a certain change of momentum $(p_1, p_2) \rightarrow (\acute{p}_1, \acute{p}_2)$ and v_{12} is the relative velocity for the colliding nucleons.

The isospin dependence comes into the model by both the elementary NN cross-section σ_{12} and the nuclear mean field U. In this model, experimental NN cross-sections with the explicit isospin dependence are taken into account [100]. The isospin dependence is due to the fact that the cross-section of neutron-proton is about three times that of the neutron-neutron or proton-proton cross-section. In this model, U is the mean field, which is a function of the local density. It can be parametrized as an arbitrary function of the density, making possible to model a variety of equations of state. Typically, it can be written as, the sum of three terms:

$$U = V_{Coul} + V_N + V_{Sym}, \tag{2.2}$$

where V_{Coul}, V_N and V_{Sym} represents the Coulomb, iso-scaler nucleon potential and the symmetry energy, respectively. The nuclear mean field U including the isospin symmetry term is parametrized as:

$$U(\rho, \tau_z) = \alpha \left(\frac{\rho}{\rho_0} \right) + \beta \left(\frac{\rho}{\rho_0} \right)^{\gamma} + (1 - \rho_0) V_{Coul} + C \frac{\rho_n - \rho_p}{\rho_0} \tau_z. \tag{2.3}$$

Here ρ_0 is the normal nuclear matter density, ρ, ρ_n and ρ_p are the nucleons, neutron and proton densities, respectively. τ_z equals to +1 or -1 for neutrons or protons, respectively. The V_{Coul} as discussed above is the Coulomb potential. Other forms of the parametrization for mean fields which corresponds to probably more complete form of Skyrme forces are also possible [101]. The Skyrme term comes from averaging over the constituent two-body forces with Heisenberg component proportional to $(\tau_i,\ \tau_j)$ [102]. Its strength C can be deduced from experiments (e.g. nuclear symmetry energies, optical potentials for nucleon scatterings, excitation of analog states in (p,n) reactions). However, the strength deduced vary significantly from reaction to reaction and also depends on the energy of nucleon [102].

This model provides an accurate description of the time dependence of the one-body distribution function. Accurate solution of the BUU equation average away fluctuations in the density that might lead to the formation of fragments in an individual collision. This is usually achieved by solving the BUU equation with a large number of test particles per nucleon N_{test}. The density fluctuations that lead to the fragment production are suppressed in the BUU equation, so the calculation of fragment yield directly via $IBUU$ model is not feasible. Therefore, alternate model such as, *Stochastic Mean Field (SMF)* model [75] is used to overcome this limitation.

2.2.2 Stochastic Mean Field (SMF)Model

SMF model [75], like, IBUU [29] describes the time evolution of the collision using a self-consistent mean field. In this model, fluctuations and asymmetry effects [103] are included. A density-dependent symmetry term is also used in the ground state construction of the initial condition i.e. isospin effects on the nucleon-nucleon cross-section and Pauli-blocking are consistently evaluated. The nucleon-nucleon mean field including the isospin asymmetry is parametrized as:

$$U(\rho) \;=\; \alpha\left(\frac{\rho}{\rho_0}\right) \;+\; \beta\left(\frac{\rho}{\rho_0}\right)^{\gamma} \;+\; C(\rho)\left(\frac{\rho_n-\rho_p}{\rho_0}\right)\tau_z. \tag{2.4}$$

Here, α, β and γ have their usual meanings as in QMD model. In this model, two different choices for the density dependence of symmetry term is used:

$C \;=\; 32\; MeV$; ASY-STIFF choice,

$C/\rho_0 \;=\; a \;+\; b\rho$ with $a \;=\; 481.7$ MeV fm^3, $b \;=\; -1638.2$ MeV fm^6: ASY-SOFT choice.

These two parametrizations give close values for the symmetry at normal nuclear matter density $\rho_0 \;=\; 0.17\; fm^{-3}$. In the lower density region, they are quite similar, while, at higher densities, the difference is observed. The asy-soft symmetry energy shows a decrease and it changes sign at density $\rho \;\approx\; 2\rho_0$. Moreover, the difference between the asy-stiff and asy-soft increases for large asymmetries [75].

For the reaction mechanisms like fragmentation and deep inelastic scattering, it is quite important to have a dynamical approach that includes fluctuations in a consistent way. In this SMF approach, fluctuations are introduced in two different approaches just starting from a local equilibrium assumption in a phase space cell [103]. In the first approach, a fluctuation term is added to the standard Boltzmann-Nordeim-Vlasov (BNV) equation to account for the stochastic force, the strength of which is adjusted to reproduce the growth of the most important unstable mode in the system. In practical term, the stochastic force is a type of stochastic noise. The second approach uses this fact by approximating it with numerical noise caused by solving BUU with a small number of test particles (i.e. $N_{test} = 50$) per nucleon.

Keeping in mind the requirement of intermediate energy region, one would like to have method where correlations and fluctuations among nucleon can be preserved. SMF, like, IBUU model is suitable to explain one-body observable like collective flow indicating correlations are not preserved among the nucleons. In the following, we describe in detail the *Quantum Molecular Dynamics (QMD)* model [5, 30, 74, 104, 105] which is an N-body model.

2.3 Quantum Molecular Dynamics (QMD) Model

The classical molecular dynamics (CMD) approach, which is a true N-body theory, is capable of treating both the compression and fragments formation, but on a completely classical level: the Hamilton's equation of motion are integrated for N classical point particles, with finite range nucleon-nucleon potential. Based on the CMD approach, Aichelin and Stöcker [95, 106], designed a novel method that incorporates N-body correlations, an equation of state and most important quantum features, namely, the Pauli-principle, Stochastic scattering as well as particle production. It is based on an event by event method. Here each event is simulated independent of other events. In contrast to BUU model, no averaging is done over various events and hence, the correlations among nucleons can be preserved. The most widely used microscopic models for the description of heavy-ion collisions were based on the Vlasov-Uehling-Uhlenbeck (VUU) theory [69, 94], which explicitly treats non-equilibrium and (stochastic) quantum effects in the framework of one particle quantities, as well as nuclear potential/equation of state (NEOS). However, certain fluctuations and correlations, such as the formation of fragments in heavy-ion collisions, can not be studied with a transport model based on a single particles distribution function. This was one of the motivations for the development of the Quantum Molecular Dynamics (QMD) model [5, 30, 74, 104, 105].

The quantum molecular dynamics model is based on the molecular dynamics picture where nucleons interact via two and three-body interactions. The explicit two and three-body interactions lead to the preservation of the fluctuations and correlations which are important for N-body phenomena like multifragmentation.

In QMD, the successfully initialized nuclei are boosted towards each other with proper center-of-mass velocity using relativistic kinematics. Here each nucleon is represented by a Gaussian wave packet with a width $\sqrt{L}$ centered around the mean position $\vec{r}_i$(t) and the mean momentum $\vec{p}_i$(t):

$$\psi_i(r,\ p_i(t),\ r_i(t)) \ = \ \frac{1}{(2\pi L)^{3/4}} exp\left[\frac{i}{\hbar}\ p_i(t)\cdot r\ -\ \frac{(r\ -\ r_i(t))^2}{4L}\right]. \tag{2.5}$$

The Wigner distribution of a system with $A_T + A_P$ nucleons is given by

$$f_i(r,\ p, r_i(t),\ p_i(t)) \ = \ \frac{1}{(\pi\hbar)^3} e^{-(r\ - r_i(t))^2/2L}\ e^{-(p\ - p_i(t))^2 2L/\hbar^2}, \tag{2.6}$$

with $L = 1.08 fm^2$. The total Wigner density is the sum of all those nucleons. The Gaussian width for a particular nucleon is chosen in a way so that maximum stability of the nucleonic density profile can be achieved. In QMD model Gaussian width used is 4.33 fm^2 for all the nuclei in periodic table. The centroid of each wave packet propagates under a classical equation of motion [5, 74, 104, 107]:

$$\dot{p}_i \ = \ -\frac{\partial\langle H\rangle}{\partial r_i}\ ;\ \dot{r}_i \ = \ \frac{\partial\langle H\rangle}{\partial p_i}, \tag{2.7}$$

where the Hamiltonian is given by

$$\begin{aligned}\langle H\rangle &= \langle T\rangle + \langle V\rangle \\ &= \sum_i \frac{p_i^2}{2m_i} + V_{Skyrme} + V_{Yuk} + V_{Coul} + V_{MDI}.\end{aligned} \tag{2.8}$$

Here V_{loc} , V_{Coul} , V_{Yuk} , and V_{MDI} are, respectively, the local Skyrme, Coulomb, Yukawa, and Momentum Dependent Interactions (MDI). The Yukawa interaction is essential for the surface effects. The momentum dependent part of the interaction which is obtained by fitting the real part of the optical potential acts strongly in the cases where the system is mildly excited [5, 74, 104, 108-110]. In this case, the MDI is reported to generate more fragments compared to the static equation of state. For a detailed discussion of the different equations of state and momentum dependent interactions the different form of nucleon-nucleon cross section and their effect on different observables [5, 40, 41, 42, 74, 104, 108-113] is studied in literature.

If two nucleons come closer than distance $\sqrt{\frac{\sigma^{tot}(\sqrt{s})}{\pi}}$ they are bound to collide depending upon the available phase space. In recent years, several refinement and improvements were made over original QMD model. The new versions were named as *MQMD* [114], *HQMD* [30], *PQMD* [115], *BQMD* [30], *Urqmd* [116], *IQMD* [30], *G-Matrix QMD* [117], *Glauber* *plus QMD(DQMD)* [118] etc. Apart from QMD and its modified versions, there are other dynamical models, which can also used for the study of heavy-ion collisions at intermediate energies. The crucial quantum features like the antisymmetrisation were implemented in approaches like *FMD* [119] and *AMD* [120], which is further modified by including the stochastic incorporation of the diffusion and the deformation of wave packet [121]. Recently the improved version of AMD [122] was used to show the cluster-shell competition of these nuclei. However the use of AMD and FMD models are restricted, due to serious numerical problems, to light systems only. To study the fermionic nature of N-body system, new microscopic model, dubbed as *Constrained molecular dynamics (CoMD)*, was also proposed in Ref.[123]. In order to include both correlations and fluctuations with isospin effects, one must have some other dynamical model. This dynamical model, which explicitly incorporates the N-body correlations as well as nuclear mater equations of state and important quantum features (like Pauli Blocking, Stochastic scattering, particle production and isospin effects) is dubbed as *Isospin-dependent quantum molecular dynamics (IQMD)* model [30]. This model is developed by Ch. Hartnack and collaborators in 1998. In the following section, we will explained this model in detail.

2.4 Isospin-dependent Quantum Molecular Dynamics (IQMD) Model

In IQMD model [30] isospin is treated explicitly by incorporating a symmetry potential (to achieve corrected distributions of protons and neutrons in the nucleus) and explicit Coulomb forces between the Z_P and Z_T protons are included. The IQMD [30] model treats different charge states of nucleons, deltas and pions explicitly [77], as inherited from the VUU model [69, 94]. The IQMD model has been used successfully for the analysis of large number of observable from low to relativistic energies [30, 107]. The IQMD model is a nonequilibrium transport model which considers the isospin degree of freedom for nucleon-nucleon cross-section, the Coulomb interaction, the Yukawa potential, and the momentum dependence of the interaction [92, 124, 125]. In the model, the nucleons are represented by Gaussian wave packet and classical equation-of-motion are used to propagate their centroids in an interaction potential. In the potential, there is a local term which can be parametrized with a potential depending on the density and this allows a direct connection to nuclear Equation-of-State. The calculation are based on event-by-event and the reaction are treated as binary collisions between nucleons with Pauli exclusion principle. This model includes

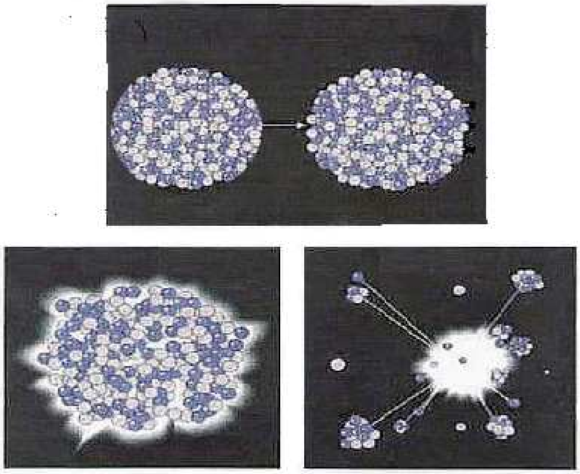

Figure 2.1: Diagramatic representation of three steps in IQMD model.

three important steps:

1. First, one has to generate projectile and target. This procedure is called **initialization**. It becomes very important to make sure that our initialization produce reasonably stable nuclei. For this, we will discuss some *initial checks for the stability of the nuclei.*

2. In the second step, nuclei propagate under the influence of surrounding mean field. This is termed as **propagation**.

3. Finally, nucleons are bound to collide if they come too close to each other. This part is dubbed as **collisions**.

In the Fig.2.1, these three steps are picturised. The elastic and inelastic cross-sections for proton-proton, neutron-neutron as well as proton-neutron are supposed to be affected in the presence of isospin. The details for these cross-sections will also be discussed in the last step. In the following, we shall discuss all of these parts in detail.

2.4.1 Initialization

In this model, baryons are represented by Gaussian-shaped density distributions as described in Eqn.(2.6). Where, Gaussian width L is regarded as a description of the interaction range of particle. The system dependence of L has been introduced in IQMD in order to obtain maximum stability of the nucleonic density profiles. For the heavier system (e.g. Au + Au), its value is chosen 8.66 fm^2, while for lighter one (i.e. Ca + Ca), the value is 4.33 fm^2. In the present thesis, we enhance and reduce the Gaussian width from normal Gaussian width and noted the range (lower-higher) from the time evolution of largest fragment and see its effect on balance energy and multifragmentation.

Nucleons are initialized in a sphere with radius $R = 1.12A^{1/3}$ fm, in accordance with the liquid drop model. Each nucleon occupies a volume of h^3, so that phase space is uniformly filled. The initial momenta are randomly chosen between 0 and Fermi momentum(p_F), without any further local constraints. The Fermi momentum p_F depends on the ground state density. For $\rho_0 = 0.17\ fm^{-3}$, it has a value of about 268 MeV/c. Moreover, the IQMD model performs a Lorentz contraction of the nucleus coordinate distribution, which becomes important at the higher energies. The nuclei prepared within transport model may start emitting nucleons after the lapse of hundred fm/c. Therefore, it is very important to make sure that our initialization does not destabilize the cold nuclei. The stable fragments formation take place if the interaction among the nucleons ceases to exist. Extensive tests were conducted by *Heidelberg-Nantes-Frankfurt-Tubingen-Chandigarh* groups to study the properties of different single nuclei. The nucleons inside a nucleus move under the influence of the mean field of their neighbors. During the motion whenever a nucleon come close to the surface of the nucleus, it is pulled back by other nucleons. Thus every nucleon remains confined in a sphere as shown in Ref. [5, 74, 104, 126]. Due to the local density approximation used here, the lighter nuclei are unstable compared to heavier one. Frankfurt group [115] showed that inclusion of Pauli-potential in the mean field keeps the nucleon stable for several thousand fm/c. Nantes Group [5, 74, 104] checked the stability in term of root mean square (r.m.s) radius as well as binding energy. We have also carried out various checks by calculating the binding energy and r.m.s radius of different nuclei as well as propagation of heaviest fragment. Most of the nuclei were found to be stable for couple of hundred fm/c, which is long enough for the present purpose.

2.4.2 Propagation

The successfully initialized nuclei are then boosted towards each other with proper center of mass velocity using relativistic kinematics. The nucleons of target and projectile interact via two and three-body Skyrme forces, a Yukawa potential and momentum dependent interactions. The isospin degree of freedom is treated explicitly by employing a symmetry potential and explicit Coulomb forces between protons of colliding target and projectile. This helps in achieving correct distribution of protons and neutrons within nucleus.

The hadrons propagate using Hamilton equations of motion as described in Eqn.(2.7) and Eqn.(2.8). The baryon-baryon potential $\langle V \rangle$, in the Eqn.(2.8) is written as:

$$
\begin{aligned}
\langle V \rangle &= V_{Skyrme} + V_{Yuk} + V_{Coul} + V_{MDI} + V_{Sym} \\
&= \left(t_1 \delta(r' - r) + t_2 \delta(r' - r) \rho^{\gamma - 1} \left(\frac{r' + r}{2} \right) \right) \\
&\quad + t_3 \frac{exp(|r' - r|/\mu)}{(|r' - r|/\mu)} + \frac{Z_i Z_j e^2}{|r' - r|} \\
&\quad + t_4 \ln^2 [t_5 (p_i{}' - p)^2 + 1] \delta(r' - r) \\
&\quad + t_6 \frac{1}{\varrho_0} T_3^i T_3^j \delta(r_i{}' - r_j). \qquad (2.9)
\end{aligned}
$$

Here Z_i and Z_j denote the charges of i^{th} and j^{th} baryon, and T_3^i, T_3^j are their respective T_3 components (i.e. 1/2 for protons and -1/2 for neutrons). The finite range Yukawa potential with $t_3 =$ -6.7 MeV is important to stabilize the surface of a finite nucleus. Meson potential consists of Coulomb interaction only. The parameters μ and $t_1, ..., t_6$ are adjusted to the real part of the nucleonic optical potential. Other baryonic potentials like V_{Skyrme} and V_{MDI} are isospin-independent. For the density dependence of nucleon optical potential, standard Skyrme-type parametrization is employed.

Two different NEOS have been implemented (as discussed in chapter 1): A hard NEOS with a compressibility of 380 MeV and a soft NEOS with a compressibility of 200 MeV [5, 74, 104]. The Yukawa potential (V_{Yuk}) in IQMD is very short ranged (μ = 0.4 fm in contrast to μ = 1.5 fm in QMD) and weak. Yukawa forces also stabilize the nuclei because of the increase of the interaction range as compared to a δ-like Skyrme potentials. This results in the reduction of fluctuations.

2.4.3 Nucleon-Nucleon (NN) Collisions

The binary nucleon-nucleon collisions are included by employing the collision term of well known VUU-BUU equation [69, 94]. The binary collisions are done stochastically, in a similar way as are done in all CASCADE models [89, 127]. During the propagation, two nucleons are supposed to suffer a binary collision if the distance between their centroids

$$|r_i - r_j| \leq \sqrt{\frac{\sigma_{NN}}{\pi}}, \sigma_{NN} = \sigma(\sqrt{s}, type). \tag{2.10}$$

Here the $\sigma_{NN}(\sqrt{s})$ represents the total NN cross section and '$\sqrt{s}$' is the center-of-mass energy. "type" denotes the ingoing collision partners (N-N, N-Δ, N-π,..). In addition, Pauli blocking (of the final state) of baryons is taken into account by checking the phase space densities in the final states. The final phase space fractions P_1 and P_2 which are already occupied by other nucleons are determined for each of the scattering baryons.

2.4.4 Pauli-blocking

The Pauli-blocking is very important quantum feature of any dynamical model to understand the exact reaction mechanism. Whenever a collision occurs, the phase space around the scattering partners is checked. For simplicity, we assume that each nucleon occupies a sphere in coordinate and momentum space. This trick yields the same Pauli blocking ratio as an exact calculation of the overlap of the Gaussian, will yield. We calculate the fractions P_1 and P_2 of final phase spaces for each of the two scattering partners that is already occupied by other nucleons. The collision is then blocked with probability

$$P_{block} \ = \ 1 - (1 - P_1)(1 - P_2), \tag{2.11}$$

and, correspondingly, is allowed with probability $1 - P_{block}$. For a nucleus in its ground state, we obtain an averaged blocking probability $< P_{block} >$ of 0.96. For absolute blocking, this factor should be one. From above description, it is clear that the Pauli factor will be zero or one depending whether the final phase-space is occupied or not. This sharp occupancy is valid for the cold nuclear matter only. With the passage of time, Puri *et al.* [128] for the first time included the temperature by smearing the Fermi spheres for Pauli-operator. The impact of in-medium corrections is drastic at low energies. With increase in the incident energy, these effects start washing out and thus, the in-medium cross section approaches the free nucleon-nucleon cross section. The pictorial view of Pauli- blocking is shown in Fig.2.2, indicating the more Pauli-blocking effect at low incident energies as compared to high incident energies.

Furthermore, parametrized free *pn* and *pp* cross-sections are used instead of an averaged nucleon-nucleon cross-sections. The respective strength of different cross-sections in shown in Fig.2.3. The total cross-section is the sum of the elastic and all inelastic cross-sections

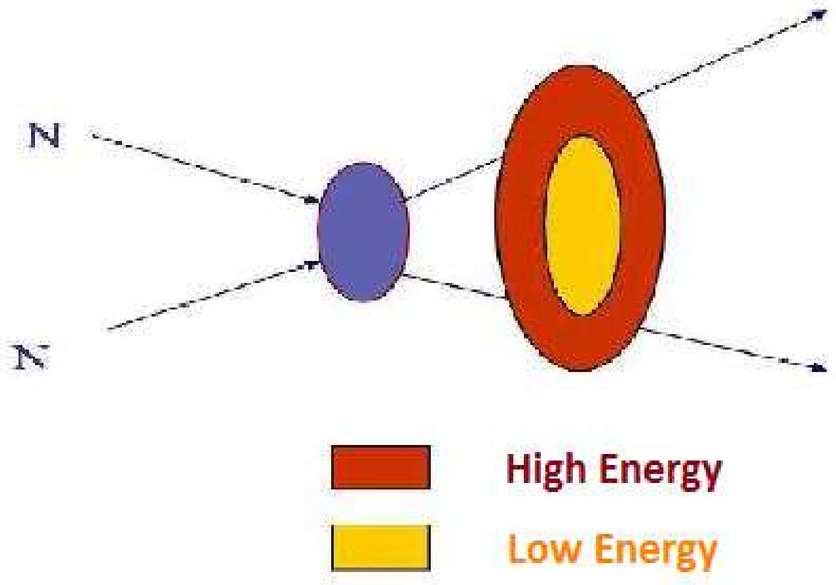

Figure 2.2: Pictorial view of Pauli-blocking at low and high incident energies [129].

$$\sigma_{NN} \;=\; \sigma_{el} \;+\; \sigma_{inel} \;=\; \sigma_{el} \;+\; \Sigma_{channels}\sigma_i. \tag{2.12}$$

The following inelastic reactions might influence the dynamics of the collision and are explicitly taken into account:

$$\begin{aligned}
&N + N \rightarrow\; \Delta + N \; (hard - delta\; production) && (a),\\
&\Delta \rightarrow\; N + \pi \; (delta\; decay) && (b),\\
&\Delta + N \rightarrow\; N + N \; (delta\; absorption) && (c),\\
&N + \pi \rightarrow\; \Delta \; (soft - delta\; production) && (d).
\end{aligned} \tag{2.13}$$

Experimental cross-sections are used for processes (a) and (d) [130], as well as for the elastic NN collisions. Inaccessible reactions like ΔN$\rightarrow$ NN are calculated from their reverse reactions(here $NN \;\rightarrow\; \Delta N$) using modified detailed balance formula [131]. The conventional detailed balance formula is only correct for particles with infinite lifetimes (zero width). The elastic nucleon-nucleon scattering angular distribution is taken to be [132]

$$\frac{d\sigma_{el}}{d\Omega} \;\approx\; exp\,[A(s), t]\,, \tag{2.14}$$

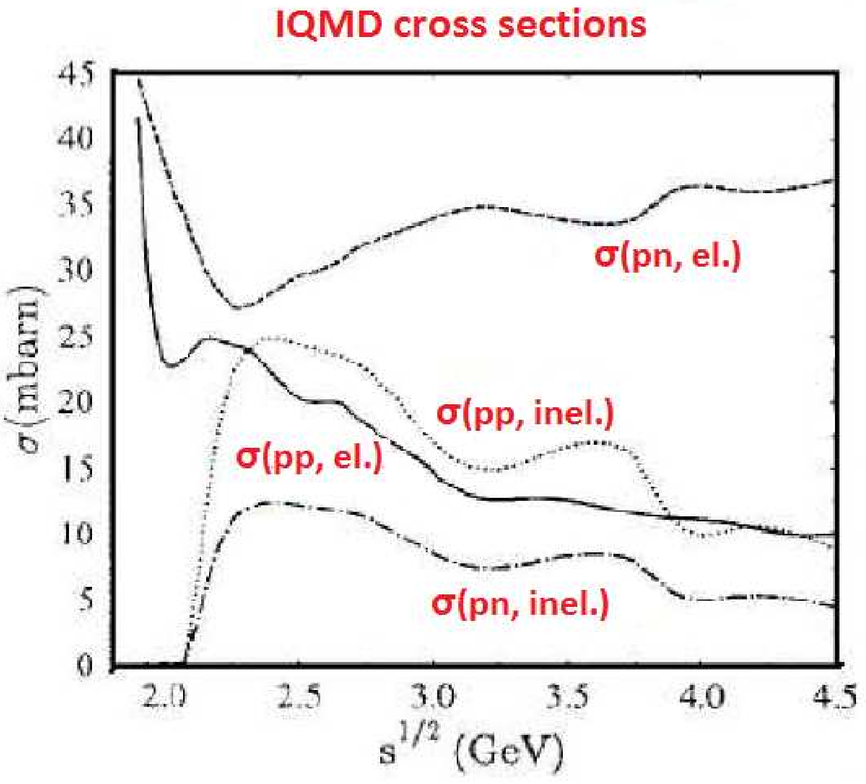

Figure 2.3: The elastic and inelastic cross-sections for proton-proton (pp) and proton-neutron (nn) used in IQMD. The neutron-neutron (nn) cross-section is assumed to be equal to pp. The total cross-section is equal to sum of elastic and inelastic cross-section. This figure is taken from Ref. [56].

where t is $-q^2$, the transverse momentum transfer and

$$A(s) \;=\; 6\frac{[3.65\,(\sqrt{s}-1.8766)]^6}{1+[3.65\,(\sqrt{s}-1.8766)]^6}, \tag{2.15}$$

$\sqrt{s}$ is the c.m. energy in GeV and A is given in $(GeV/c)^{-2}$.

The isospin degree of freedom play an important role especially for the particle production. The employed inelastic channels $NN \rightarrow NN^*$,$N\Delta$ and $\Delta\Delta$ are treated in an analogous fashion. The parametrization suggested by Huber and Aichelin [133] is used: fitted differential cross-sections are extracted from one-boson-exchange (OBE) calculations:

$$\frac{d\sigma_{in}}{d\Omega} \;\approx\; a(s)exp\,[b(s)cos\theta]\,. \tag{2.16}$$

The $a(s)$ and $b(s)$ are functions of $\sqrt{s}$ and vary in their definition for different intervals of $\sqrt{s}$ (see table 2.1). θ is the polar angle.

These isospin effects in the IQMD are found to vary the results, one obtained with QMD model. In the following, the importance of IQMD over QMD model is discussed.

Table 2.1: a(s) and b(s) as a function of the c.m. energy

$x\ =\ \sqrt{s}\ (GeV)$	$a\ (fm)$	b
2.104 - 2.12	$294.6(x-2.014)^{2.578}$	$19.71(x-2.014)^{1.551}$
2.12 - 2.43	$\frac{0.01224}{(x-2.225)^2\ +\ 0.004112}$	$19.71(x-2.014)^{1.551}$
2.43 - 4.50	$\left(\frac{2.343}{x}\right)^{43.17}$	$33.14\ arctan(0.5404(x-2.146)^{0.9784})$

2.5 Importance of IQMD over QMD

The importance of explicit isospin treatment can be seen in Fig.2.3 [130]. The dotted line depicts the results of a QMD calculations without explicit isospin treatment. Average charges are distributed over all nucleons and the inelastic $NN \rightarrow\ N\Delta$ channel is also isospin averaged. Therefore, the neutron to proton ratio must remain constant at 1.5 for $Au\ +\ Au$ independent of transverse momentum and beam energy. The respective IQMD calculations, however, yield a totally different results. The neutron to proton ratio decreases with increasing transverse momentum due to Coulomb interactions. Apart from the p_t dependence also a strong dependence on the incident energy is observed. Due to the explicit inclusion of isospin into the inelastic channels with energy dependent branching ratios, the n/p ratio decreases with increasing beam energy.

The above mentioned models are "primary models" that are used to generate the phase-space of nucleons. As mentioned in chapter 1, we need to have "secondary models" to clusterize the nucleons into fragments. These clusterization methods are discussed briefly in the following section, while, detail is given in the respective chapter, where they are used.

2.6 Secondary models: methods of clusterization

The **Minimum Spanning Tree (MST)** method is the most extensively used to clusterize the nucleons [5, 78-81]. In **MST** method, two nucleons share the same fragment if their centroids are closer than a certain distance. An improvement over the **MST** algorithm, is to put additional cut in momentum space [110, 134]. This method is dubbed as **MSTP**. These two methods are discussed in detail in chapter 6 where restriction is put on spatial arrangement (MST) of nucleons and also on the momentum space of nucleons (MSTP). It will help to get rid of fragments that although close in spatial space are far in momentum space. As mentioned in the above clusterization methods, it is fairly straightforward to determine the cluster structure of a system, i.e. the particle number and velocity of each product. In practice, however, the additional running time required to reach this stage limits the practical utility of the model. It has been, therefore, of interest to devise methods for recognizing the clusters as early as possible. It is worth mentioning that it may also help to elucidate the mechanism of fragment production. A novel algorithm, namely, **Simulated Annealing Clusterization Algorithm (SACA)**, developed by Puri *et al.* [81, 83, 84, 135] was based on the fact that at any given moment of the reaction, the configuration corresponding to largest binding energy is realized in nature. But, since it is very time consuming so clusterization of fragment is done by **MST** and **MSTP** method.

In summary, we discussed the details of various models in this chapter. In the following chapters, we shall present the detailed analysis of multifragmentation using MST method. Apart from this, effect of mass asymmetry, within **IQMD** model, on the directed transverse flow, elliptical flow and multifragmentation will be discussed. Our results are also compared with the experimental data of ALADIN, NSCL, INDRA@(GSI+GANIL), FOPI, MSU, Plastic ball collaborations for multifragmentation and collective flow.

Chapter 3

Effect of isospin-dependent nucleon-nucleon cross-section on directed flow

3.1 Introduction

The outcome of a heavy-ion collision at intermediate energies is not only of importance for nuclear physics, but is also of importance for astrophysics and cosmology. The heavy-ion physics branch has renewed interest recently. This ranges from the fusion probabilities [136] to symmetry energy dependence at intermediate energies as well as the fragmentation of colliding matter [79, 110, 135, 137, 138]. Among various phenomena, one observable that was used extensively for extracting the information from heavy-ion collisions is the collective in-plane flow of various particles [28, 99, 139-148]. Apart from the transverse in-plane flow, other observables that were also proposed were differential [149] and elliptic flows [81, 150]. Among all these outcomes, collective flow has been found to be sensitive towards nuclear equation of state, mean-field potential, nucleon-nucleon (NN) cross-sections as well as towards entrance channel properties such as the mass of the system [151-153], impact parameter of a reaction [99, 140, 150, 154-156] & incident energy of the projectile [157-160].

3.2 Directed transverse flow

Two nuclei that collide with each other at non zero impact parameter will produce a tiny participant zone of the compressed matter, while a head on collision at zero impact parameter will lead to higher compression and large pressure gradient. For non-zero impact parameter, there is an anisotropy in the pressure, resulting in **directed transverse flow** of the nuclear matter in the direction of the lowest pressure. The disappearance of the directed transverse sideward flow, termed the balance energy E_{bal}, was suggested as a powerful probe of the

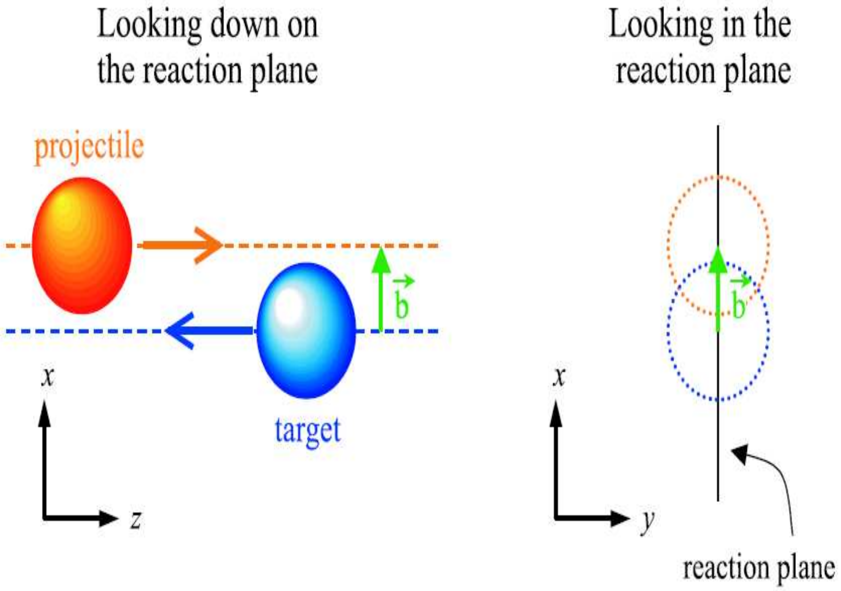

Figure 3.1: The geometric description of reaction plane and impact parameter [34].

equation of state [161, 162]. However, numerous model calculations have demonstrated that the balance energy, while sensitive to the nuclear compressibility K, was also sensitive to the in-medium cross section σ_{NN} [155, 163-166] as well as the momentum dependence of the nuclear mean field [68, 97, 99, 152, 167, 168]. As a result, at a certain incident energy, called the balance energy, the in-plane flow vanishes as a result of the cancellation between these two competing effects (attractive nuclear mean field potential at low energy and repulsive nucleon-nucleon scattering at high energy) [81, 145-151]. The composite dependence of the E_{bal} on the mean field and nucleon-nucleon cross-sections (σ_{NN}) can be sorted out by noting the sensitivity of E_{bal} on the system size, impact parameter, and isospin degree of freedom of the reaction [28, 141-147].

The reaction plane is defined as the plane containing the beam axis and a line joining the centre of two nuclei shown in Fig.3.1. The impact parameter vector ($\vec{b}$) joins the centre of target and projectile at their closest approach, lies within this plane. It is useful to distinguish between two side of the reaction plane as divided by beam axis, which will referred as the forward flow side ($Y > Y_{cm}$) and backward flow side ($Y < Y_{cm}$). These two sides contain the forward going and backward going sections of the particle flow in the center of mass frame of reference as shown in Fig.3.2 in which the projectile P moves from left to right along the z-axis, and collides with the target T moving in the opposite direction (the x-y plane is perpendicular to the beam direction). The central column is the projection of

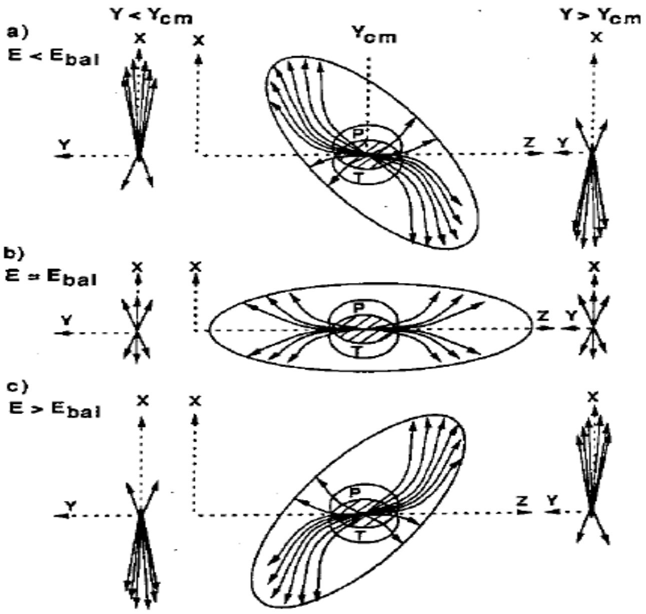

Figure 3.2: Diagramatic representation of the forward and backward flow side of the reaction plane for three incident energies:(a) $E < E_{bal}$ (b) $E = E_{bal}$ (c) $E > E_{bal}$ [144]. The setup shown in this figure is taken from front view.

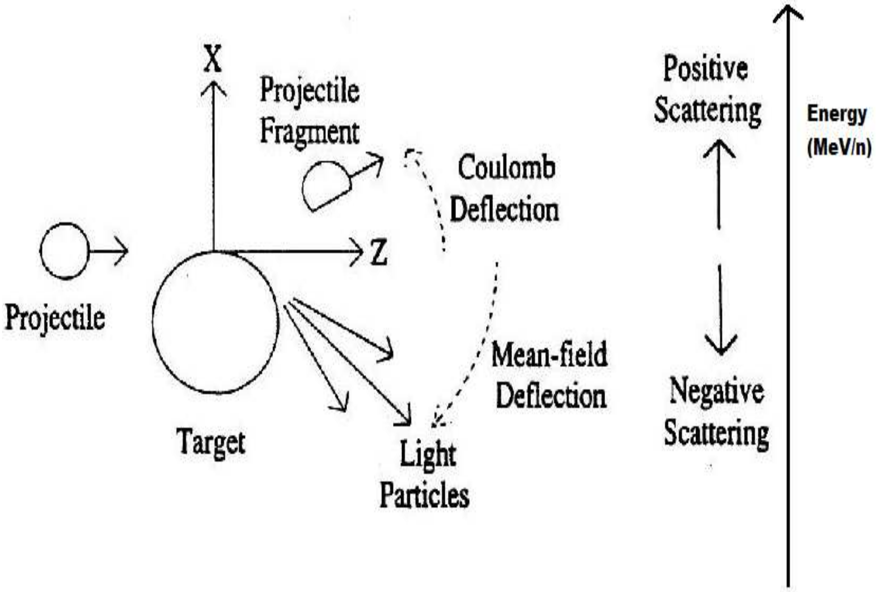

Figure 3.3: Schematic description of the proposed deflection in the peripheral events [169].

linear momenta onto the reaction plane (the x-z plane), and these linear momenta projected onto the x-y plane are the transverse momenta. The left (right) column shows the transverse momenta for particles with c.m. rapidity ($Y < Y_{cm}$ and $Y > Y_{cm}$). Focusing attention on the case for particles moving forward in the c.m. frame ($Y > Y_{cm}$) in the right column, we observe: At low incident energies i.e. for $E < E_{bal}$, reaction dynamics are dominated by the attractive nuclear mean-field potential, the particles are mainly scattered away from the projectile side of reaction plane (to negative angles) or leads to negative directed flow, i.e., projectile like fragments orbit to target-side of the reaction plane. It is worth mentioning that at these energies the phenomenon of fusion, and cluster radioactivity are dominant [136, 170]. With increasing incident energy $E > E_{bal}$ repulsive nucleon-nucleon scattering becomes important, the particles are mainly scattered towards the projectile side of reaction plane (to positive angles) as shown in Fig.3.3. For $E = E_{bal}$ these two effect balance, the particles are symmetrically deflected in the reaction plane, and the directed transverse flow vanishes. The converse is true for particles moving backward in the c.m. frame ($Y < Y_{cm}$).

3.3 Earlier attempts on balance energy

Experimentally, balance energy is observed for different systems ranging from $^{12}C +^{12} C$ to $^{197}Au +^{197} Au$ [141-144, 163, 171-174]. The very accurate measurement of the E_{bal} in $^{197}Au +^{197} Au$ [174] has generated a renewed interest in the field. But, these studies have not shed any light on isospin effects. Later on, Pak *et al.* [144] demonstrated the isospin effect on the collective flow and balance energy at central and peripheral colliding geometries. These findings were limited only to the reaction $^{58}Fe+^{58}Fe$ and $^{58}Ni+^{58}Ni$ only. Theoretically, disappearance of the directed flow is studied using the Boltzmann-Uehling-Uehlenbeck (BUU) model [141-144, 149, 163, 171-173] and quantum molecular dynamics (QMD) model [5, 30, 81, 99, 139, 140, 142, 143, 163, 171-177]. Different theoretical attempts considered either a stiff or soft equation of state along with a variety of NN cross-sections. Recently, Puri *et al.* [145-147], conducted a very detailed analysis on the balance energy over the entire periodic table with masses between 24 and 394. This study shed light on various aspects of nuclear dynamics. Unfortunately, this study along with all the other studies reported in the literature was limited to central/semicentral collisions only [145-147]. Following this work, a detailed analysis on the the semi-central and peripheral collisions was performed by the Puri *et al.* in 2010 [175]. All of these studies indicated an enhanced cross-section of 40-55 mb with a stiff equation of state to verify the balance energy in intermediate energy heavy-ion collisions. All of these studies were independent of the isospin effects. The first study showing the isospin effects on the collective flow and balance energy was reported by Li *et al.* [29] using the isospin-dependent Boltzmann-Uehling-Uehlenbeck (IBUU) model, where the strong dependence of isospin effects was observed. In another contribution [81, 150], they suggested the demand of a reduced isospin-dependent cross-section ($\sigma = 0.88\sigma_{NN}$) to better explain the experimental data. Chen *et al.* [148] studied the effect of isospin degree of freedom on the balance energy using the isospin-dependent quantum molecular dynamics (IQMD) model, which was an improved version of the original QMD model [5, 79, 110, 135, 137, 138, 145-147]. The calculated results were found to differ from the data at all colliding geometries. Recently, Gautam *et al.* [176] also studied the isospin effect on the balance energy by using the IQMD model [30, 81, 177], and also compared their findings with the other theoretical and experimental findings.

From the above, it is clear that an enhanced constant cross-section is required in the QMD model to explain the experimental findings. However, it was also observed that the reduced isospin-dependent cross-section is valid for the soft as well as for soft momentum-dependent equation of state [81, 150, 176] within the IQMD or IBUU model.

For a given set of input parameters i.e. enhanced and reduced isospin-dependent cross-sections in the presence of a hard equation of state is not studied in the literature yet. Moreover, the effect of isospin-dependent cross-sections are studied on the limited systems experimentally as well as theoretically [29, 30, 81, 144, 148, 176, 177].

3.4 Plan for the present study

We plan to study the effect of enhanced as well as reduced value of isospin-dependent cross-section on the directed flow and ultimately on the balance energy. This will be supplemented by comparing our finding with the experimental data. For this study, we calculated the balance energy over wide range of system size from $^{12}C_6 +^{12} C_6$ to $^{197}Au_{79} +^{197} Au_{79}$. This study will provide an excellent opportunity to pin down the role of mass dependence, where only preliminary studies [142-147] have been performed yet. These preliminary studies suggest a power law dependence $\propto (A_{tot})^{\tau}$ of the balance energy on the composite mass of system.

3.5 Results and Discussion

We study the directed flow using a stiff equation of state along with enhanced and reduced value of isospin-dependent cross-section (σ= 0.7 to 1.3 σ_{NN}), by simulating various reactions. The time evolution of the reaction is a followed upto 200 fm/c. This is the time at which transverse in-plane flow saturates for lighter as well as for heavier systems. For this study, the reactions of $^{12}C_6$ + $^{12}C_6$ ($\hat{b}$ = 0.4, L=0.5L) where L=8.66 fm^2, $^{20}Ne_{10}$ + $^{27}Al_{11}$ ($\hat{b}$ = 0.4, L=0.5L), $^{40}Ar_{18}$ + $^{45}Sc_{21}$ ($\hat{b}$ = 0.4, L=0.5L), $^{40}Ar_{18}$ + $^{51}V_{23}$ ($\hat{b}$ = 0.3, L=0.5L), $^{86}Kr_{36}$ + $^{93}Nb_{41}$ ($\hat{b}$ = 0.4, L=0.6L), $^{64}Zn_{30}$ + $^{58}Ni_{28}$ (b=2 fm, L=0.6L), $^{93}Nb_{41}$ + $^{93}Nb_{41}$ ($\hat{b}$ = 0.3, L=0.7L), $^{129}Xe_{54}$ + $^{118}Sn_{50}$ (b=0-3 fm, L=0.7L), $^{139}La_{57}$ + $^{139}La_{57}$ ($\hat{b}$ = 0.3, L=0.8L), and $^{197}Au_{79}$ + $^{197}Au_{79}$ (b=2.5 fm, L=L) are simulated. The choice of impact parameter is guided by the experimentally extracted information [141-144, 163, 171-174]. The above reactions were simulated between 45 and 200 MeV/nucleon using the hard equation of state along with different values of isospin-dependent cross-section. We attempted to fit the reduced isospin-dependent cross-section in the presence of a stiff equation of state with the experimental findings, as was performed in the literature with the soft equation of state with and without momentum-dependent interactions.

The mass dependence is studied at time t= 200 fm/c. This is the time at which transverse in-plane flow saturates for lighter as well as for heavier systems. As the balance energy is due to contribution of mean field and nucleon-nucleon collision. To observe the effect of isospin dependent cross-sections on the balance energy, one must check the effect of cross-section on the number of collision and the number of particles for the particular rapidity distribution, if the N_{coll} and rapidity distribution is affected by the isospin dependent cross-section, then directed flow or balance energy (E_{bal}) or energy of vanishing flow (EVF) is supposed to be affected surely by the isospin dependent cross-section. In Fig.3.4, we display the mass dependence of the allowed nucleon-nucleon collision. The number of collisions shows a linear enhancement with the composite mass of the system and with increase in the incident energy from 60 to 200 MeV/nucleon. Moreover, the cross-section affects the number of collisions to a great extent i.e. with increase in the cross-section, number of collisions are found to increase. This is indicating that cross-sections will surely affect the balance energy. There are two methods suggested in the literature, used to find the balance energy. In the first case, the balance energy is extracted from the $\langle P_x/A \rangle$ plots, where $\langle P_x/A \rangle$ is plotted as a

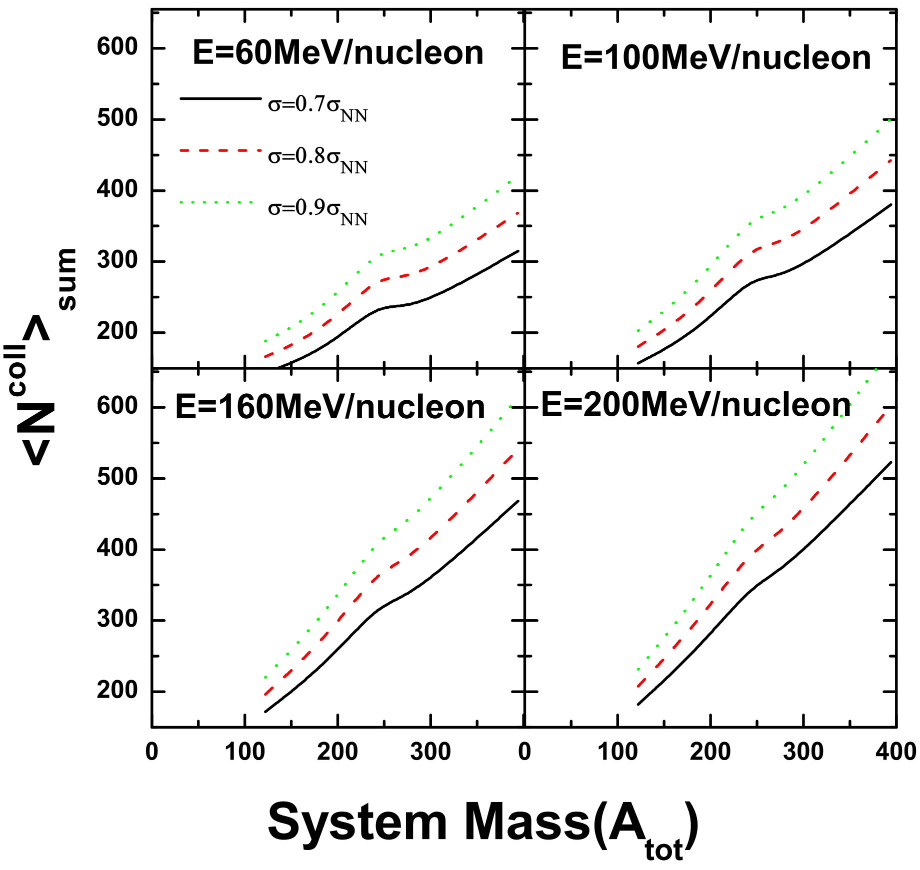

Figure 3.4: System mass dependence of number of collision at different isospin-dependent cross-sections. The different panels are at different incident energies.

function of rapidity distribution Y_{cm}/Y_{beam} [144], which is given as.

$$Y(i) = \frac{1}{2}\, ln \frac{E(i) + P_z(i)}{E(i) - P_z(i)}, \tag{3.1}$$

where E(i) and $P_z(i)$ are, respectively, the total energy and longitudinal momentum of the i^{th} particle [145-147]. Naturally, the energy at which this flow passes through zero is called the balance energy. The second method is to study the incident energy dependence of the directed transverse in-plane flow $\langle P_x^{dir} \rangle$, which is defined as [145-147]

$$\langle P_x^{dir} \rangle = \frac{1}{A} \sum_{i}^{A} sign\{Y(i)\} P_x(i), \tag{3.2}$$

where Y(i) is the rapidity distribution as discussed previously and $P_x(i)$ is the transverse momentum of the i^{th} particle in the x-direction. The effect of isospin dependent cross-section on the flow or alternatively on balance energy is studied by using $\langle P_x/A \rangle$ and $\langle P_x^{dir} \rangle$ parameters. This $\langle P_x^{dir} \rangle$ is defined over the entire rapidity region and therefore expected to present an easier way of measuring the in-plane flow rather than the complicated $\langle P_x/A \rangle$. In the present study, we tried to study the effect of isospin-dependent cross-sections on the flow or alternatively on the balance energy by using both of the parameters; then the detailed study was extended with the latter one.

3.5.1 The averaged $\langle P_x/A \rangle$ and $(dN/dY)_{norm}$ as a function of Y_{cm}/Y_{beam}

Figs.3.5 and 3.6 shows the distribution of transverse momentum versus the rapidity Y_{cm}/Y_{beam} at different energies, for different cross-sections and for different systems respectively. At very low incident energy, the negative slopes corresponding to negative scattering angles are visible whereas at higher incident energies the opposite sign slopes positive scattering angles are found. The former corresponds to negative flow parameter while the latter corresponds to the positive flow parameter. In Fig.3.5 we display the change in the transverse momentum $\langle P_x/A \rangle$ as a function of the rapidity distribution at different incident energies from 60 to 200 MeV/nucleon for $^{86}Kr_{36}$ + $^{93}Nb_{41}$ systems. The different lines in the figure show the variation for different cross-section values. From the figure, we see that slope becomes less negative or more positive with an increase in the incident energy. However, with a reduction in the cross-section (σ_{NN}), slope gets more negative or less positive, while, become more positive with the enhanced cross-section. This indicates that we see a change in the slope with the incident energy and reduced isospin-dependent cross-section. The balance energy is the energy at which slope of rapidity distribution $\langle P_x/A \rangle$ approaches to zero. The figure

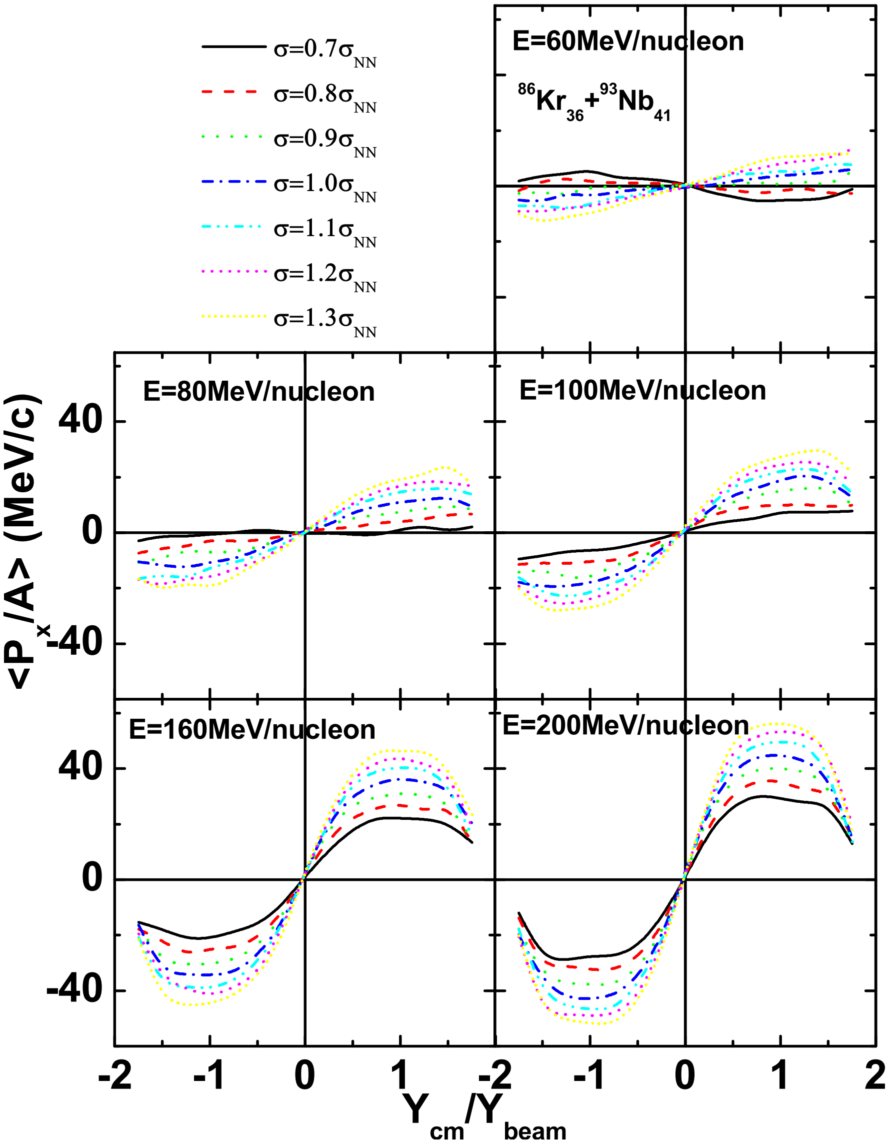

Figure 3.5: The averaged $\langle P_x/A \rangle$ as a function of the rapidity distribution. Here we display the result for the $^{86}Kr_{36}$ + $^{93}Nb_{41}$ system at different incident energies and different values of isospin-dependent cross-section.

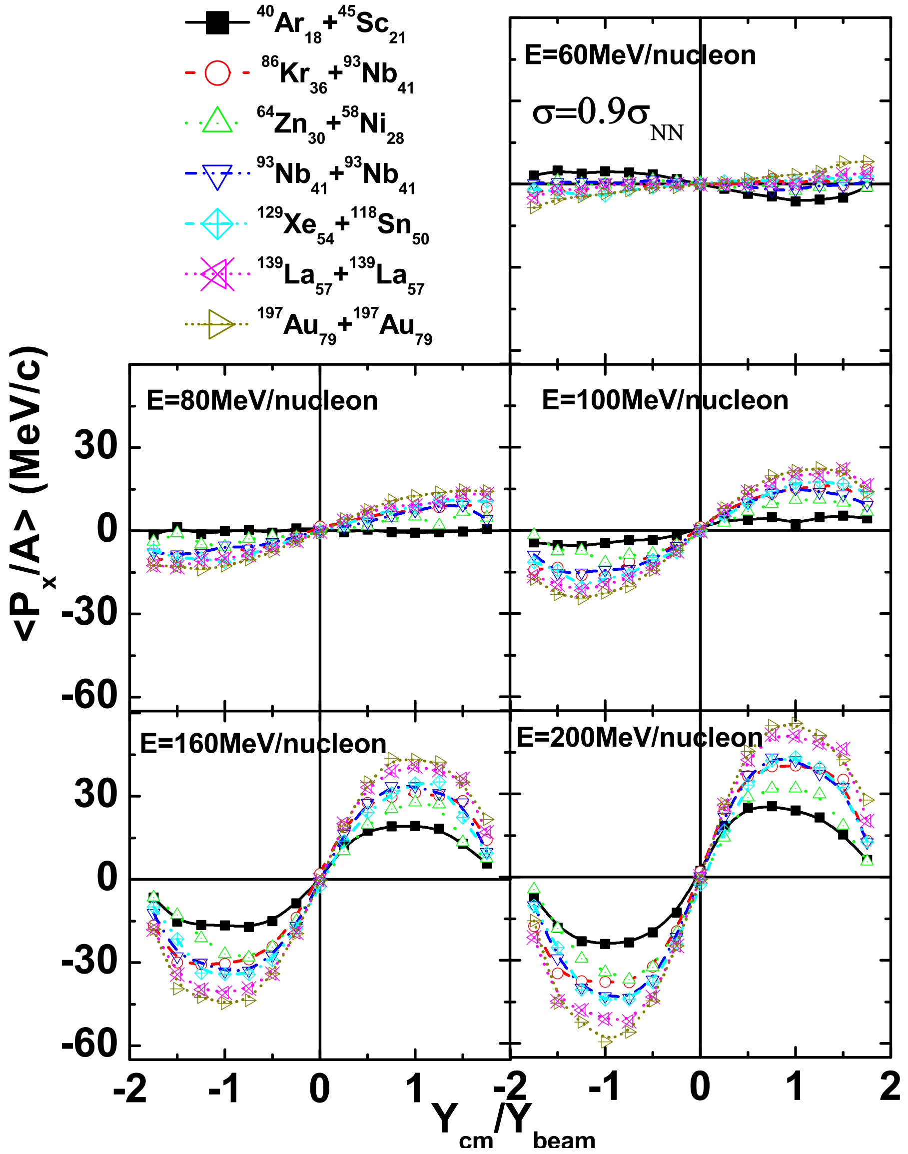

Figure 3.6: As in Fig.3.5, but for a different system and at the particular cross-section $\sigma = 0.9\sigma_{NN}$. Different panels are at different incident energies.

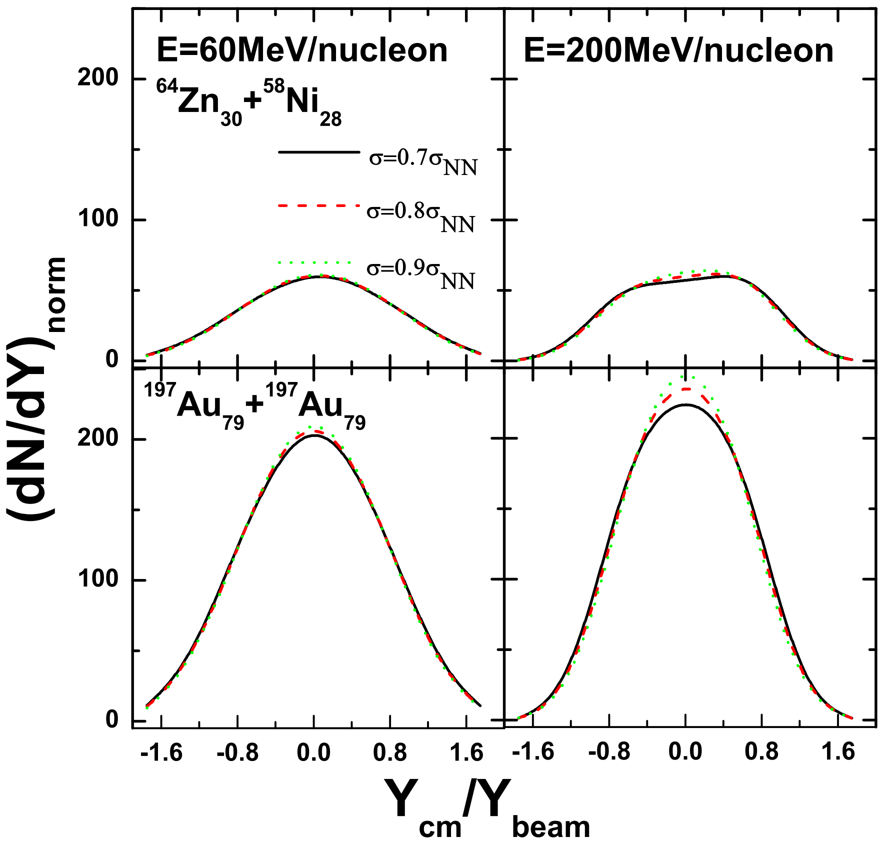

Figure 3.7: The normalized rapidity distribution $(dN/dY)_{norm}$ as a function of Y_{cm}/Y_{beam} for different values of cross-section. The upper panels are for $^{64}Zn_{30}$ + $^{58}Ni_{28}$, While, lower for $^{197}Au_{79}$ + $^{197}Au_{79}$ system.

indicates two values of the balance energy, that is, E=80 MeV/nucleon (at $\sigma = 0.7\sigma_{NN}$) and around E=60 MeV/nucleon (at $\sigma = 0.9\sigma_{NN}$) for the $^{86}Kr_{36} + {}^{93}Nb_{41}$ system. As the experimental balance energy for $^{86}Kr_{36} + {}^{93}Nb_{41}$ is in the range of 55-60 MeV/nucleon, so one expects to follow the whole of the dynamics at $\sigma = 0.9\sigma_{NN}$.

Further, the detailed analysis of the rapidity distribution of transverse momentum $\langle P_x/A\rangle$ for different systems at different energies with $\sigma = 0.9\sigma_{NN}$ is displayed in Fig.3.6. The slope becomes more positive or less negative with the increase in the composite mass of the system, indicating that lighter systems remain in the environment of mean field compared to NN collisions at any given incident energy. The contribution of the mean field and the collisions is discussed in detail in Ref. [145-147]. One also notices that a higher incident energy is needed in lighter cases to balance the attractive and repulsive forces. This energy is supposed to decrease with an increase in the system mass. Similar findings are also published by Puri *et al.* [145-147]. Note that their study did not take isospin effects into consideration.

To elaborate more, in Fig.3.7, the rapidity distribution is studied for different cross-sections. In this figure, we study the degree of equilibrium reached for Zn+Ni and Au+Au reactions at E=60 and 200 MeV/nucleon. For a full equilibrium, one should get, a Gaussian shaped peak at midrapidity. The degree of equilibrium depends on system mass as well as on the number of collisions (any individual nucleon suffer) which is found to increase with the incident energy. From the figure, it is clear that effect of cross-section is observed at higher incident energies, where NN collision are more active. Moreover, the heavier system (Au+Au) is more thermalized as compared to lighter ones (Zn+Ni).

3.5.2 Time evolution of $\langle P_x^{dir}\rangle$ for different systems at E = 60 and E = 200 MeV/nucleon

In the Figs.3.8 and 3.9, we show the time evolution of second parameter $\langle P_x^{dir}\rangle$ below (60 MeV/nucleon) and above (200 MeV/nucleon) the experimental balance energy, respectively. The displayed reactions in this figure are $^{12}C_6 +^{12} C_6$, $^{20}Ne_{10} +^{27} Al_{11}$, $^{40}Ar_{18} +^{45} Sc_{21}$, $^{40}Ar_{18} +^{51} V_{23}$, $^{86}Kr_{36} +^{93} Nb_{41}$. Note that the different curves in each part of the figure are for different values of isospin-dependent cross-section. We see that the flow first becomes negative and finally it saturates either at negative or positive values depending on the bombarding energy. The negative flow at the start of reaction signifies the attractive nuclear interactions at the start. At low incident energies, due to the lack of available phase space, we have few nucleon-nucleon collisions and as a result, the nuclear interactions are still at-

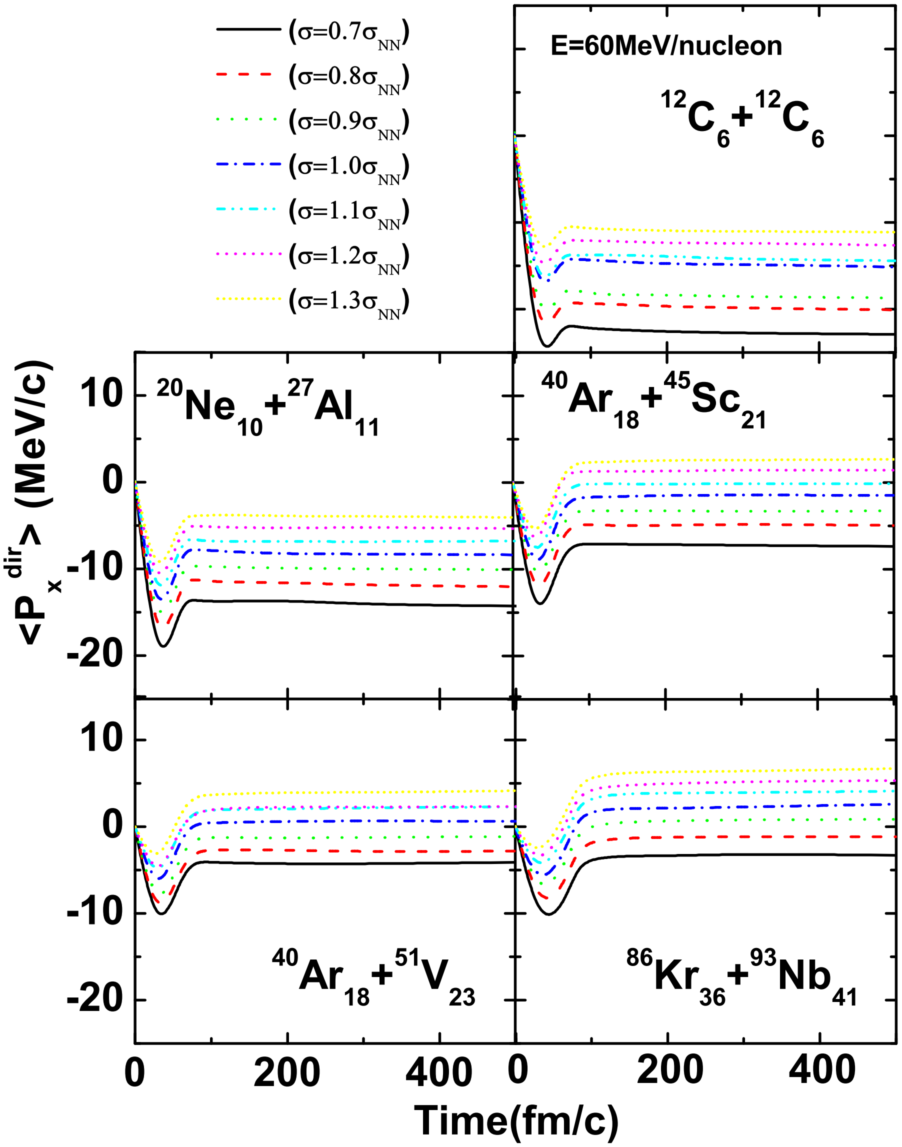

Figure 3.8: Time evolution of $\langle P_x^{dir} \rangle$ for different systems at E=60 MeV/nucleon. The different lines in the figure represent the directed flow at different values of cross-section.

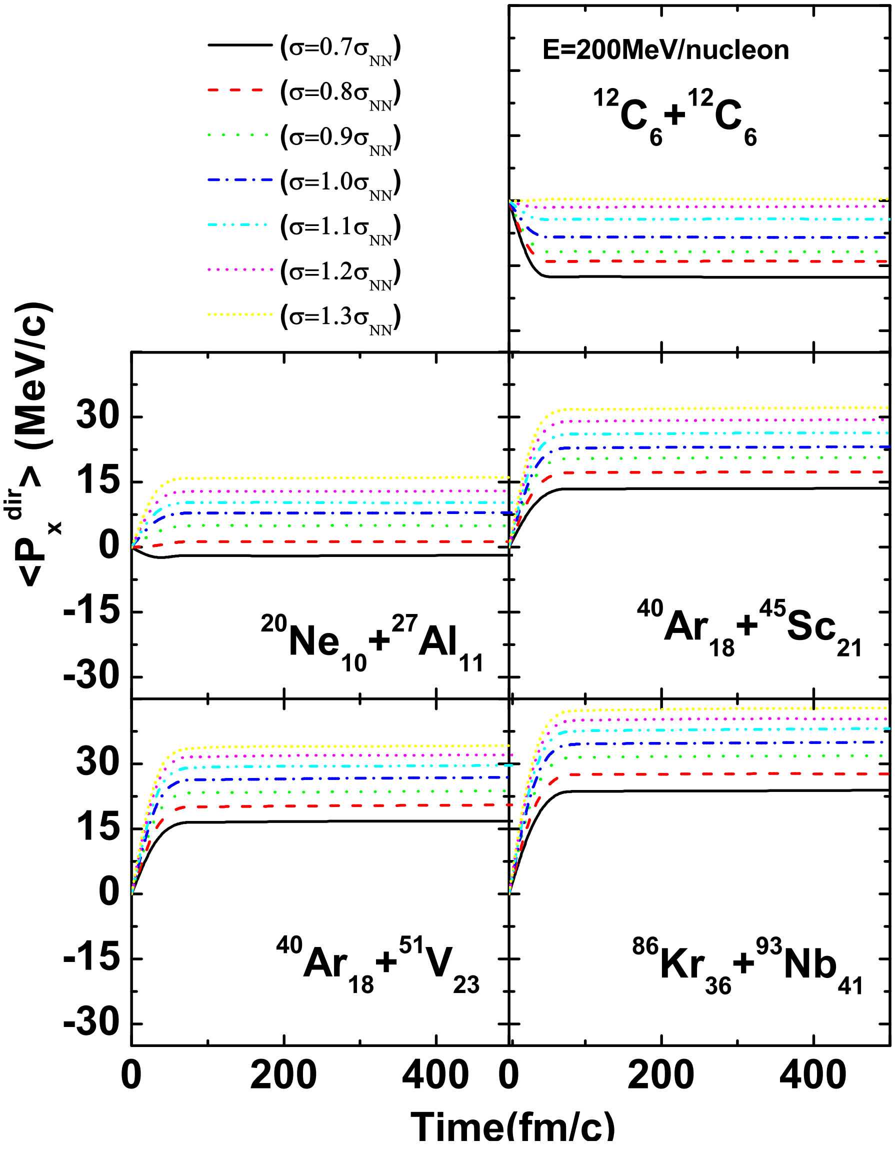

Figure 3.9: Time evolution of $\langle P_x^{dir} \rangle$ for different systems at E=200 MeV/nucleon. The different lines in the figure represent the directed flow at different values of cross-section.

tractive. At higher incident energies, however, one has frequent nucleon-nucleon collisions and therefore, nuclear flow is repulsive at the end of the simulations. One also notices that a larger cross section have more allowed collisions and thus, the flow becomes positive at lower incident energies compared to that of smaller cross section. The results in the figure are displayed for five different systems and at reduced as well as enhanced isospin-dependent cross-sections. The figures indicate the similar scenario with $\langle P_x^{dir} \rangle$, as is depicted with $\langle P_x/A \rangle$. Below the balance energy in Fig.3.8, the directed in-plane flow is negative during the initial phase of the reaction for all systems under consideration. This becomes positive at sufficient high incident energy, say E=200 MeV/nucleon Fig.3.9. These results shows that the interactions among nucleons are attractive during the initial phase of the reaction, which turns out to be repulsive with the increase in the incident energy. These interactions remain either attractive or repulsive throughout the time evolution, which depends on the incident energy, value of isospin-dependent cross-section, as well as the composite mass of the system. It is clear from the figure that directed flow becomes more positive or less negative with the incident energy, isospin-dependent cross-sections, as well as with the size of system. There is a sharp transition for each system from negative to positive directed flow at a particular cross-section. This particular transition is not possible for the $^{12}C_6$ + $^{12}C_6$ system as it indicates the requirement of other variable-like momentum-dependent interactions as well as the enhancement in a cross-section of more than 30 %.

If one compares Fig.3.5 through Fig.3.9, the same physics of the balance energy elaborates with $\langle P_x/A \rangle$ as well as with $\langle P_x^{dir} \rangle$. Out of these, as discussed earlier, $\langle P_x^{dir} \rangle$ is the simple and more useful quantity, because it is summed over the entire rapidity distribution, that is why, $\langle P_x^{dir} \rangle$ is elaborated in detail for further study.

3.5.3 Energy dependence of directed flow for different system

Let us understand the concept of second parameter $\langle P_x^{dir} \rangle$. One can use this to find the balance energy by plotting the energy dependence of directed flow. So, to study the influence of reduced as well as enhanced cross-section on directed flow $\langle P_x^{dir} \rangle$ or alternatively on the balance energy, in Figs.3.10 and 3.11, incident energy dependence of the directed flow is displayed for different systems. The different lines in the figures represent the variation with different values of cross-section. The studies with enhanced and reduced cross-section are also available in the literature [81, 145-147, 150, 176]. The experimental data are represented

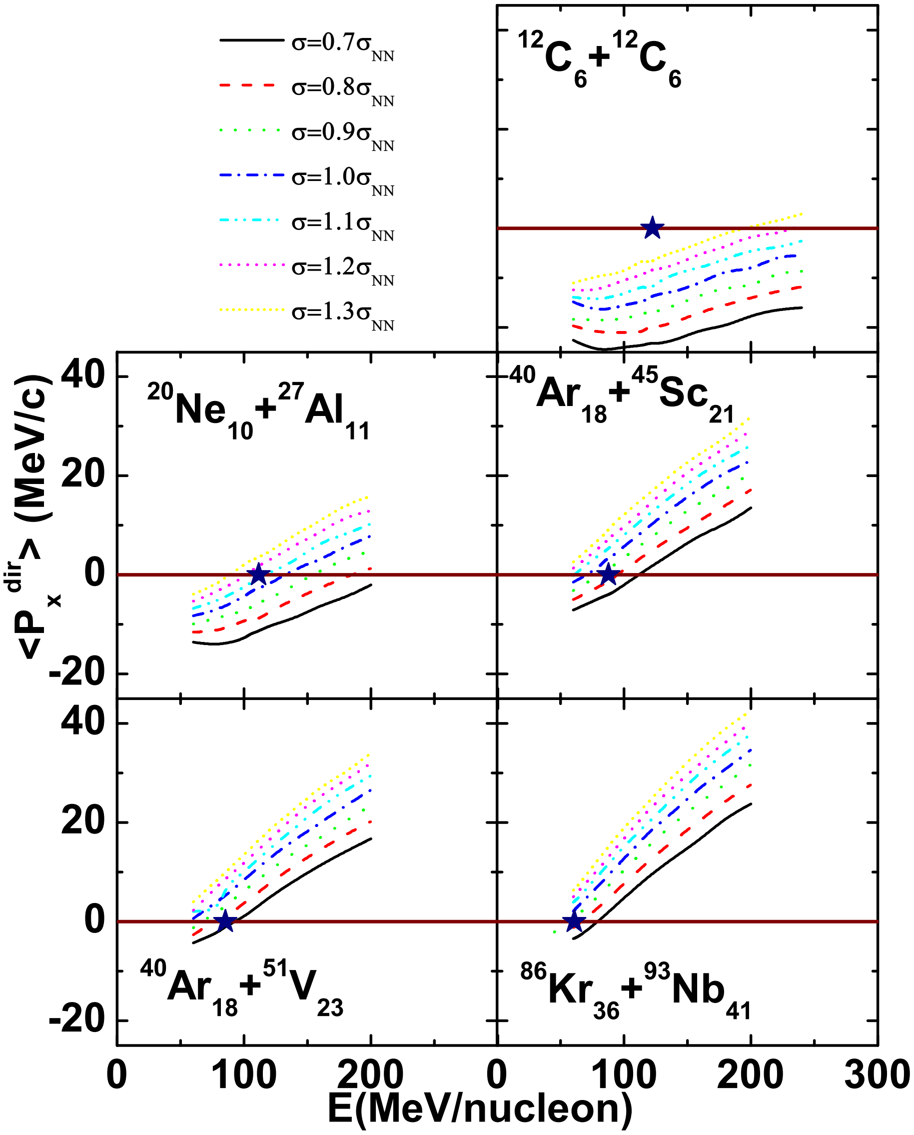

Figure 3.10: Energy dependence of the directed nuclear flow $\langle P_x^{dir} \rangle$ for different systems. The lines have the same meaning as that in Figs. 3.8 and 3.9.

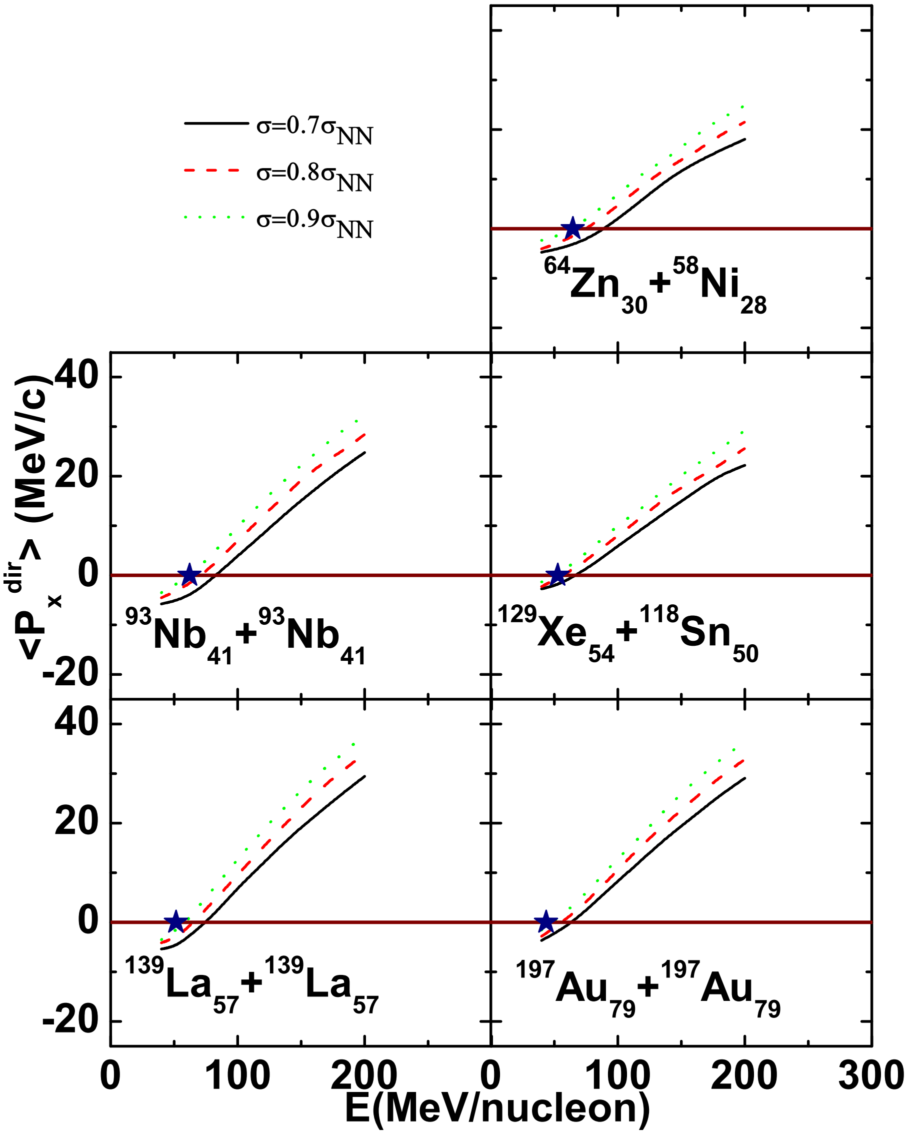

Figure 3.11: Same as in Fig.3.10, but for different systems.

by stars. The directed flow changes from a negative to positive value with an increase in the incident energy. This is the general trend and is explained many times in the literature by taking the concept of mean field and NN cross-section. However, the role of different values of cross-section is consistent for the present mass range. By finding the evidence of reduced cross-sections from Fig.3.10, the results are displayed between the (0.7-0.9 σ_{NN}) values in Fig.3.11. The enhanced cross-section (1.3 σ_{NN}) gives a more positive value of flow followed by the reduced cross-section (0.7 σ_{NN}). In other words, with the increase in the cross-section value from ($0.7\sigma_{NN}$-$1.3\sigma_{NN}$), the directed flow becomes more positive or less negative. The reason for this is that with the increase in the cross-section value, the probability of collision increases, which further results in an increase in the NN collisions and hence more positive value of the directed flow. This results in the decrease of the balance energy.

The balance energy is also found to decrease with an increase in the composite mass of the system. This is due to the dominance of Coulomb repulsion with an increase in the composite mass of the system. Except for some lighter systems, the cross-section $\sigma = 0.9\sigma_{NN}$ is found to explain the experimental balance energy nicely. A similar parametrization was also performed by Sood *et al.* [145-147] within the QMD model. They also found that the enhanced cross-section ($\sigma_{NN} = 40mb$) can best explain the data. On the contrary, the calculation in the IQMD model demands a reduced value of the cross-section. The difference is due to the additional effect of isospin-dependent cross-section in the IQMD model [30, 81, 177], that were absent in the QMD model. As in the QMD model, the strength of the nn, pp, and np cross-section is taken to be equal, while in the IQMD, $\sigma_{np} = 3\sigma_{pp} \approx 3\sigma_{nn}$ [30, 81, 177].

Due to the different strength of the np, pp, and nn cross-section in IQMD, additional repulsion is produced compared to the QMD model. This additional repulsion will force the directed flow to make an earlier transition from a negative to positive value and hence will lower the balance energy in the IQMD model as compared to QMD for the same cross-section value. This is the first ever parametrization of balance energy with a hard equation of state in the presence of reduced cross-section with the experimental available balance energy.

3.5.4 Balance energy as a function of system mass and N/Z

By taking Ref. [145-147] into account, which depicts, that for heavier colliding nuclei E_{bal} is independent of the cross-section one is choosing, we plotted in Fig.3.12 the

$\Delta E_{bal} = (E_{bal})_{0.7\sigma_{NN}} - (E_{bal})_{0.9\sigma_{NN}}$ with the composite mass of the system. Our findings also support the findings in Refs. [141-143, 149]. ΔE_{bal} is maximum for lighter systems and it goes on decreasing with system mass. It also indicates theoretically that balance energy is almost independent of the nucleon-nucleon cross-section for the heavier systems such as Au + Au, U + U, and so on.

In Fig.3.13, we display the energy of vanishing flow or balance energy (E_{bal}) as a function of the composite mass of a system that ranges from $^{40}Ar_{18}+^{45}Sc_{21}$ to $^{197}Au_{79}+^{197}Au_{79}$. In this figure, E_{bal} is shown for the experimental data (open stars), QMD + 40 mb (crossed triangle), and IQMD + 0.9 σ_{NN} (solid squares). All the curves are fitted with a power law of the form $C(A_{tot})^{\tau}$. The experimental data are fitted by $\tau = -0.33 \pm 0.06$. The balance energy is found to decrease with the composite mass of the system, which is a well known trend discussed many times in the literature [145-147]. The difference is in the τ values obtained by different theoretical models. The BUU model reports τ between $-0.28 \leq \tau^{th} \leq -0.32$. In another study [141-143], again with the BUU model, $\tau^{th} = -0.41 \pm 0.03$. The present calculation depicts the τ value (-0.29 ± 0.06), which is close to the experimental τ value (-0.33 ± 0.06) as compared to the QMD + 40 mb calculation having a τ value (-0.27 ± 0.17). In other words, the present IQMD model with a stiff equation of state along with $\sigma = 0.9\sigma_{NN}$ can explain the data much better than any other theoretical calculations. $\sigma = 0.9\sigma_{NN}$ explains the data for all nuclei, except for some lighter nuclei. The lighter nuclei, when checked out, call for an enhanced cross-section [81, 145-147] along with momentum-dependent interactions [83, 84, 178].

This result supports the notion that the mass dependence of the balance energy results from two competing factors:

1.)The competition between the attractive mean field, which can be associated with the surface area of the interacting nuclei and should scale as $C(A_{tot})^{\tau}$

2.)The repulsive nucleon-nucleon scattering potential, which scales as the number of nucleons present. Our calculations about the strength of the reduced NN cross-section is in agreement with an earlier calculation, where the disappearance of transverse in-plane flow [176] as well as elliptical flow is parametrized with the experimental data [81, 150].

We also tried to fit the balance energy in terms of other parameters such as the neutron-to-proton ratio of colliding nuclei. This attempt is shown in Fig.3.14, where balance energy is plotted as a function of N/Z. The E_{bal} is parametrized with a power law of the form $(N/Z)^{\tau}$. The τ value in the N/Z dependence is -2.39 ± 0.40, while in A_{tot} dependence in Fig.3.13 is

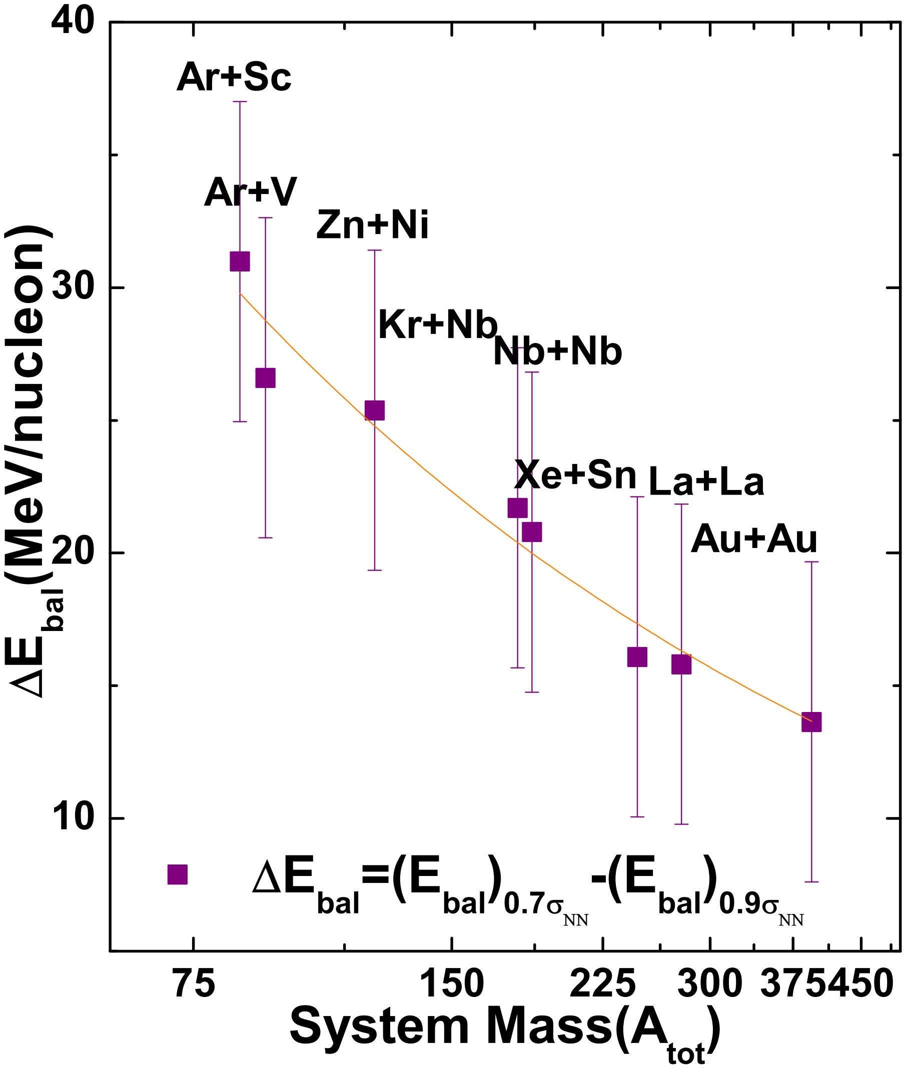

Figure 3.12: The shift in the balance energy due to cross-section as a function of combined mass of the system.

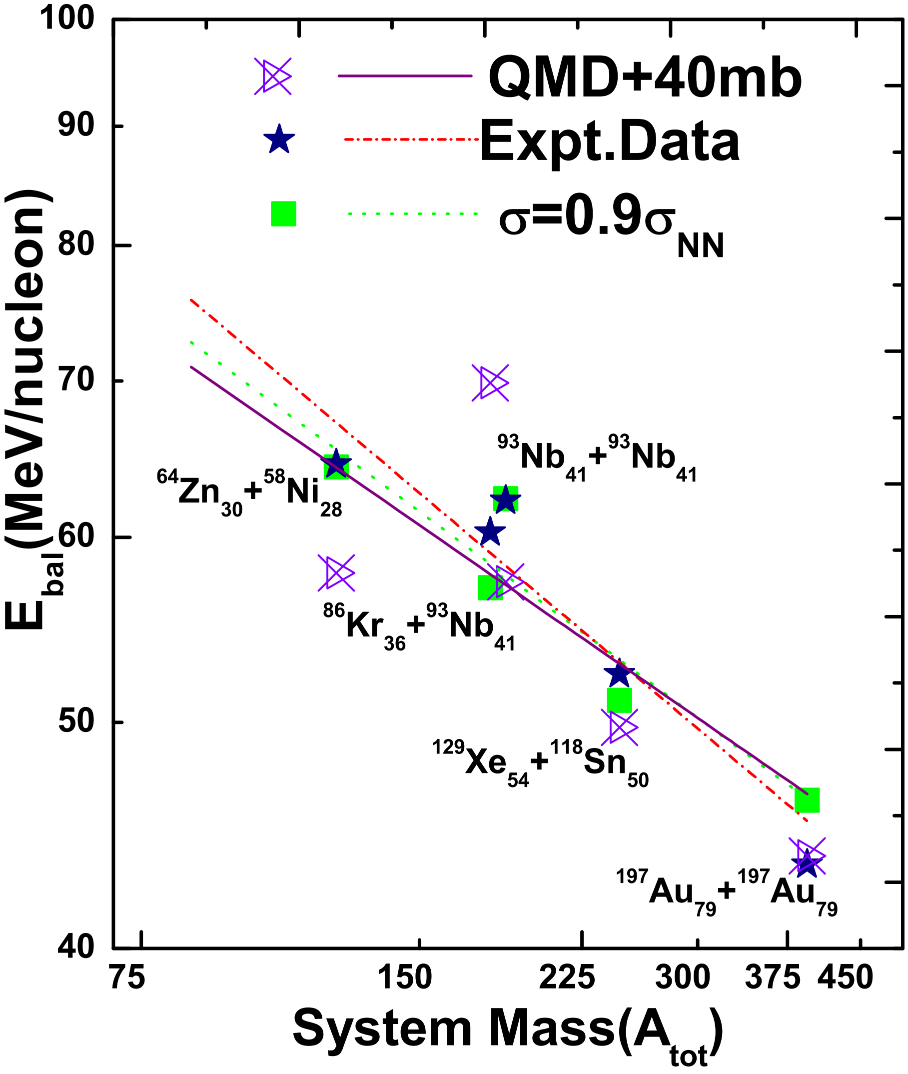

Figure 3.13: Balance energy as a function of the combined mass of the system. The experimental points are represented with stars, QMD + 40 mb with the crossed triangle, and the present with the solid square.

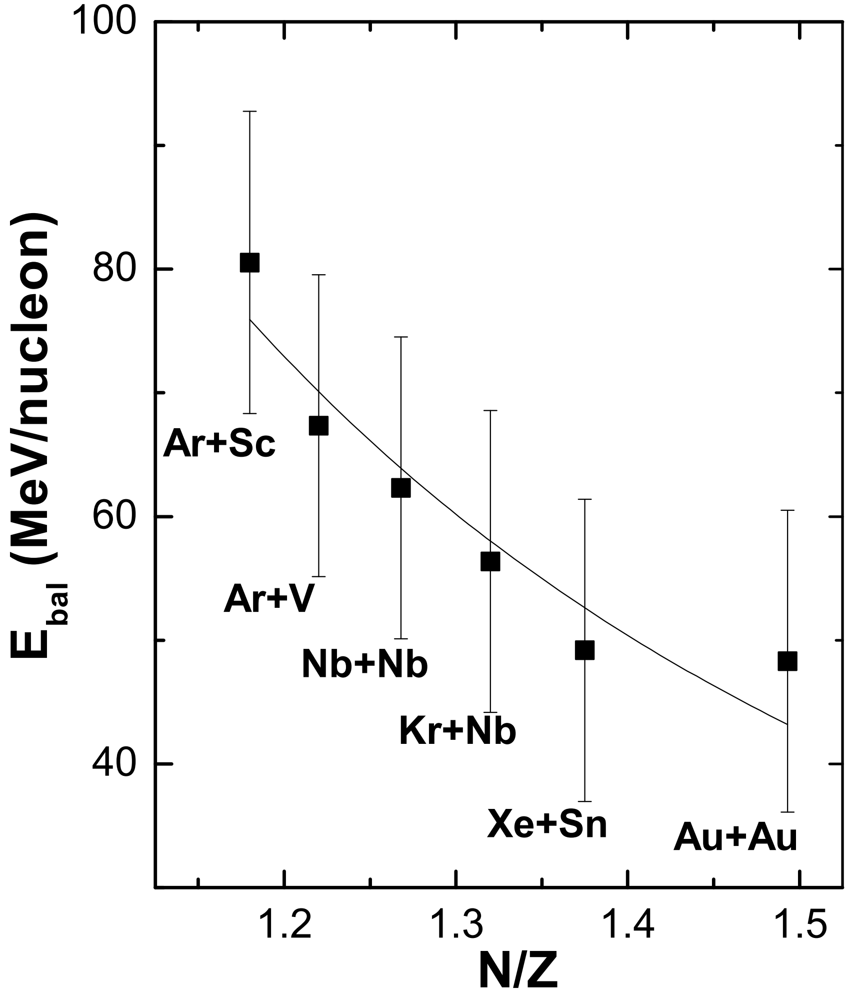

Figure 3.14: N/Z dependence of the balance energy at $\sigma = 0.9\sigma_{NN}$. The curve is parametrized with a power law.

-0.29 ± 0.06. The τ value in this case is larger compared to the N/Z dependence. The difference in the slopes may be due to a different charge-to-mass ratio in heavier colliding nuclei.

3.6 Summary

Using the IQMD model, we studied the effect of reduced as well as enhanced isospin-dependent cross-section on the directed flow and balance energy. A large number of reactions were studied having a mass range from 24 to 394, where experimental balance energy is available. The directed flow or in other words, balance energy is found to be sensitive towards the isospin-dependent cross-section. Our calculation with a stiff equation of state and reduced cross-section ($\sigma = 0.9\sigma_{NN}$) are in good agreement with the experimental findings, except for $^{12}C_6 +^{12} C_6$. The dependence of isospin-dependent cross-section weakens with the increase in the size of the system. The balance energy is parametrized with the N/Z ratio in terms of a power law, which is quite similar with the parametrization of the composite mass of the system, but the τ values are different in both cases.

One can try the balance energy prediction with an enhanced isospin-dependent cross-section in the presence of a momentum-dependent interaction for $^{12}C_6+^{12}C_6$, which was earlier studied by Sood *et al.* [145-147] using the QMD model in the presence of momentum-dependent interactions. This study is proven to be useful for nuclear community in order to parametrize the other observable in intermediate energy heavy-ion collision.

Chapter 4

Multifragmentation around the balance energy

4.1 Introduction

The intermediate energy heavy-ion collisions (from several tens to several hundreds MeV/ nucleon) typically yield several fragments like free nucleons (FNs) (A=1), light mass fragment (LMFs) ($2 \leq A \leq 4$), medium mass fragment (MMFs) ($5 \leq A \leq 11$), intermediate mass fragment (IMFs) ($5 \leq A \leq A_{tot}/6$). At relatively low incident energies, dissipative binary reactions may create IMFs at midrapidity, while higher-energy central collisions create expanding systems that produce clusters copiously; and peripheral collisions produce excited fragments. The IMFs typically carry a major part ($\approx 50\%$) of the nucleons involved in reaction. At excitation energy $\epsilon \approx 1$ MeV/nucleon, successive emission of particles by evaporation of the compound nucleus or its fission are the basic de-excitation mechanisms. At excitation energy comparable to the binding energy $\epsilon \approx 8$ MeV/nucleon, a very existence of a long-lived compound nucleus is unlikely which leads to the scenario of an explosion-like process involving the whole nucleus. This will lead to multiple emission of nuclear fragments of different masses. This is what we called **multifragmentation** where multi is more than two. The multiplicity of these fragments in an event depends upon the violence of the collision, i.e., the centrality and incident beam energy. For non-central events, a target and projectile remnant are created, and these spectator source may also de-excite via fragment emission.

In the previous chapter, we have studied energy dependence of the directed flow for various systems. Balance energy extracted from these is then plotted as a function of the system mass and compared with the experimental data. In this chapter, we study the multifragmentation around the balance energy (i.e. above, below and at EVF) [179] and also try to attempt a systematic study of the mass dependence in multifragmentation around the bal-

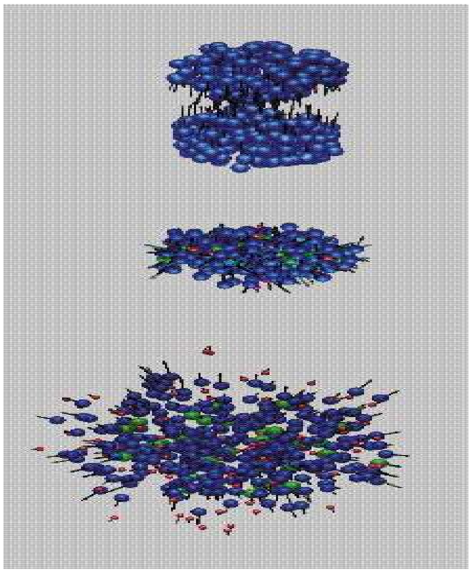

Figure 4.1: Pictorial view of multifragmentation of two colliding nuclei

ance energy using isospin-dependent reduced cross-section. The system-size effects depend on the reaction inputs as well as on the colliding geometries. The multiplicity of any kind of fragment can be parametrized in terms of a power law C$(A_{tot})^{\tau}$, where A_{tot} is the total mass of the composite system. This is true for a wide range of the impact parameter and incident energy considered here.

4.2 Description of multifragmentation

The breaking of colliding nuclei into several complex pieces as shown in Fig.4.1. (consisting of light, intermediate as well as heavy masses) has been of core importance both in experimental and theoretical studies. The multifragmentation offers an unique opportunity to explore the properties of a quantum many-body system very far from the equilibrium and to discover the universal law of fragmentation, which is theoretically meaningful for investigating the phase transition and critical phenomenon of a finite system. A great deal of the experimental and theoretical work has been devoted to the studies of the mechanism for IMF emission. The lower charge limit of IMF is set to 5. The upper limit should exclude the fission like fragments; if the nucleus broke up into several pieces, we could expect some of them to be IMFs.

In the earlier understanding, multifragmentation was considered to be **statistical process**

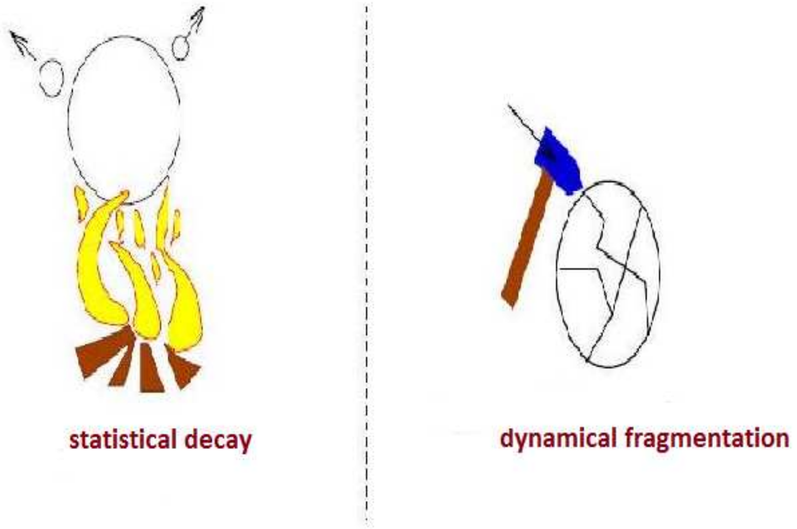

Figure 4.2: Illustration of statistical and dynamical decay in multifragmentation

in which the nucleon-nucleon correlations are neglected and one cannot study the formation and origin of fragments. This means that during the reaction at least a subsystem comes to statistical equilibrium and maintains this equilibrium during expansion until it has reached the freeze-out volume. Then it disintegrates instantaneously into FNs, LMFs and IMFs. It is assumed that at freeze-out the system is in statistical equilibrium and the disintegration pattern is determined by phase space. Presently, one has dynamical models and multifragmentation is considered as **dynamical process** in which one can simulates the reaction dynamics starting from two well defined nuclei to the end of the reaction where one has practically cold and scattered nuclear matter in the form of nucleons, light and heavy mass fragments [180] and hence are capable of investigating the evolution of fragmentation, the nucleon-nucleon correlation, the liquid-gas phase transition, etc. [74, 92, 168, 181, 182]. Both statistical decay as well as dynamical fragmentation are shown in Fig.4.2. These models are originally developed to describe proton spectra, particle production and the influence of the nuclear equation of state on observable like flow, they have been later developed to explain also multifragmentation, i.e., multiple emission of nuclear fragments of different masses. It is now quite clear that the multiplicity of these fragments depends crucially on the bombarding energy, masses of colliding nuclei as well as on the impact parameter of the reaction. The experimental studies can be divided into symmetric and asymmetric reactions. Former category leads to higher compression whereas latter lacks the compression and therefore, large part of excitation energy converts into thermal energy [5, 112, 183-185]. As stated in previous chapters, recently Chandigarh group [145] also study the multifragmentation & associated phenomena at the energy of vanishing flow. They find that a power law dependence exist over all the energy of vanishing flow. It still remains to be seen whether the fragmenting matter at the energy of vanishing flow is sensitive towards the isospin-symmetry energies and how structure of fragments at EVF differs from the one obtained at different incident energies. Till now, no such study exists in the literature so far that sheds light on the fragment's structure around EVF using the isospin dependent quantum molecular dynamics (IQMD) model. It is worth reminding that the energy of vanishing flow is much higher in lighter colliding nuclei compared to the heavier one where matter counterbalances attractive and repulsive forces at low incident energies. It is also evident from the literature that the form and strength of the symmetry energy depends on the incident energy and corresponding density. Therefore, one would like to investigate how multiplicity of various fragments behaves at the energy of vanishing flow and whether the trend is similar to that obtained at low or higher incident energies. Further, how symmetry energy affects the dynamics around the energy of vanishing flow.

4.3 Results and Discussion

The present analysis is made using the reactions of $^{197}Au_{79}$ + $^{197}Au_{79}$ (b=2.5 fm), $^{139}La_{57}$ + $^{139}La_{57}$ ($\hat{b} = 0.3$), $^{93}Nb_{41}$ + $^{93}Nb_{41}$ ($\hat{b} = 0.3$), $^{86}Kr_{36}$ + $^{93}Nb_{41}$ ($\hat{b} = 0.4$), $^{64}Zn_{30}$ + $^{58}Ni_{28}$ (b=2 fm), $^{40}Ar_{18}$ + $^{45}Sc_{21}$ ($\hat{b} = 0.4$) where $\hat{b}$ is the scaled impact parameter, defined as $\hat{b} = \frac{b}{b_{max}}$, (b is particular impact parameter in Fermi (fm) and $b_{max} = 1.12(A_T^{1/3} + A_P^{1/3})$), A_T and A_P are the masses of target and projectile respectively. The corresponding energy of vanishing flow (EVF) as predicted in **chapter 3** for $^{197}Au +^{197} Au$, $^{139}La +^{139} La$, $^{93}Nb +^{93} Nb$, $^{86}Kr +^{93} Nb$, $^{64}Zn +^{58} Ni$, $^{40}Ar +^{45} Sc$ were reported to be 48, 58, 62, 56, 64, 80 MeV/nucleon respectively [81]. The calculations have been carried out with symmetry energy corresponding to normal nuclear matter density which is $E_{sym} = 32 MeV$ [186]. It is worth mentioning that these EVF is now found to be in closer agreement with experimental energy of vanishing flow. Each of above reaction was simulated at their corresponding energy of vanishing flow for 1000-3000 events till reaction saturates. It has been observed by many authors that the reaction time in lighter colliding nuclei is shorter compared to heavy nuclei. For comparison, calculations were also made below and above the energy of vanishing flow. In the present calculations, mass dependent Gaussian width was employed.

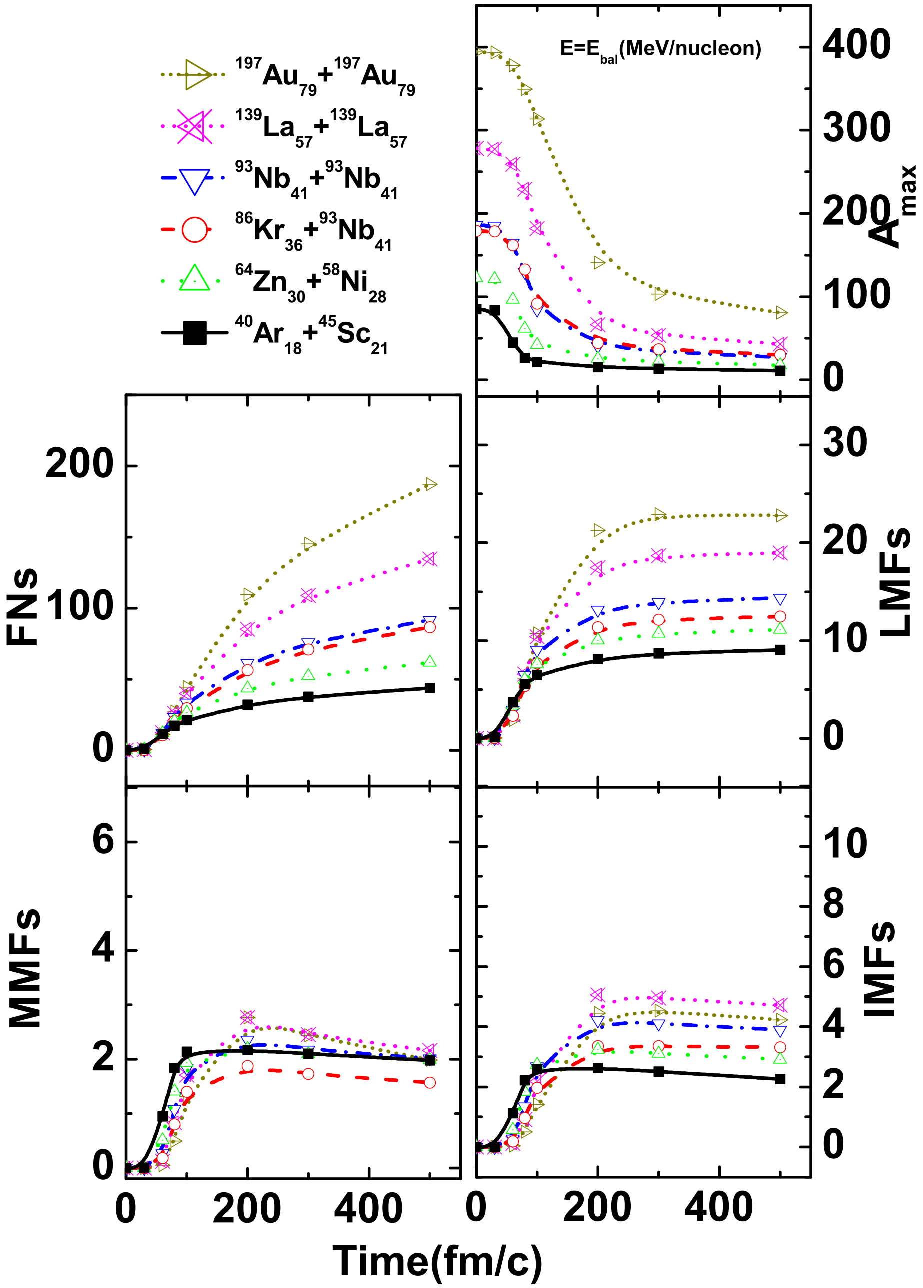

Figure 4.3: Time evolution of largest fragment A_{max}, FNs, LMFs, MMFs, IMFs for the collision of ^{197}Au+^{197}Au, ^{139}La+^{139}La, ^{93}Nb+^{93}Nb, ^{86}Kr+^{93}Nb, ^{64}Zn+^{58}Ni, ^{40}Ar+^{45}Sc at their corresponding theoretical balance energies of 48, 58, 62, 56, 64 and 80 MeV/nucleon.

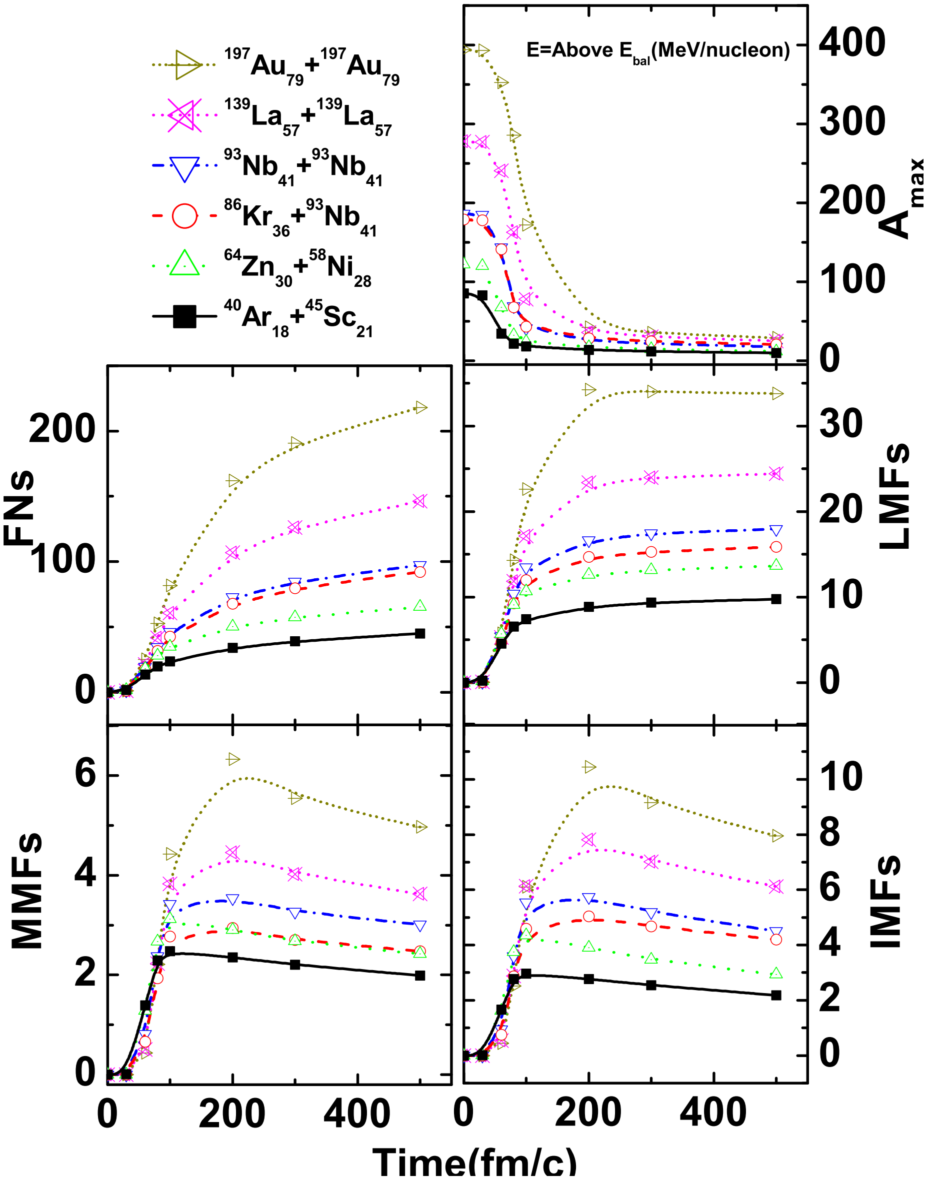

Figure 4.4: Same as in Fig.4.3, but for the reactions of $^{197}Au +^{197} Au$, $^{139}La +^{139} La$, $^{93}Nb+^{93}Nb$, $^{86}Kr+^{93}Nb$, $^{64}Zn+^{58}Ni$, $^{40}Ar+^{45}Sc$ at incident energy of 100 MeV/nucleon.

After a couple of hundreds fm/c, reaction is assumed to be over. The clusterization at first instance is made using the minimum spanning tree (MST) method, that binds two nucleons in a cluster if their centroids are separated by a distance less than 4 fm [187].

4.3.1 Time evolution of different fragments around the energy of vanishing flow

Now it would be of interest to know, how multiplicities of different fragments change with time around the energy of vanishing flow. In Fig.4.3, we display the time evolution of different fragments for the above mentioned reactions at their corresponding energy of vanishing flow. The displayed windows are the heaviest fragment A_{max}, FNs, LMFs, MMFs as well as IMFs. The MST method gives one big excited compound cluster at the time of maximum density that decays later into FNs and fragments. As a result, FNs, LMFs, MMFs, IMFs continue to rise till interaction among nucleons ceases. One also see that lighter colliding nuclei saturate much faster compared to heavier nuclei. In addition, since balance energy in heavier nuclei is much smaller than that of lighter nuclei, it takes longer time for heavier nuclei to saturate. At the start of the reaction, all nucleons constitute spectator matter. Since $^{40}Ar +^{45} Sc$ reaction happens at relatively higher energy of vanishing flow. The transition from the spectator to participant matter is swift and sudden. In contrast, due to low bombarding energy, such transition is slow and gradual in heavier colliding nuclei. Since energy of vanishing flow represents counterbalancing between the attractive and repulsive forces, this also points toward the formation of lighter fragment that emerge from mid-rapidity region.

In Fig.4.4, we display the time evolution of different fragments at incident energy of 100 MeV/nucleon. Due to the increase in the incident energy, frequent nucleon-nucleon collisions enhance the emission of FNs, LMFs, IMFs and MMFs.

In Fig.4.5, we display the time evolution of different fragments below the corresponding energy of vanishing flow. The displayed windows are same as reported in Fig.4.3, with the decrease in the incident energy, excitation energy of the systems gets depleted severely and as a result, binary collisions are reduced drastically that suppresses the emission of FNs and LMFs. This point towards the dominance of attractive mean field below the balance energy. Reduced binary collisions and stronger attractive forces binds more and more nucleons in various fragments, therefore, reducing the production of medium and heavy mass fragments.

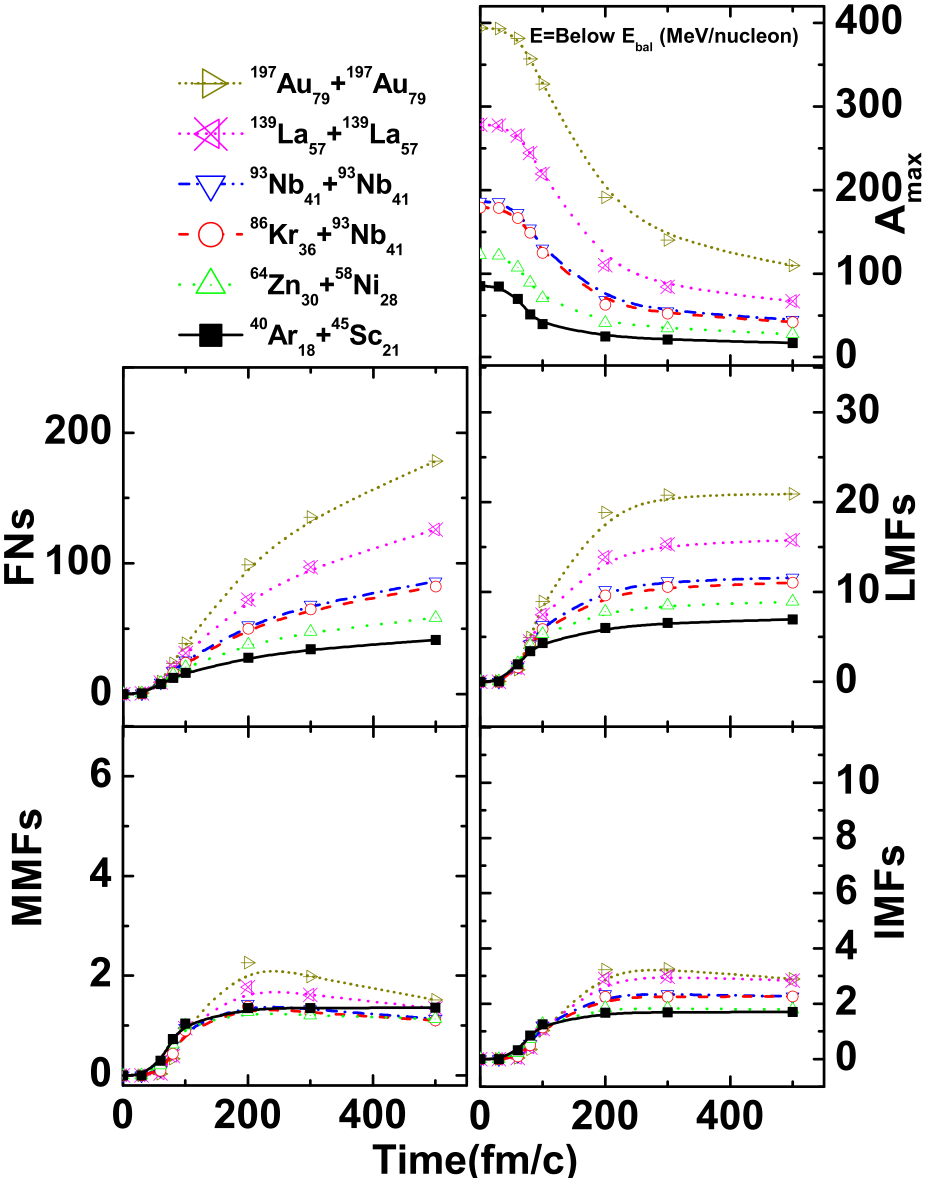

Figure 4.5: Same as in Fig.4.3, but for the reactions of $^{197}Au +^{197} Au$, $^{139}La +^{139} La$, $^{93}Nb +^{93} Nb$, $^{86}Kr +^{93} Nb$, $^{64}Zn +^{58} Ni$, $^{40}Ar +^{45} Sc$ at 40 MeV/nucleon.

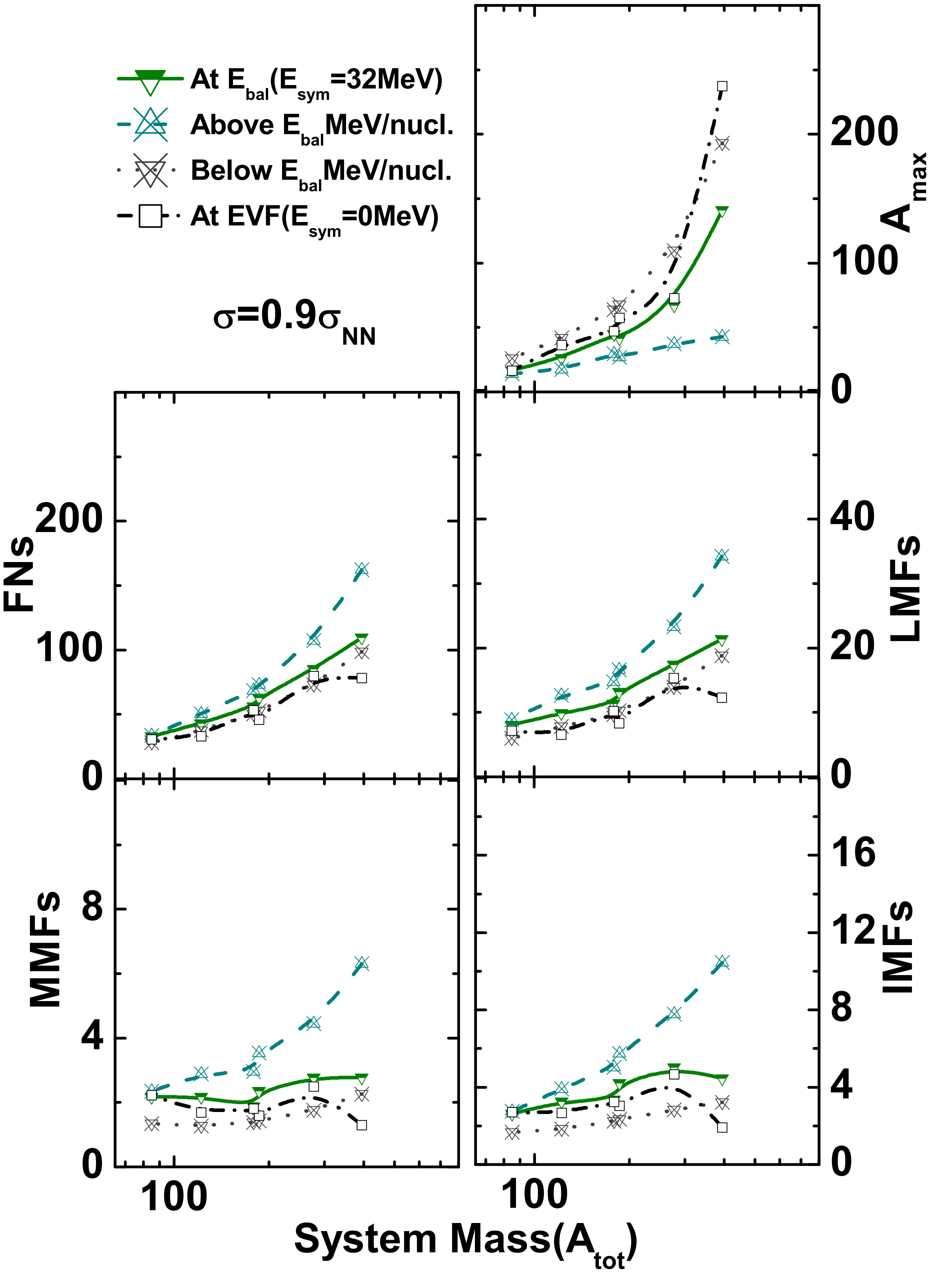

Figure 4.6: Multiplicities of A_{max}, FNs, LMFs, MMFs, IMFs as a function of composite mass of colliding nuclei (A_T+A_P) for the reactions of $^{197}Au+^{197}Au$, $^{139}La+^{139}La$, $^{93}Nb+^{93}Nb$, $^{86}Kr+^{93}Nb$, $^{64}Zn+^{58}Ni$, $^{40}Ar+^{45}Sc$ at, above, below and at EVF with $E_{sym}=0MeV$.

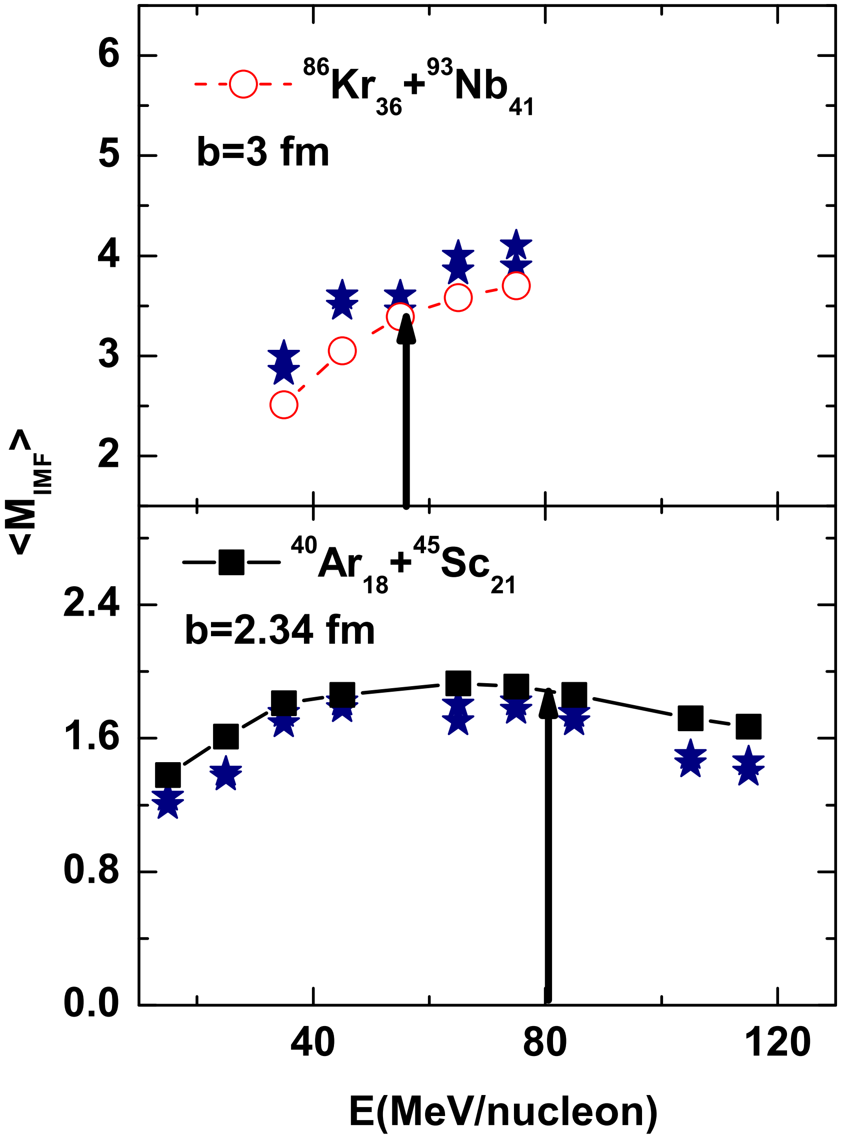

Figure 4.7: The average multiplicity of IMFs vs beam energy for the reaction of $^{86}Kr+^{93}Nb$ and $^{40}Ar+^{45}Sc$. The stars represent the NSCL experimental results.

4.3.2 Mass and incident energy dependence of fragment production

In Fig.4.6, we display the A_{max}, FNs, LMFs, IMFs and MMFs as a function of the system mass at all three incident energies i.e. at EVF with $E_{sym} = 32MeV$, below 40 MeV/nucleon, above 100 MeV/nucleon and at EVF with $E_{sym} = 0MeV$. From the figure, it is clear that no typical structure is obtained at the energy of vanishing flow with $E_{sym} = 32MeV$ and $E_{sym} = 0MeV$. As noted in ref. [137], multiplicity of various fragment show power law dependence without any particular structure at energy of vanishing flow. For lighter system there is not much change at all EVF, i.e., multiplicities of all fragment (A_{max}, FNs, LMFs, IMFs and MMFs) remains same. This is due to fact that balance energy in lighter colliding nuclei is very high and lesser repulsions are produced when two lighter nuclei collide, so multiplicity of all fragments get reduced. As the system mass increases multiplicities of all fragments shows difference at all EVF due to more repulsion between two nuclei. Multiplicities of fragments is more for above EVF, and lesser for below EVF. Both EVF (above and below) are continuously increases as the system mass increases. With symmetry energy multiplicity of fragments is more as compared to without symmetry energy. But multiplicity of all fragments show slight decrease with increase in system mass for both EVF ($E_{sym} = 32MeV$, $E_{sym} = 0MeV$).

In the Fig.4.7, multiplicity of IMFs in $^{86}Kr +^{93} Nb$, $^{40}Ar +^{45} Sc$ are displayed as a function of beam energy at scaled impact parameter $\hat{b} = 0.3$ (semi central collisions) using isospin dependent reduced cross section ($\sigma = 0.9\sigma_{NN}$) [81]. Final results are compared with NSCL experimental data [188]. The trend obtained is in agreement with the experimental findings. Multiplicity of IMFs decreases with increase in beam energy for $^{40}Ar_{18} +^{45} Sc_{21}$ and increase with increase in beam energy for $^{86}Kr_{36} +^{93} Nb_{41}$ system. This is due to fact that incident energy is much higher in lighter system as compared to heavier system. It is also clear from experimental data that no particular structure is obtained at the energy of vanishing flow (EVF) as shown by arrow in this figure.

4.4 Summary

By using the isospin dependent quantum molecular dynamic model, we studied the fragment structure at, above and below the balance energy. Also we have carried out the systematic study of mass dependence in multifragmentation around the balance energy using isospin-dependent reduced cross-section ($\sigma = 0.9\sigma_{NN}$). We find that, disappearance of flow and multifragmentation scales with the size of the interacting system that can be parametrized in terms of power law $C(A_{tot})^{\tau}$. From the energy dependence of IMFs it is clear that fragmentation produced due to two colliding nuclei does not follow any particular structure at the energy of vanishing flow.

Chapter 5

Correlation between balance and transition energy

5.1 Introduction

The collective motion can be characterized by several ways that pin down different space-momentum correlations generated by the simulation of reactions at intermediate energies. The kind of collective flows that have been suggested and employed to get information on the equation of state (or the mean field) can be divided into three categories: radial, sideward and elliptic. The sideward and elliptic flows are currently useful tools to study of compressibility of symmetric nuclear matter. The sideward or directed flow is discussed in detail in chapter 3. In this chapter we will discuss about elliptic flow. The word **elliptic** is due to the fact that in polar co-ordinates, the azimuthal distribution with non-zero second harmonic represents an ellipse. Two different signatures of the elliptic flow as shown in Fig.5.1 have been predicted. a) The bounce-off [189] of the compressed matter in the reaction plane and b) The squeeze-out [190] of the participant matter out of the reaction plane.

The most strongly stopped, compressed matter around the mid-rapidity is seen directly in the squeeze-out [191]. A strong dependence of these collective effects on the nuclear equation of state is also predicted [191]. For higher beam energies, however, projectile and target spectator decouple quickly from the reaction zone, giving way to a preferential emission of the matter in the reaction plane, even at the mid-rapidity [192]. An excitation function of the squeeze out at midrapidity shows the transition from the out-of-plane enhancement to preferential in-plane emission.

In the previous chapter, we have studied the directed flow which is anti-symmetric with respect to ϕ distribution for the forward rapidity ($Y_{cm} > 0$) and backward rapidity ($Y_{cm} < 0$) whereas elliptic flow has the same distribution in both rapidity regions, at least for the

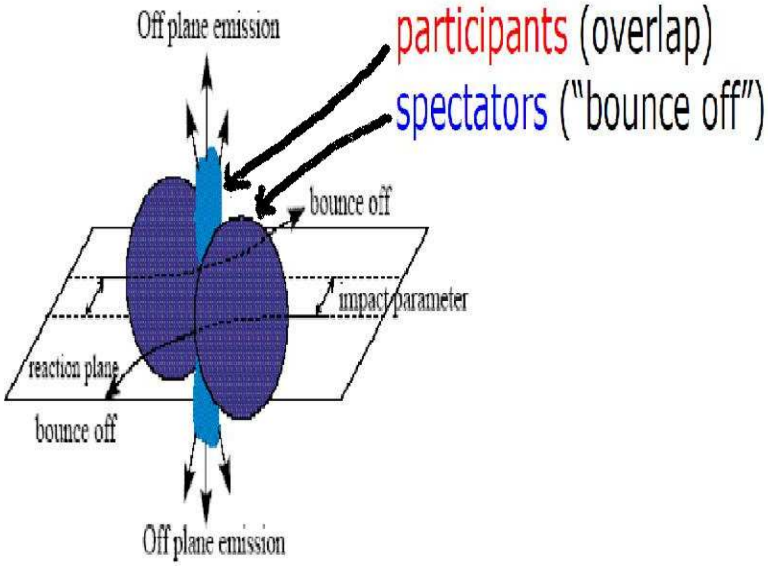

Figure 5.1: In-plane bounce-off caused by compression and squeeze-out caused by enhanced emission of light particles perpendicular to plane close to midrapidity.

symmetric colliding nuclei. The important feature of both directed and elliptic flow is the existence of the transitions between both forms. Both the transitions amount to measuring the "zeroes" in the flow excitation functions, or the energy dependence of the flow variables. Measuring zero is mostly free from the difficulties inherent in the theory-data comparison for finite flow values [163].

In this chapter, we study the azimuthal anisotropy of the mean particle momentum $\langle v_2 \rangle$ thought to be originating from the azimuthal anisotropy in collective flow ("elliptic flow"), has long been regarded as an important observable in heavy ion collisions. The main reason for this is that elliptic flow has long been understood to be "self-quenching" [193]. The azimuthal pressure gradient extinguishes itself soon after the start of the hydrodynamic evolution, so the final $\langle v_2 \rangle$ is insensitive to the later stages of the fireball evolution and therefore allows us to probe the hottest, best thermalized, and possibly deconfined phase. The elliptic flow reflects the anisotropy in the particle transverse momentum (P_t) distribution at midrapidity, and is defined as the average difference between the square of the X and Y components of the particle's transverse momentum. Mathematically, it can be written as

$$v_2 = \langle \frac{P_x^2 - P_y^2}{P_x^2 + P_y^2} \rangle, \tag{5.1}$$

where P_x and P_y are the X and Y components of the momentum; P_x is in the reaction plane, while P_y is perpendicular to the reaction plane and the average is taken over all particles of

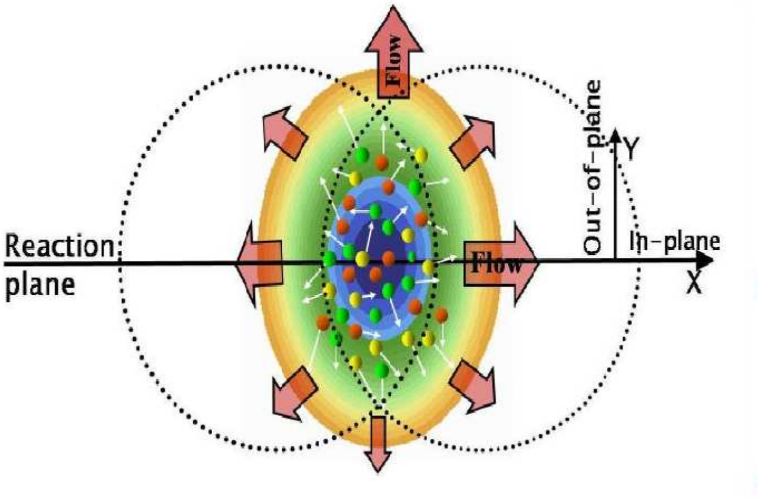

Figure 5.2: Illustration of elliptic flow shows possible movement of nucleons in the compressed zone. The direction of in-plane and out-of-plane emission is shown in this figure [129].

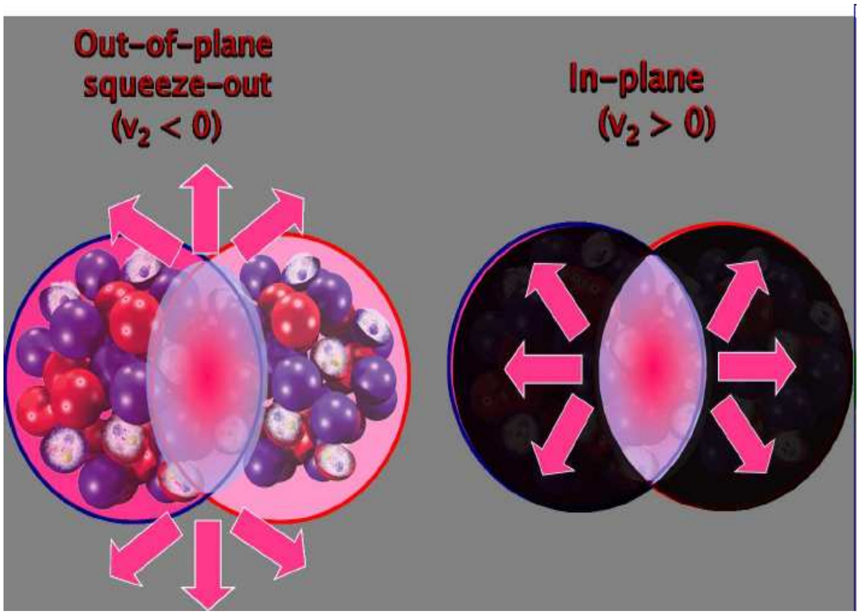

Figure 5.3: In-plane (right side) and out-of-plane (left side) emission of nucleons in the reaction plane and perpendicular to reaction plane is presented [129].

a given kind in all events [193].

Elliptic flow refers to the anisotropy of the ϕ distribution at midrapidity and its value indicates whether or not particle emission is in-plane or out-of-plane. Azimuthal distributions which are peaked at 0^o and 180^o exhibit predominantly in-plane emission, while ϕ distributions peaked at $\pm 90^o$ signify out-of-plane emission as shown in Figs.5.2 and 5.3. The term elliptic, initially, was known with the names like "Squeeze-out", "rotational motion", or "anisotropic flow", because the shapes of ϕ distributions at mid rapidity resemble ellipse with a major axis along the x-axis (in-plane emission) or y-axis (out-of-plane emission). The term "elliptic flow" was introduced in 1997 by H. Sorge [139], a theoretician at SUNY-Stony Brook.

This study is a continuation of our previous study [81], in which we showed that experimental balance energies can be explained well with a reduced isospin-dependent NN cross section with a hard equation of state. In the present study, our aim is to pin down the relation between the balance energy (E_{bal}) and transition energy (E_{trans}).

5.2 Anisotropic flow

The elliptic flow is a measure that quantifies the azimuthal anisotropy of the momentum distribution. Specifically, we fit the azimuthal distribution of nucleons about the reaction plane with a Fourier expansion of the form [194, 195]

$$\frac{dN}{d\phi} = v_0(1 + 2v_1 Cos\phi + 2v_2 Cos2\phi + ...), \tag{5.2}$$

where v_0 is for normalization only, $\langle v_1 \rangle$ characterizes the directed in-plane flow, $v_2 > 0$ indicates in-plane enhancement, $v_2 < 0$ characterizes the squeeze-out perpendicular to the reaction plane, and $v_2 = 0$ shows an isotropic distribution of nucleon momentum in the transverse plane. Hence, the ellipticity coefficient $\langle v_2 \rangle$ depends on the in-plane and out-of-plane flow amplitudes. In addition, the anisotropy ratio is defined by

$$R_n = \frac{1 - 2v_2}{1 + 2v_2}. \tag{5.3}$$

If R_n larger than unity, it signals a preferred out-of-plane emission, and smaller than one shows in-plane flow [196]. The first coefficient of the Fourier expansion of the azimuthal distribution of the emitted particles $\langle v_1 \rangle$ describes the directed in-plane flow discussed in **chapter 3**. The directed flow measures the total amount of the transverse flow. It is most pronounced in semi-central interactions around target and projectile rapidities where the spectators are deflected away from the beam axis due to a bounce-off from the compressed and heated matter in the overlap region. $\langle v_1 \rangle$ is defined by

$$v_1 \;=\; \langle cos(\phi - \phi_{RP}) \rangle, \tag{5.4}$$

where ϕ denotes the azimuthal angle of one outgoing particles and ϕ_{RP} is the azimuthal angle of the reaction plane. The angular brackets denote an average over all considered particles from all events. The second coefficient of the Fourier expansion of the azimuthal distribution of the emitted particles $\langle v_2 \rangle$ is called elliptic flow [139, 193, 197]. This type of flow is strongest around central rapidities in semi-peripheral collisions. It is driven by the anisotropy of the pressure gradients, due to the geometric anisotropy of the initial overlapping region. Therefore, it is a valuable tool to gain insight into the expanding stage of the fire ball $\langle v_2 \rangle$ is defined by

$$v_2 \;=\; \langle cos[2(\phi - \phi_{RP})] \rangle. \tag{5.5}$$

The elliptic flow parameters $\langle cos2\phi \rangle$ at energies from tens to hundreds of MeV/nucleon are determined by the complex interplay among expansion, rotation, and the shadowing of spectators. Both the mean-field and two-body-collision parts play important roles in this energy range. The mean field plays a dominant role at low energies, and then, gradually, the two-body collision becomes dominant with the increase in energy. So, there are two competing effects that lead to contributions with different signs to the integrated $\langle v_2 \rangle$ value. At low energies or early times there is the so-called squeeze-out effect. The spectator matter blocks the emission in the impact parameter direction and therefore the flowing matter is squeezed out perpendicularly to the reaction plane. This leads to negative elliptic flow values. The second effect is the so called in-plane flow illustrated by the following picture: This type of flow becomes important at higher energies and/or later times. At higher bombarding energies ($E \geq 1$A GeV) the spectators leave the interaction zone rapidly. The remaining hot and dense matter expands almost freely, where the surface is such that in-plane emission is preferred. Therefore, the elliptic flow receives a positive contribution. It is due to the interplay between the time scales of the passing time of spectators and the expansion time of the dense stopped interaction zone that determines the time-integrated elliptic flow signal. Indeed, when following the elliptic flow as a function of reaction time, early out-of-plane squeeze is superposed by later preferential in-plane expansion [139].

5.3 Experimental and theoretical study of elliptic flow

Experimentally observed out-of-plane emission, termed squeeze, was first observed by at Saturne (France) by the DIOGENE Collaboration [198]. The Plastic Ball group at the Bevalac in Berkeley quantified the squeeze-out in symmetric systems [199]. Recently, elliptic flow has been measured at the Relativistic Heavy Ion Collider (RHIC) in Au + Au collision at $\sqrt{s} = 130$ GeV/nucleon [200]. At top Alternating-Gradient Synchrotron (AGS) and Super Proton Synchrotron (SPS) energies, elliptic flow is inferred to be a relative enhancement of emission in the plane of the reaction.

Elliptic flow is developed mostly in the first several fm/c (of the order of the size of nuclei) after the collision and thus, provides information about the early-time thermalization achieved in the collision [201]. A large elliptic flow of all charged particles near midrapidity was reported by the STAR Collaboration [201]. The FOPI, INDRA, and Plastic Ball Collaborations [156, 202] are actively involved in measuring the excitation function of the elliptic flow from Fermi energies to relativistic energies. Interestingly, at intermediate energies ($E \approx 100$ MeV/nucleon), the change from in-plane emission (rotation-like behavior) to squeeze-out is predicted [167, 203] whereas at relativistic energies ($E \approx 5$ GeV/nucleon) the opposite change from the squeeze-out to in-plane enhancement is observed. Elliptic flow requires re-interactions within the produced matter as a mechanism for transferring the initial spatial deformation of the reaction zone in noncentral collision onto momentum space. It is thus plausible to expect that the largest elliptic flow signal is produced in the hydrodynamic limit and an almost linear increase in its value with the particle transverse momentum below 1.5 GeV/c. In the hybrid model of combining the hydrodynamic model with the relativistic quantum molecular dynamics (RQMD) transport model [204] and choosing certain effective equations of state, it is possible to obtain an elliptic flow that is comparable to the measured ones in heavy-ion collisions at both SPS and RHIC energies [205].

The experimental result shows that elliptic flow first increases with particle transverse momentum and then levels off. The dependence of the elliptic flow on both the charged-particle multiplicity [206, 207] and the particle pseudorapidity [207] has also been measured. A complete study of the excitation function of transverse momentum and the energy dependence of elliptic flow in the entire energy region can provide useful information about nucleon-nucleon interactions related to the nuclear equation of state. In the literature, many attempts have already been made for hard equations of state (EOS) with free NN cross section and for soft EOS with a reduced nucleon-nucleon cross section with and without momentum-dependent interactions, and studies have also tried to explore different aspects of directed sideward flow.

5.4 Results and Discussion

We study the elliptic flow using a hard equation of state along with isospin-dependent reduced cross section (σ= 0.9 σ_{NN}) by simulating various reactions as discuss in chapter 3. The time evolution of the reaction is followed upto 200 fm/c. This is the time at which flow saturates for lighter as well as for heavier systems. For this study, the reactions of $^{40}Ar_{18}$ + $^{45}Sc_{21}$ ($\hat{b}$ = 0.4, L=0.5L), $^{93}Nb_{41}$ + $^{93}Nb_{41}$ ($\hat{b}$ = 0.3, L=0.7L), $^{139}La_{57}$ + $^{139}La_{57}$($\hat{b}$ = 0.3, L=0.8L), and $^{197}Au_{79}$ + $^{197}Au_{79}$ (b=2.5 fm, L=L) are simulated, where L is the Gaussian width. As mentioned in Ref. [30, 81, 177], in IQMD the value of Gaussian width L depends on the mass of the system. For Au nuclei L=8.66fm^2 and for Ca nuclei L=4.33fm^2. $\hat{b}$ is the scaled impact parameter, defined as $\hat{b} = \frac{b}{b_{max}}$ [where b is particular impact parameter in fermi and $b_{max} = 1.12(A_T^{1/3} + A_P^{1/3})$], and A_T and A_P are the mass of the target and projectile, respectively. The choice of impact parameter is guided by the experimentally extracted information [141-144, 174]. These reactions have been performed at their corresponding balance energies. The above reactions were simulated between 40 and 1200 MeV/nucleon using the hard equation of state along with isospin-dependent reduced cross section. The phase space generated by the IQMD model has been analyzed using the minimum spanning tree (MST) [5] method. The MST method binds two nucleons in a fragment if their distance is less than 4 fm. In recent years, several improvements have also been suggested. One of the improvement is to also imply a momentum cut of the order of Fermi momentum. This method is dubbed the MSTP method [134]. The entire calculations are performed at t = 200 fm/c, i.e., saturation time.

5.4.1 Transverse momentum (P_t) dependence of elliptic flow $\langle v_2 \rangle$ and anisotropy ratio (R_n)

In Fig.5.4, we display the transverse momentum dependence of elliptic flow for the free nucleons (FNs) (A=1), light mass fragment (LMFs*) ($1 \leq A \leq 4$) and LMFs ($2 \leq A \leq 4$). A Gaussian-type behavior is observed in all cases. This Gaussian type behavior is quite similar to one obtained by Colona and Toro *et al.* [208]. Note that this elliptic flow is integrated over the entire rapidity range. There is a linear increase in the elliptic flow with

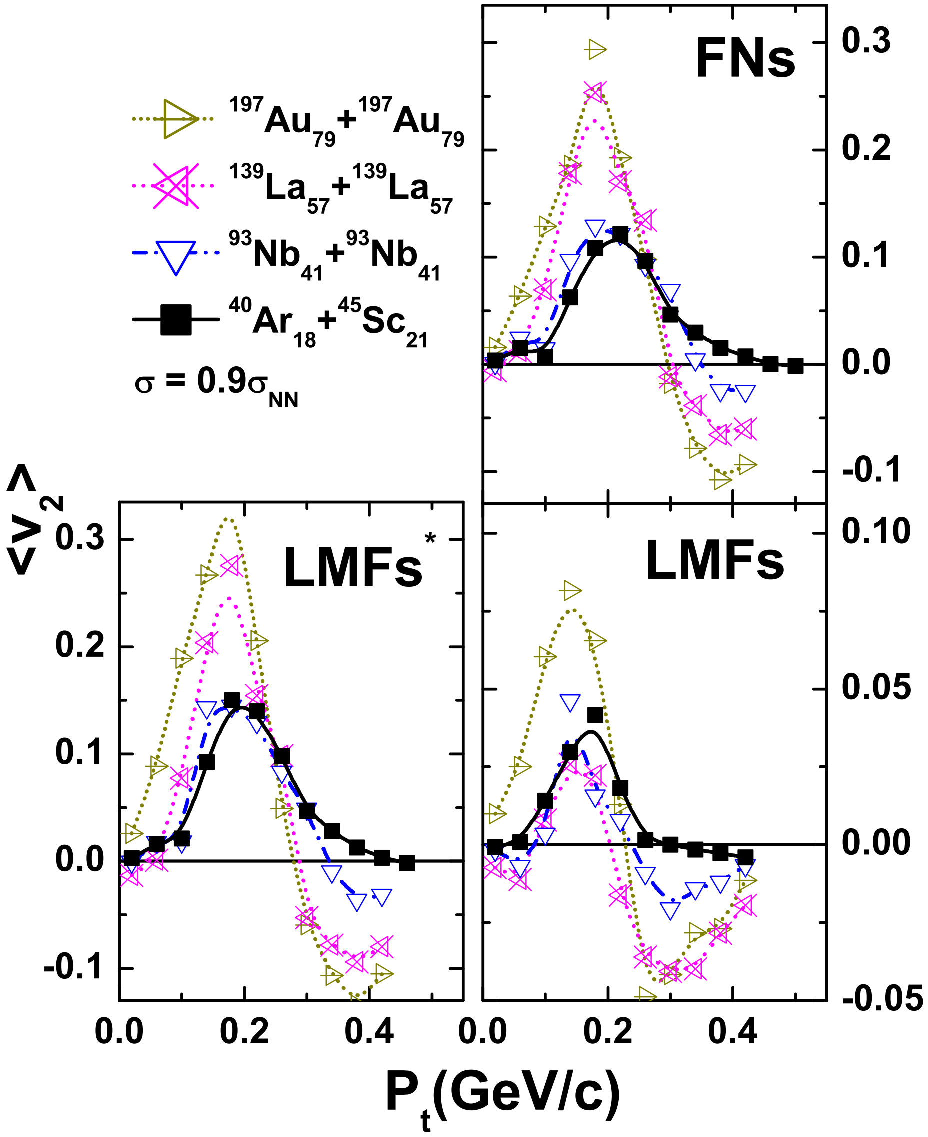

Figure 5.4: Transverse momentum dependence of the elliptical flow at $E = 200$ MeV/nucleon. The different lines show the variation with different system masses, and different panels show the fragments of different mass ranges.

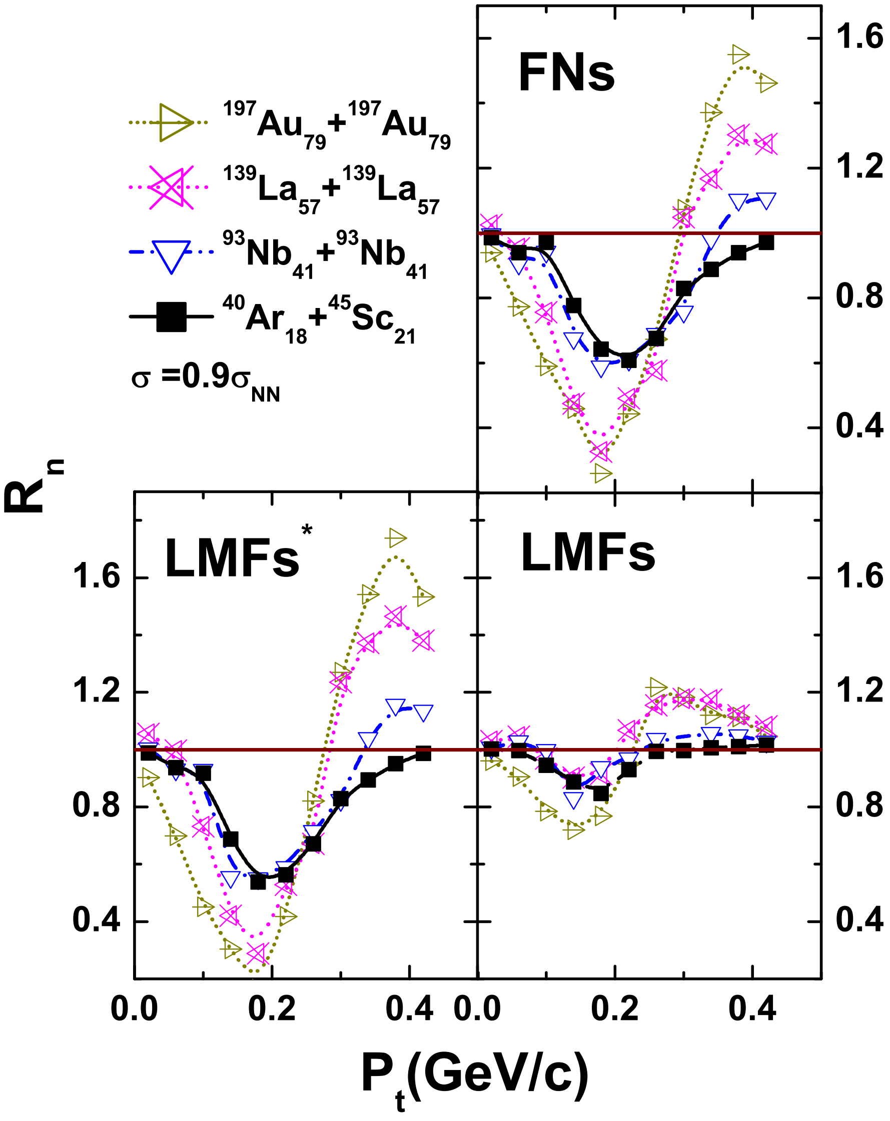

Figure 5.5: Same as in Fig.5.4 but for the transverse momentum dependence of the anisotropy ratio (R_n).

transverse momentum upto certain range of P_t. This is due to fact that particles with large momentum will escape the reaction zone earlier and hence leads to an increase in flow. After certain range of transverse momentum, it starts decreasing due to decrease of number of particles in that particular P_t range. In the start of reaction, number of particles increases and the average value of the momentum of corresponding particles increases and hence large positive value of elliptic flow is obtained. With time as reaction proceed further, number of particles decreases and the average value of the momentum of corresponding particles decreases and hence decrease in the positive value of elliptic flow. Positive value of elliptic flow signifies in-plane and negative value signifies out-of-plane emission of nucleons. It is also evident from Fig.5.4 that the peaks of the Gaussian shift toward lower values of P_t for FNs and LMFs* with increase in the mass of system. This is due to the fact that the FNs and LMFs* feel the mean field directly, while LMFs have weaker sensitivity [209]. This weak sensitivity of the mean field is due to the indirect pairing between the nucleons of the projectile and target in the compressed participant zone for LMFs compared to LMFs* where direct pairing takes place between the nucleons.

In Fig.5.5, we display the transverse momentum dependence of anisotropy ratio for the FNs, LMFs* and LMFs. Ratio R_n larger than unity, signals a preferred out-of-plane emission, and smaller than one shows in-plane flow [196]. A Gaussian-type behavior is observed in all cases as in Fig.5.4 but in opposite direction. As we increase the fragment mass range the in-plane and out-of-plane emission of nucleon increases whereas for LMFs the in-plane and out-of-plane emission both decreases significantly. It is also evident from the figure that the peak of the Gaussian shifts towards lower values of P_t for FNs and LMFs* with increase in the mass of system. But no such systematic trend for LMFs is observed.

5.4.2 System mass dependence of transverse momentum and ΔE

First of all, we study elliptic flow by analyzing the system size dependence of transverse momentum and (E_{trans}-E_{bal}) for free nucleons and light mass fragments and then parametrized it in terms of a power law C$(A_{tot})^{\tau}$. In Fig.5.6, we display the system size dependence of the transverse momentum at which $\langle v_2 \rangle$ becomes zero for different systems and different fragments shown in Fig.5.4. The value of transverse momentum decreases with system mass because in heavier systems there are more Coulomb repulsion than in lighter systems. Free nucleons and LMFs* shows almost similar trend. This is due to fact that FNs feels the mean field directly and LMFs* also includes FNs as compared to LMFs in which there is absence

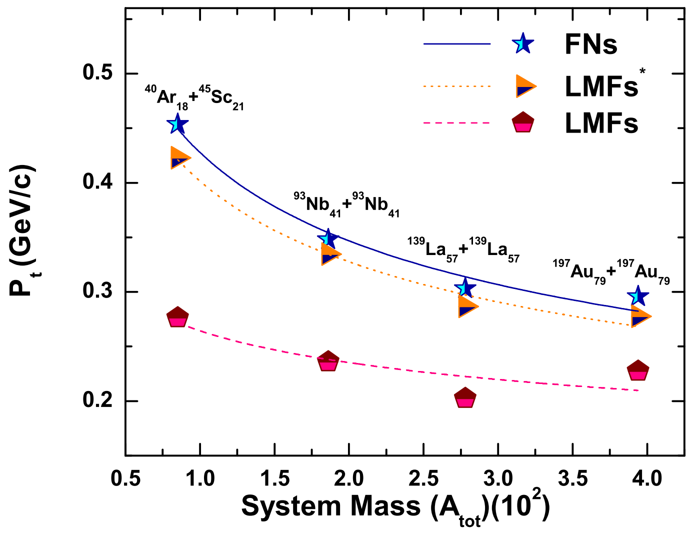

Figure 5.6: Transverse momentum dependence P_t for elliptic flow as a function of the combined system mass for different systems with fragments of different mass ranges.

of FNs. So, transverse momentum is more for LMFs*. The system mass dependence of transverse momentum is again fitted with a power law of the kind

$$P_{trans} = C(A_{tot}^{-\tau}). \tag{5.6}$$

The value of τ is found to increase with an increase in fragment mass range. In the case of FNs it is -0.30 ± 0.03, for LMFs* it is -0.29 ± 0.02, and for LMFs it is -0.17 ± 0.07.

In Fig.5.7, we display the system size dependence of the difference of transition energy $\Delta E(\%) = \frac{E_{trans}-E_{bal}}{E_{bal}} \times 100$ extracted from Fig.5.8 for different fragments and the balance energy E_{bal} ($\sigma = 0.9\sigma_{NN}$) studied in Ref. [81]. The origin of balance and transition energy is different. The balance energy counter balances the mean field and NN collisions, while transition energy is due to more complex effects such as expansion of compressed zone and shadowing of cold spectator part. For a fragment with low mass range this difference shows a slight decrease as we increase the system mass, and then other effects come into play (i.e., expansion of participant and shadowing of spectator matter), whereas for light mass fragment very small variation is obtained, which means the additional effect is independent of system mass. This shows that the transition energy E_{trans} and balance energy E_{bal} are closer for the heavy mass system compared to lighter systems. This happens because as the number of neutrons increases, the number of collision increases and hence leads to a decrease in transition energy. This dependence is again fitted with the power law. The value of τ is found to increase with an increase in fragment mass range. In the case

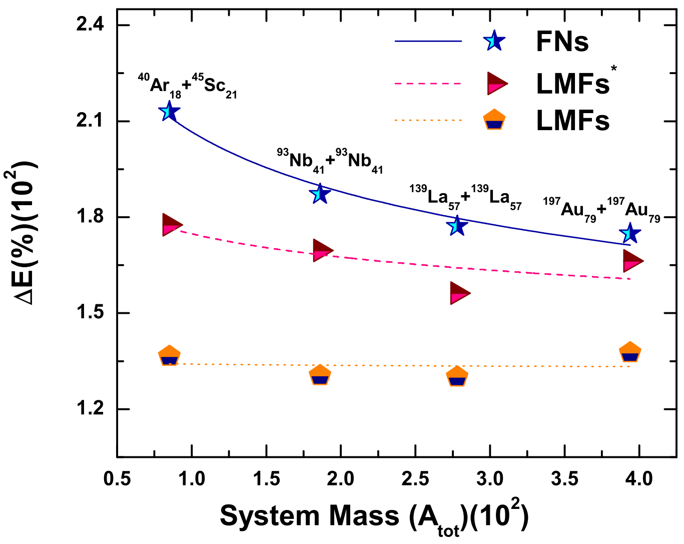

Figure 5.7: Difference of the transition energy and balance energy as a function of mass of system.

of FNs it is -0.14 ± 0.017, for LMFs* it is -0.061 ± 0.036, and for LMFs it is -0.0043 ± 0.031.

5.4.3 Energy dependence of the elliptic flow and comparison with experimental data

In Fig.5.8, we display the variation of the elliptic flow $\langle v_2 \rangle$ for free nucleons, LMFs* and LMFs over the midrapidity region as a function of energy. This figure shows the excitation function of the in-plane/squeeze-out flow parameter $\langle v_2 \rangle$. The FNs and LMFs*, which originate from the participant zone, show a systematic behavior with the beam energy and with the composite mass of the system. The elliptic flow for these particles is found to become more negative with the increase in the composite mass of system and with the increase in the beam energy. The heavier the system is, the greater the Coulomb repulsion is and the more negative the elliptical flow is.

The elliptic flow is found to show a transition from in-plane to out-of-plane at a certain beam energy known as the transition energy E_{trans} for the midrapidity region [30, 81, 177]. This is due to the change in the rotational behavior into expansion with an increase in the incident energy.

In Fig.5.9, we show $\langle v_2 \rangle$ at midrapidity $|Y| = |\frac{Y_{cm}}{Y_{beam}}| \leq 0.1$ for Z=2 as a function of incident energy. The rapidity cut is in accordance with the experimental findings. The theoreti-

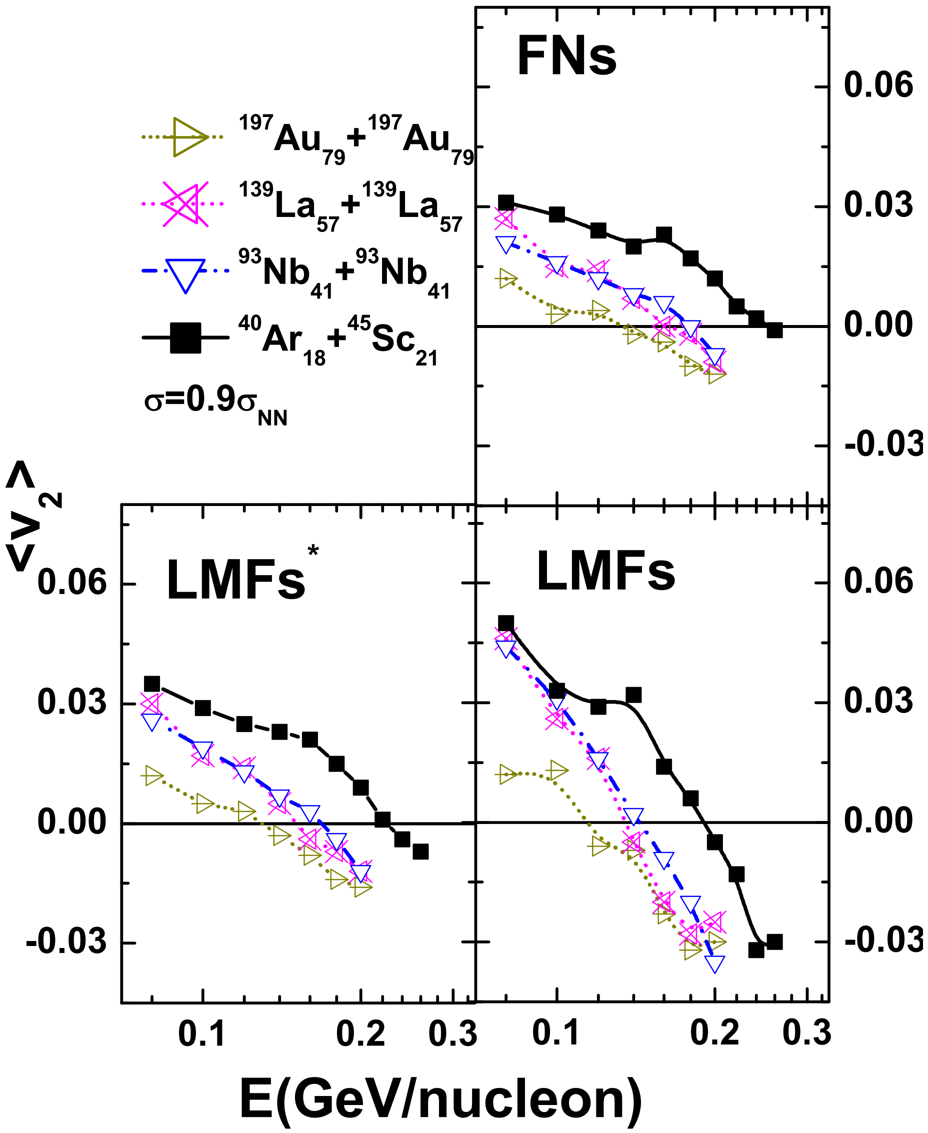

Figure 5.8: Variation of the elliptic flow, with beam energy at $|Y| = |\frac{Y_{cm}}{Y_{beam}}| \leq 0.1$ for different reactions.

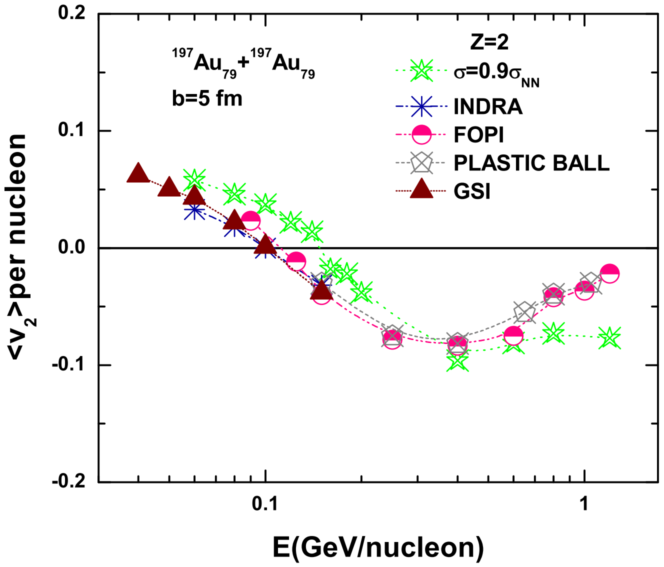

Figure 5.9: Energy dependence of the elliptic flow for Au + Au systems and its comparison with the experimental data.

cal results are compared with the experimental data extracted by the INDRA, FOPI, and Plastic Ball Collaborations [156, 202]. With the increase in the incident energy, the elliptic flow $\langle v_2 \rangle$ changes from positive to negative values, exhibiting a transition from the in-plane to out-of-plane emission of nucleons. This is because the mean field, which contributes to the formation of a rotating compound system, becomes less important and the collective expansion process based on the nucleon-nucleon scattering starts to be predominant. The maximal negative value of $\langle v_2 \rangle$ is obtained around E = 500 MeV/nucleon with a reduced isospin-dependent cross section. This out-of-plane emission decreases again towards higher incident energies. This happens due to faster movement of the spectator matter after $\langle v_2 \rangle$ reaches the maximal negative value [202]. This trend is in agreement with experimental findings. A close agreement with data is obtained in the presence of the hard equation of state and with a reduced isospin-dependent cross section for Z=2 particles. Similar results and trends have also been reported by Zhang *et al.* in their recent communication [210].

5.5 Summary

By using the IQMD model, we have studied the correlation between transition energy E_{trans} and balance energy E_{bal}. We have investigated the elliptical flow of fragments for different reacting systems at incident energies between 40 and 1200 MeV/nucleon using the isospin-dependent quantum molecular dynamics model. We have studied transverse momentum dependence of elliptic flow of different fragments for different systems and find that the peaks of the Gaussian shift toward lower values of P_t for FNs and LMFs* with increase in the mass of system.

The elliptical flow is found to show a transition from in-plane to out-of-plane at a certain beam energy in the midrapidity region. Our calculation with a stiff equation of state and a reduced isospin-dependent nucleon-nucleon cross section ($\sigma = 0.9\sigma_{NN}$) is in good agreement with the experimental findings. The difference between the balance and transition energy decreases with the increase in the composite mass of colliding nuclei. This tells us that due to the increase of neutrons to colliding nuclei, the difference between the two energies decreases.

Chapter 6

Effect of spatial and momentum correlation on multifragmentation

6.1 Introduction

As stated in previous chapters, multifragmentation, a complex phenomenon in nature, has been of central interest in heavy-ion physics research because of its richness in the experimental data. Experimental studies have shown that colliding nuclear matter can break into a large number of light particles and intermediate mass fragments (IMFs) depending on the incident energy, mass of the system [112, 113, 183-185, 211-213] and impact parameter of the reaction [214, 215]. Several interesting features of multifragmentation as a function of bombarding energy and impact parameter were observed or predicted [42, 84, 111-113, 216-218]. This includes a rise and/or fall in the fragment production with a change in the impact parameter [42, 84, 111-113, 216-218]. Statistical and dynamical models (discussed in chapter 4) though differ in their assumptions are able to explain one or other features of the experimental findings. One should, however, keep in the mind that the multifragmentation is a many body phenomena, therefore, molecular dynamical models are excellent tools to investigate the fragmentation.

The multifragmentation has been studied using a variety of nuclei and over a wide domain of incident energy. Multifragmentation is a universal phenomenon occurring when a large amount of energy is deposited in a nucleus leading to the fast disintegaration of nucleus into various fragments. Before the study of the origin of fragments one has to identify them by using the secondary algorithm.

6.2 Method used for clusterization of fragments

The most widely used clusterization method is to look for spatial correlation. This method is also called the minimum spanning tree (MST) method [5, 73] shown in Fig.6.1. In this method we simulates the reaction for about 200 fm/c. Two nucleons share the same fragment in MST, if their spatial distance is less than or equal to 4 fm [5, 73], i.e.

$$|r_i - r_j| \leq 4fm, \tag{6.1}$$

This procedure yields stable results, i.e., gives the same yield and fragment pattern at the end of the reaction where clusters are cold and well separated. In addition to Eqn.6.1 we also check the relative momenta of the nucleons. Therefore, we demand two nucleons obeying Eqn.6.1 also to fulfil [110]

$$|p_i - p_j| \leq p_{Fermi}, \tag{6.2}$$

where p_{Fermi} is the average Fermi momentum of the nucleons bounded in a nucleus at its ground state which, in IQMD model, is about 240 MeV/c. This definition discards all those nucleons which are too far in their momentum space. We term this extension the minimum spanning tree method with a momentum cut (MSTP method). Naturally the normal MST method depends on spatial distance and so the fragments thus created can have nucleons with very large relative momenta [110, 134]. The origin of fragments formed in central and peripheral collisions are different. In central reactions, due to frequent nucleon-nucleon collisions, an appreciable part of the nuclear matter is in the form of emitted nucleons while most of the initial correlations among the nucleon are destroyed, hence relative momenta of nucleons bounded in the same fragment can be quite large. This leads to the creation of an unstable and unbound fragment. After a while these fragments and therefore one has to follow the reaction dynamics for quite a long time to obtain stable and properly bounded fragments. In contrast, the picture for peripheral collisions is different. In peripheral collisions, many of initial correlations are preserved and hence fragments are reasonably bounded. To get a stable fragment relative momenta of nucleons need to be considered. So, we deny the nucleon to be in the same fragment if their relative momenta are very large [110, 134]. In these collisions, energy depositions reached, cover the range from particle evaporation to multifragment emission, up to total disassembly of the system, the so-called rise and fall of fragment emission [42, 219, 220].

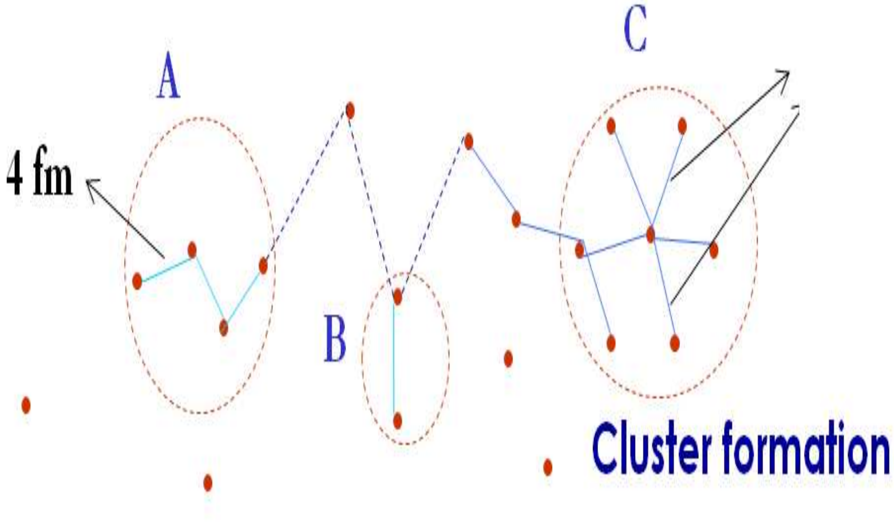

Figure 6.1: Clusterization of fragments using MST method.

6.3 Experimental and theoretical analysis done on multifragmentation

Experimental analysis of the emission of IMFs has yielded several interesting observations: De Souza *et al.* [216] observed a linear increase in the multiplicity of IMFs with incident energies for central collisions. In this study, incident energy was varied between 35 and 110 MeV/nucleon. On the other hand, Tsang *et al.* [218] reported a rise and fall in the production of IMFs. The maximal multiplicity of the IMF shifts between nearly central and peripheral collisions with increase in the incident energy. More refined results were reported by Peaslee *et al.* [111] for the reaction of $^{84}Kr_{36} +^{197} Au_{79}$ for incident energy between 35 and 400 MeV/nucleon. Their analysis revealed that multiplicity of IMFs first increases up to 100 MeV/nucleon and then decreases slowly. ALADIN experiments have provided extensive information about multifragmentation of projectiles in peripheral nucleus-nucleus collisions at high energy [42]. They showed a rise and fall behavior of fragmentation with excitation energy, and it has been shown that the temperature remains nearly constant, around $T \approx 5$ MeV, during this process [221]. There are large fluctuations of the fragment multiplicity and of the size of the largest fragment in the transition region from a compound-like decay to full multifragmentation of spectators [41]. It was found that the statistical models and dynamical models are fully consistent with the data [58, 222]. These findings pose a stringent test for any theoretical model designed for the study of multifragmentation.

Theoretically, one would need to understand the range of interaction and the cut-off limit of spatial correlation for a fragment; these depend on the average nucleon-nucleon distance in medium. We first simulate the reaction for about 200 fm/c, then the spatial distance between the nucleons is checked. As a nucleon is a part of fragment if their spatial separation is less than or equal to 4 fm, i.e., $|r_i - r_j| \leq 4$ fm [30, 81, 83], this procedure yields stable results, i.e. gives the same fragment pattern for times later than 200 fm/c, but it cannot be used at earlier times because it only makes sense when the system is very dilute and clusters are well separated from each other.

To define the fragmentation pattern, we assume that nucleons from the target and projectile form a fragment and free nucleons. The nucleons inside these fragments can interact with each other; they do not interact with nucleons from other fragments or with free nucleons. The most bound fragmentation is realized in nature. It is explained in the literature that to find the most bound configuration among a huge number of possible fragmentation patterns, a pattern is chosen by dividing the whole system into few fragments. Energy of an individual cluster is then calculated. The energy determined in this way differs from the total energy of the system [83]. This method is dubbed as Simulated Annealing Clusterization Algorithm (SACA) which is very time consuming as compared to MST and MSTP method.

6.4 Optimization of values of spatial and momentum constraints

In the present chapter, we want to optimize the value of spatial distance and relative momentum between nucleons to form clusters. The MST method used most extensively to clusterize the nucleons [5, 73, 134]. In the MST method, two nucleons are deemed to share the same fragment if their centroids are closer than a certain distance $|r_i - r_j| \leq R_{clus}$. In this chapter we vary the value of R_{clus} between 2-8 fm. The MST with momentum cut (MSTM) method also takes care of the relative momentum of nucleons [110, 134]. Along with the restriction on the spatial arrangement of nucleons, a restriction is put on the momentum space of nucleons i.e. $|p_i - p_j| \leq P_{clus}$. We vary the value of P_{clus} between 130-300 MeV/c. The parameters R_{clus} and P_{clus} can give a good description of spallation reactions. We plan to vary the spatial distance between nucleons from minimum to maximum under fixed momentum constraints. We also try to vary the momentum constraints by fixing the spatial distance, and compare both correlations with the experimental data of ALADIN [42, 220] and NSCL [53].

6.5 Results and Discussion

We present the analysis for different system size effects, excitation energies and colliding geometries. We study the multifragmentation using a soft equation of state along with enhanced and reduced clusterization range (R_{clus}) and momentum constraints (P_{clus}) with an isospin-dependent reduced cross-section ($\sigma = 0.9\sigma_{NN}$)[81]. A study with in-medium cross-sections [223-225] has been reported in the literature. For our study, the reactions of $^{40}Ar_{18} + {}^{45}Sc_{21}$ ($\hat{b} = 0.4$, L=0.5L), where L=8.66 fm^2 $^{86}Kr_{36} + {}^{93}Nb_{41}$ ($\hat{b} = 0.4$, L=0.6L), $^{64}Zn_{30} + {}^{58}Ni_{28}$ (b=2 fm, L=0.6L), $^{129}Xe_{54} + {}^{139}La_{57}$ (b=0-3 fm, L=0.7L), $^{139}La_{57} + {}^{139}La_{57}$ ($\hat{b} = 0.3$, L=0.8L), and $^{197}Au_{79} + {}^{197}Au_{79}$ (b=2.5 fm, L=L) are simulated. The choice of impact parameter is guided by experimentally extracted information [141-144, 163, 171-174]. The above reactions were simulated between 35 and 200 MeV/nucleon. The reaction dynamics are followed until 200 fm/c and then clusterization is performed with the MST method. We attempted to fit the experimental findings with $P_{clus} = 240$ MeV/c and $R_{clus} = 4$ fm in the presence of a soft equation of state.

6.5.1 Phase space of nucleons

We display in Figs.6.2, 6.3, 6.4, and 6.5 the phase space of nucleons for X-Z, Y-Z and $P_x - P_z$, $P_y - P_z$ plane for the reaction of $^{197}Au_{79} + {}^{197}Au_{79}$ at central (b=0 fm) and peripheral (b=7.8 fm) geometry. The panels from top to bottom are representing the position of nucleons of projectile and target at different times at incident energy of 100 MeV/nucleon. During and after overlapping (above t=30 fm/c) more repulsion is observed in the projectile as well as target nucleons in all planes. More radial expansion of the matter is observed for central collisions. This is due to the fact that more is the repulsion, more is the squeeze-out of the particles and more is the transfer of the momentum in the radial directions. But for peripheral collisions less squeeze out of particles is observed. In central collision for Au+Au, we found that 33% of LMFs and 17% of IMFs contains the particles from surface and remaining are coming from the core of colliding nuclei. Observations are also made for the peripheral collisions in which 21% of LMFs and 20% of IMFs contains the particles from surface and remaining are coming from the core of colliding nuclei. From this, we conclude that more particles coming from the surface of colliding nuclei if the collision are central. But in peripheral collisions more particles are coming from the core of colliding nuclei.

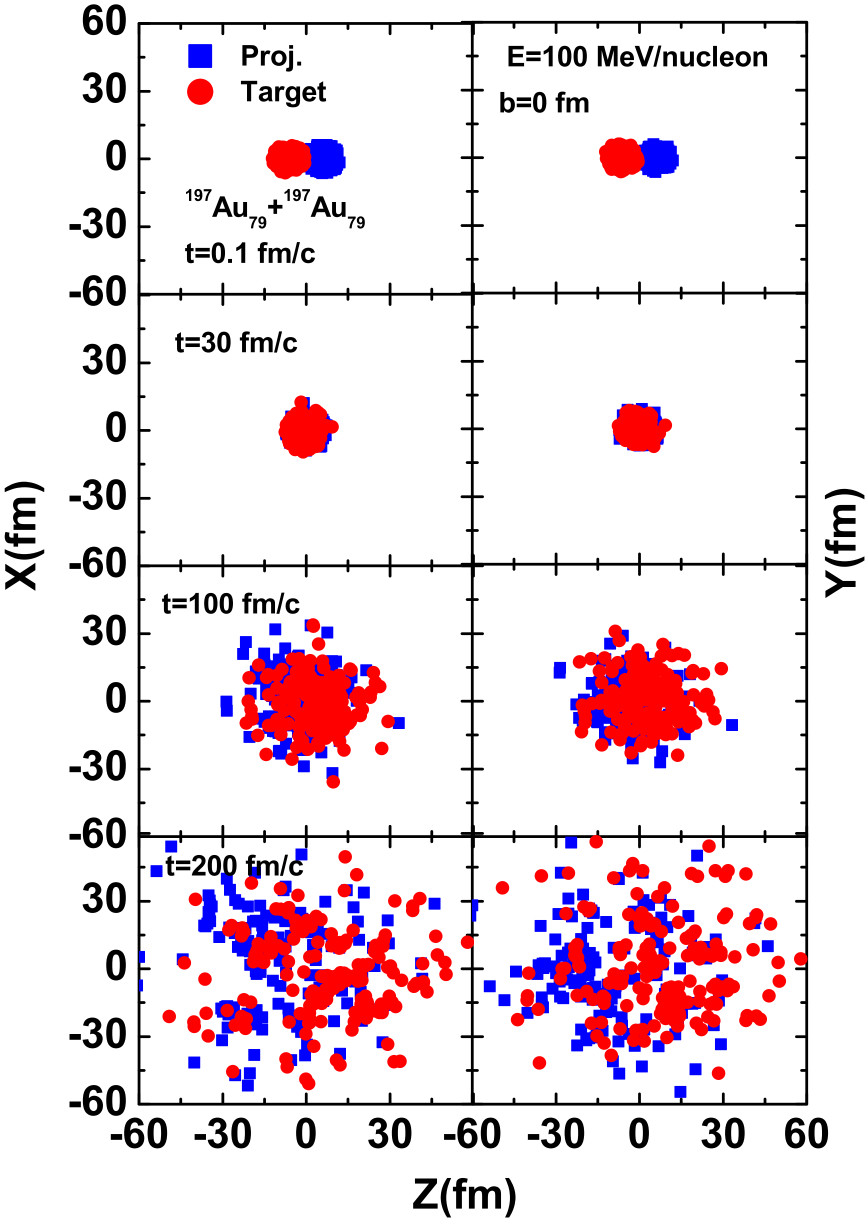

Figure 6.2: Phase space distribution of the projectile and target nucleons in the X-Z and Y-Z plane for Au+Au at incident energy of 100 MeV/nucleon and for b=0 fm. The panels from the top to bottom are representing the positions at different times.

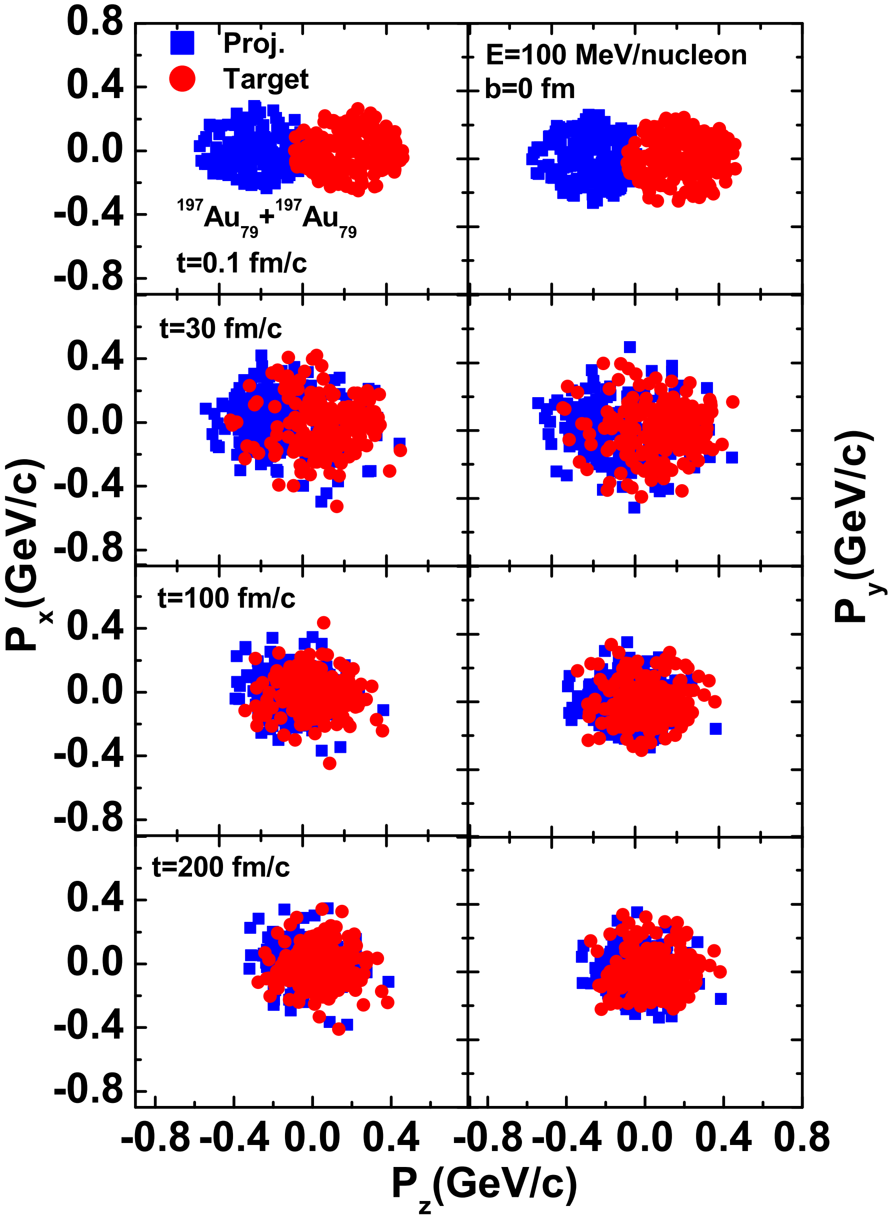

Figure 6.3: Same as in Fig. 6.2 but for $P_x - P_z$, $P_y - P_z$ plane.

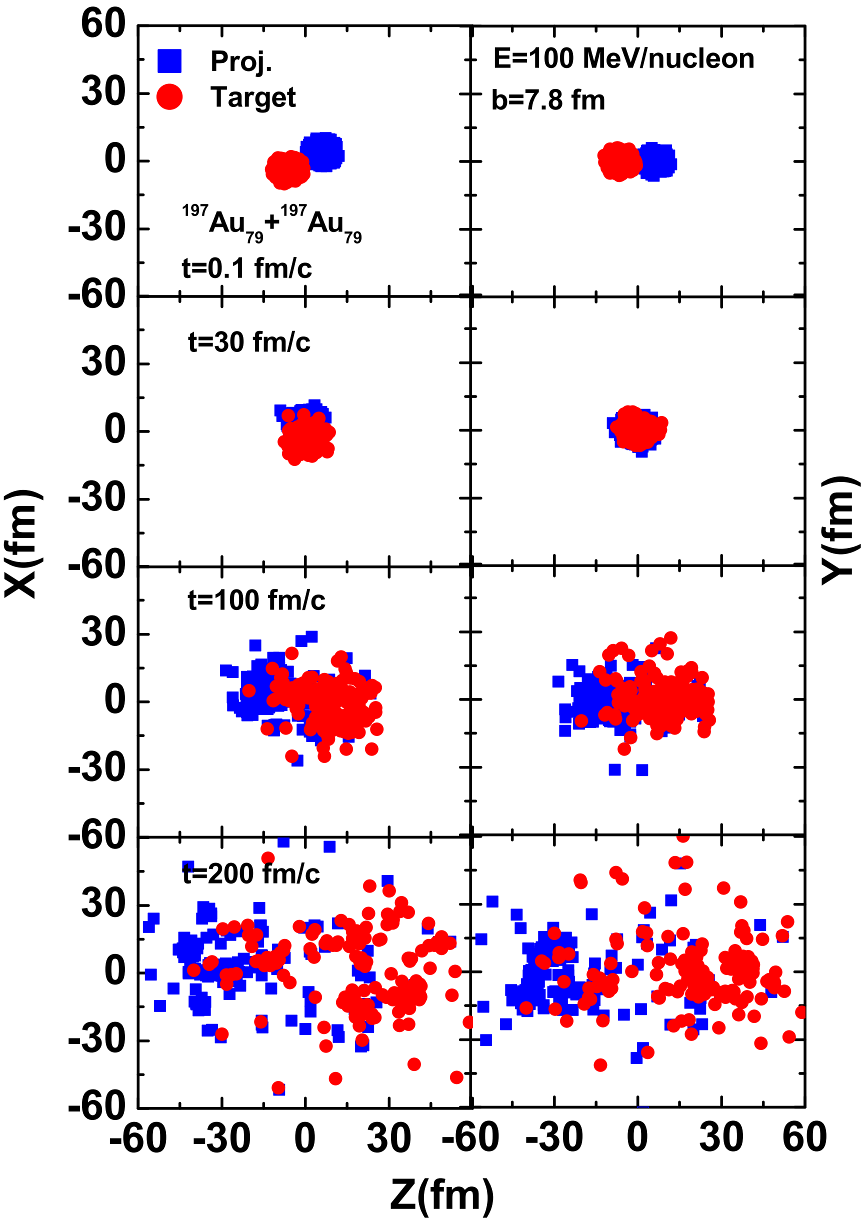

Figure 6.4: Phase space of nucleons in the X-Z and Y-Z at b=7.8 fm.

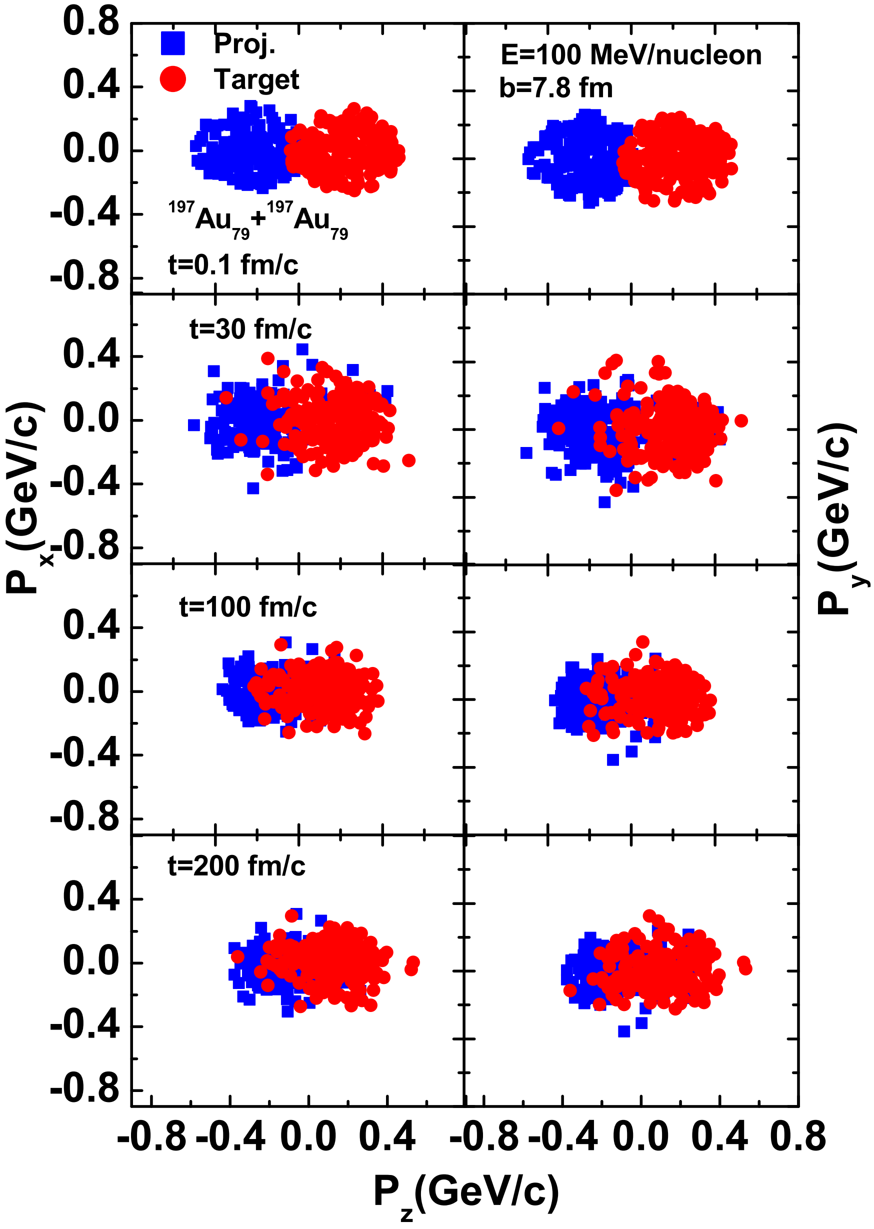

Figure 6.5: Same as in Fig. 6.3 but for $P_x - P_z$, $P_y - P_z$ plane.

6.5.2 Variation of multiplicity of various fragments for different values of R_{clus} and P_{clus}

The MST method decide the fate of a fragment based on their spatial distance (R_{clus}), whereas the MSTP method will also take care of their momentum correlations (P_{clus}). In the Figs.6.6 and 6.7, we vary the value of P_{clus} from 130-300 MeV/c and R_{clus} from 2-8 fm at some fixed values of R_{clus} and P_{clus} respectively. Multiplicity of various fragments saturates for $P_{clus} = 240$ MeV/c and $R_{clus} = 4$ fm for various systems at incident energies of 150 and 200 MeV/nucleon.

In Fig.6.6, we display the variation of multiplicity of various fragments for different values of P_{clus} at fixed $R_{clus} = 4$ fm for different systems at incident energy of 150 and 200 MeV/nucleon. Low energy decreases the emission of free nucleons and light mass fragments but increases the emission of the heavy mass and intermediate mass fragments and *vice-versa*. Fragments formed at 200 fm/c (typical saturation time) were used for the present analysis. The production of various fragments heaviest fragment (A_{max}), free nucleons (FNs), light mass fragments (LMFs) and intermediate mass fragments (IMFs) depends upon the P_{clus} between the nucleons. When P_{clus} is small, the maximum number of FNs are produced. As we increase P_{clus}, the repulsive nature of momentum-dependent interactions dominates, and so decreases the production of FNs and LMFs while increasing the production of intermediate and heavy-mass fragments. As the size of nuclei increases, production of various fragments increase. At $P_{clus} = 240$ MeV/c there is no further change in the production of various fragments.

In Fig.6.7, we display the variation of multiplicity of various fragments for different values of R_{clus} with fixed momentum constraints, for different systems at incident energy 150 and 200 MeV/nucleon. In this figure, we show that, the production of various fragments depends on the distance between two nucleons. When distance is small, large numbers of FNs and LMFs are produced and very few IMFs can be seen. As the distance increases, however, emitted nucleons and LMFs are reduced and the number of IMFs increases. The number of light particles increases with increase in energy, but the number of heavy-mass fragments decreases consistently. The multiplicity of various fragments also depends on the size of nuclei, which increases with increase in system mass. Curves of different colliding nuclei show maxima at $R_{clus} = 4$ fm. Multiplicity continuously decreases for FNs and LMFs and increases for heavy mass and IMFs from this point. Now, we are interested to know the clusterization range between the nucleons at different values of P_{clus}.

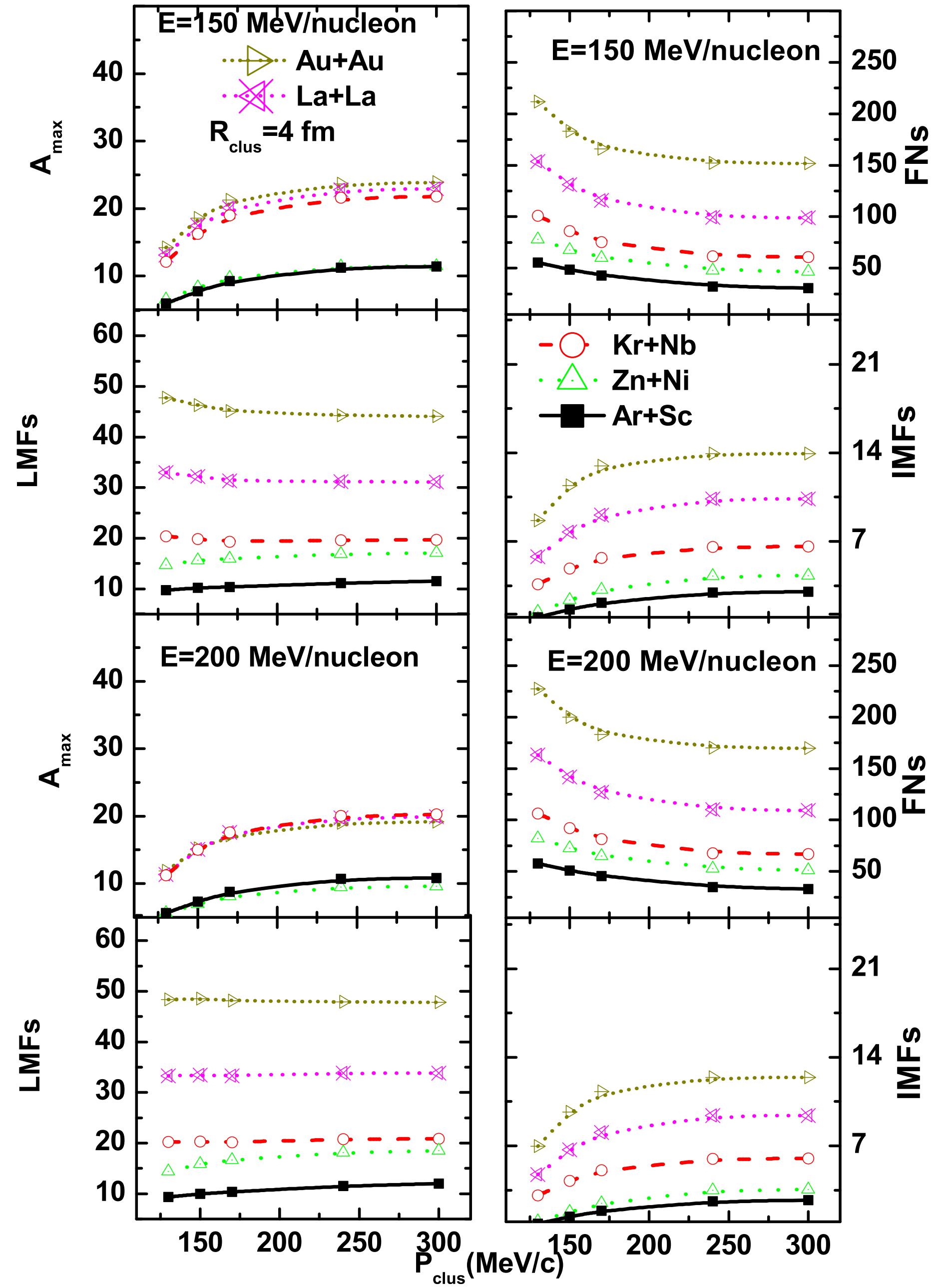

Figure 6.6: The A_{max}, FNs, LMFs and IMFs as a function of P_{clus} for different systems at an energy of 150 and 200 MeV/nucleon.

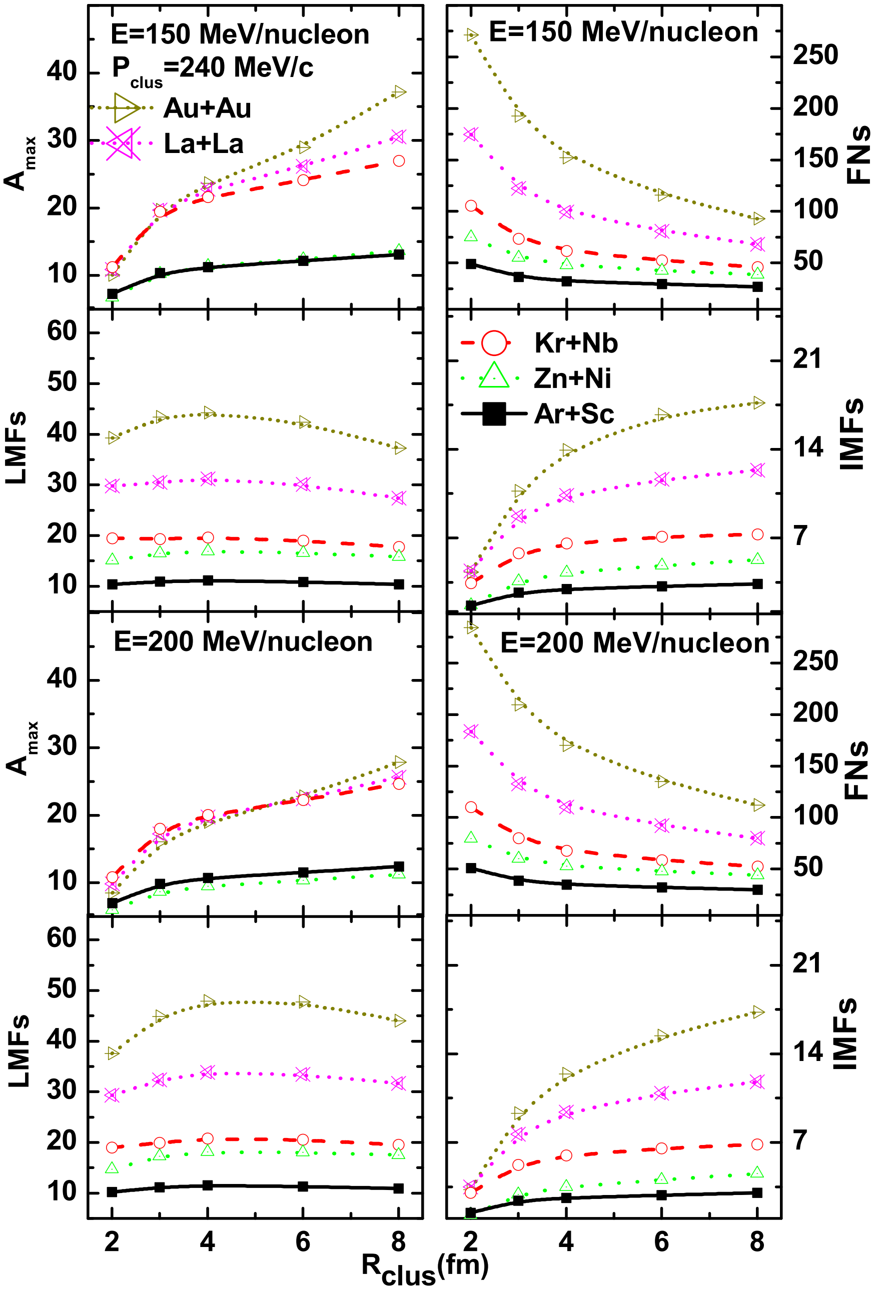

Figure 6.7: Same as in Fig. 6.6, but for the multiplicities of various fragments as a function of R_{clus}.

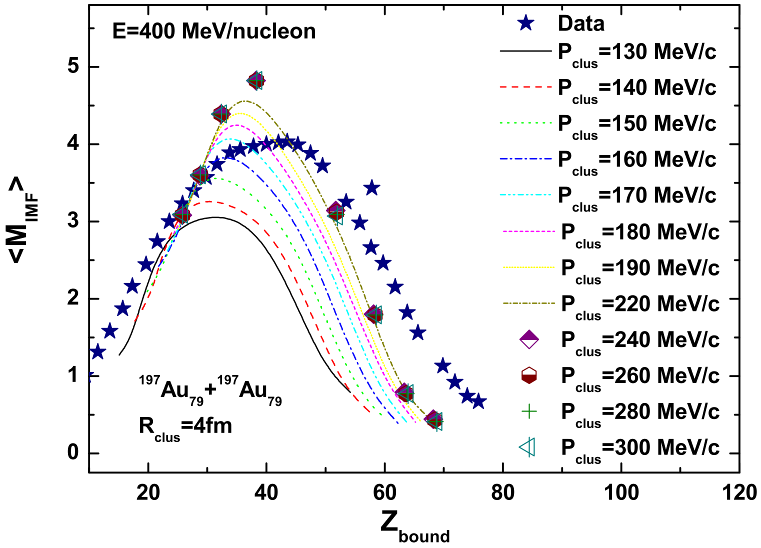

Figure 6.8: Mean multiplicity of the intermediate mass fragments $\langle M_{IMF} \rangle$ as a function of Z_{bound} for the reaction of $^{197}Au_{79}$ on $^{197}Au_{79}$ at E/A=400 MeV. Various values of P_{clus} and comparisons with the data are shown [42, 219, 220].

6.5.3 Multiplicity of IMFs as a function of Z_{bound}

In Fig.6.8, we display the multiplicity of IMFs as a function of Z_{bound} for the reaction of $^{197}Au_{79} +^{197} Au_{79}$ at incident energy of 400 MeV/nucleon. Z_{bound} is defined as the sum of the atomic numbers Z_i of all fragments with $Z_i \geq 2$. The global universality of the rise and fall behavior is preserved [42, 219, 220]. This is evident from the fact that small value of the Z_{bound} correspond to high excitation energies of the sources that disintegrate predominantly into very light clusters (fall of multifragmentation). Large values of Z_{bound} correspond to low excitation energies, at which the decay changes its character from evaporation-like or fission-like processes to multifragmentation (rise of multifragmentation). At very large value of Z_{bound} i.e. in peripheral collisions where only a small amount of incident energy is transferred to the projectile. Peripheral collisions between two nuclei may also lead to a spallation process in which only a single heavy fragment is produced so there is a fall in fragment production. In other words, the maximum number of IMFs can only be seen at semi-central impact parameters. For energy 400 MeV/nucleon, central collisions generate better repulsion and break the colliding nuclei into FNs, LMFs; for peripheral collisions the energy transfer from the participating matter to spectator matter is minimal and therefore

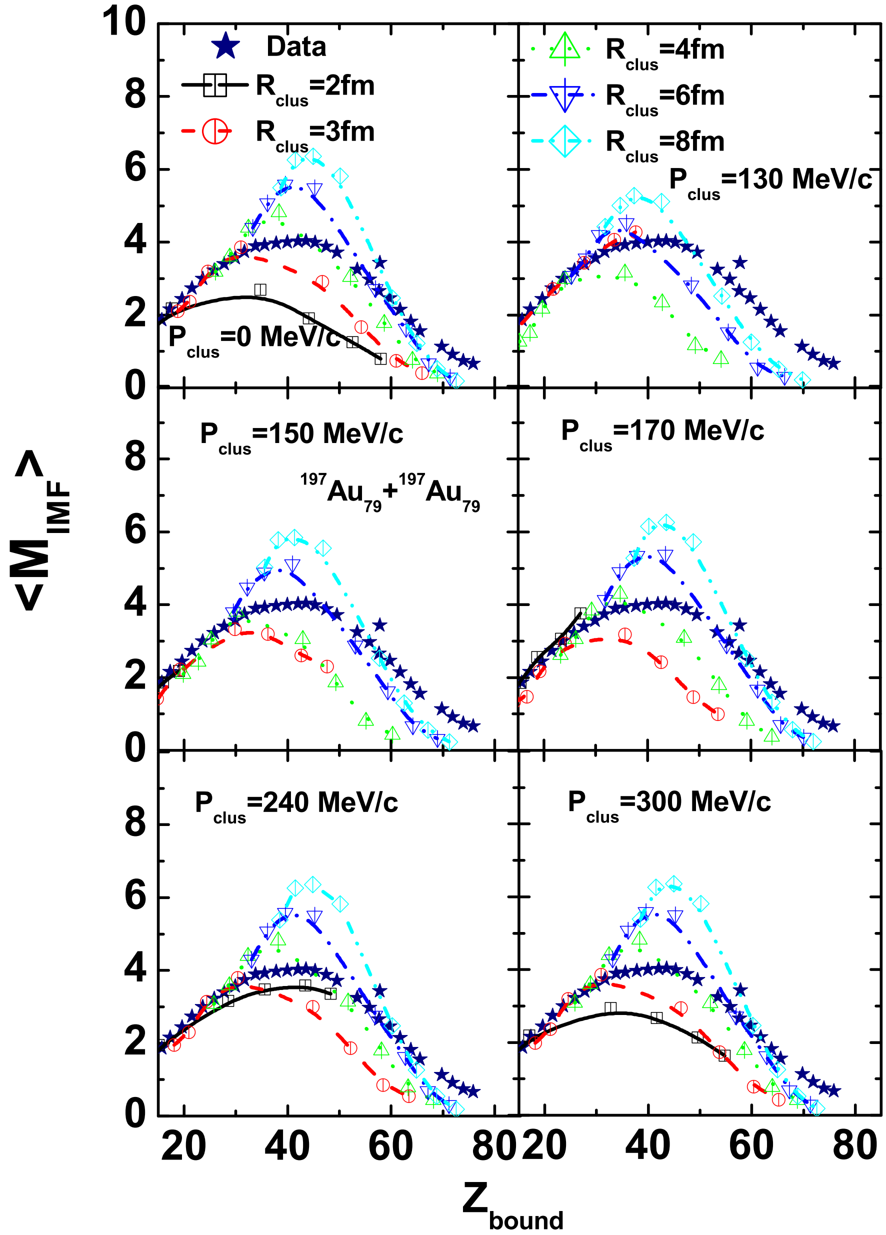

Figure 6.9: Mean multiplicity of IMFs as a function of Z_{bound} for different values of R_{clus} at some fixed values of P_{clus} for Au+Au system. Experimental data are the same as in Fig.6.8.

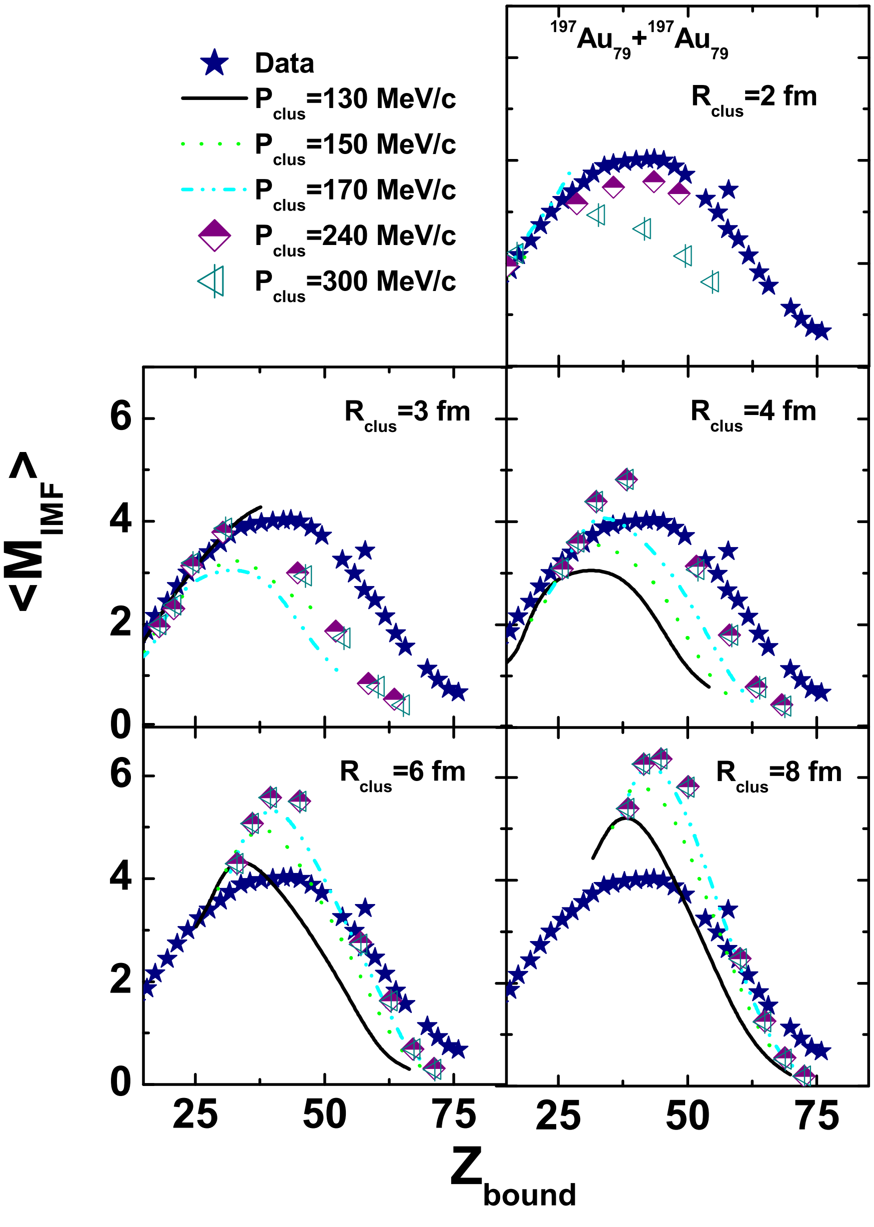

Figure 6.10: Multiplicity of intermediate mass fragments $\langle M_{IMF} \rangle$ as a function of Z_{bound} for different values of P_{clus} at some fixed values of R_{clus}. Experimental data are the same as in Fig.6.8.

very few IMFs are seen. At $Z_{bound} \approx 40$ the mean multiplicity $\langle M_{IMF} \rangle$ reaches its maximum of 4 to 4.5. As we increase the value of the momentum constraint, production of FNs and LMFs is reduced, and there is a rise in the production of IMFs. We observe no further increase in $\langle M_{IMF} \rangle$ after $P_{clus} = 240$ MeV/c. After this as we increase P_{clus}, the multiplicity of IMFs $\langle M_{IMF} \rangle$ remains same. In Fig.6.9, we show that when the momentum cut is not applied, the lowest value of R_{clus} produces minimal number of IMFs, while the highest R_{clus} results in the maximum number of IMFs. When the momentum cut increases from 130-300 MeV/c the number of intermediate mass fragments also increases. We find a strong effect of the cut (in the relative momentum of nucleons) on the fragment multiplicity in the central collisions, whereas the effect is smallest for peripheral collisions. The idea of imposing a cut in momentum space is to avoid the creation of fragments which are not properly bound and will either decay after a while or will emit nucleons in the course of time. For low values of the momentum cut interactions are attractive, therefore no IMFs are produced when the distance between two nucleons is 2 fm, but IMFs are produced for nucleons in which the separation is more than 3 fm. For the higher values of momentum cut (i.e. for P_{clus} is equal to 240 and 300 MeV/c), when we vary the distance between the nucleons from 2 to 4 fm, we observe that same number of IMFs are produced for $R_{clus} = 4$ fm, for these higher value of momentum cut. $R_{clus} = 4$ fm at $P_{clus} = 240$ MeV/c best explains the data and this remains so even if we increase P_{clus} to 300 MeV/c. As we want to optimize the distance between two nucleons, in Fig.6.10, we plot the multiplicity of IMFs as a function of Z_{bound}. This figure show different values of the momentum cut. For central colliding geometry, with the lowest value of the clusterization parameter $R_{clus} = 2$ and 3 fm, a large energy transfer to spectator part corresponds to a smaller value of Z_{bound}. If the clusterization parameter is too large, a very small energy transfer to spectator part corresponds to larger value of Z_{bound}. Low values of the R_{clus} parameter show negligible fragments for low values of P_{clus}, but, as we increase P_{clus} more IMFs are predicted. For $R_{clus} = 4$ fm there is a systematic trend for different value of P_{clus} compared to other clusterization parameters. In this clusterization range there is no change in production of $\langle M_{IMF} \rangle$ above $P_{clus} = 240$ MeV/c.

6.5.4 Time evolution of multiplicity of various fragments

In Fig.6.11, we show the time evolution of the A_{max}, FNs, LMFs and IMFs at the balance energy and high energies of the systems. At balance energies A_{max} gives just a single

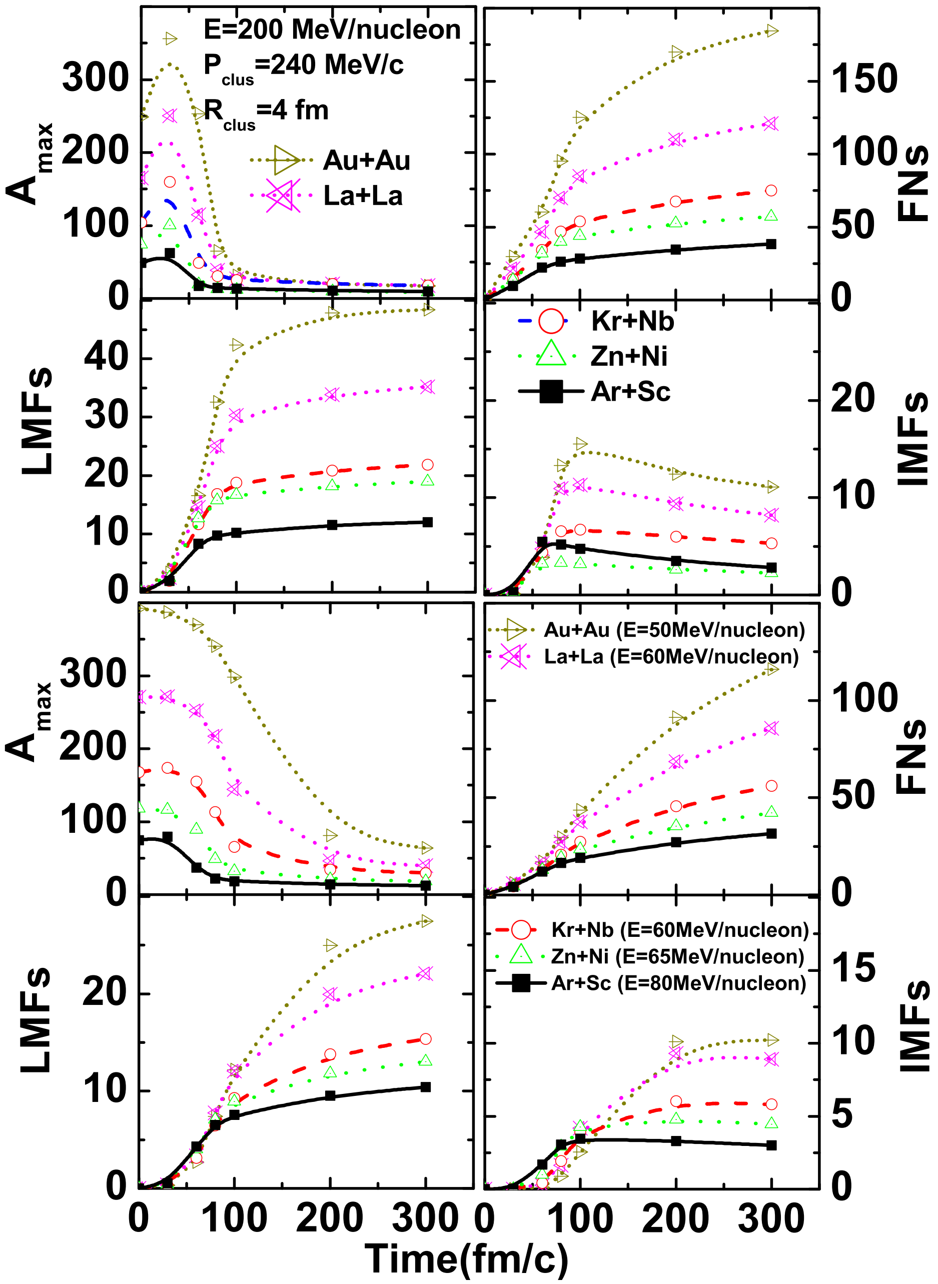

Figure 6.11: The time evolution of the multiplicity of various fragments for different systems. The upper panel shows energy equal to 200 MeV/nucl. while the lower panel denotes the results obtained with the balance energy of the systems.

fragment with 394 nucleons contained in it. This results in the decrease in emission of FNs, LMFs and IMFs at the start of collisions. But as the time increases emission of FNs, LMFs and IMFs increases with subsequent decrease in the emission of A_{max}. At higher energies emission of A_{max} decrease as two nuclei collide with each other results in subsequent increase in emission of FNs, LMFs and IMFs for fixed R_{clus} and P_{clus}. At higher beam energy of 200 MeV/nucleon it takes lesser time until the finite distribution is obtained. This is due to the large energy transfer from participant to spectator matter that is consequently excited, and hence the emission time scale is too short. At balance energies, it takes larger time until the finite distribution is obtained. This is due to the small energy transfer from participant to spectator matter that is consequently less excited, and hence the emission time scale is very long. Nearly no IMFs are produced upto 50 fm/c at balance energies.

Here a typical time 200 fm/c is needed to pin down the contents of various fragments. Multiplicity of FNs, LMFs, IMFs, and A_{max} increases with an increase in system mass. The A_{max} lasts longer in heavier systems compared to the lighter systems. The excited A_{max} in heavier systems continues to emit the nucleons till the end of the reaction, whereas it saturates around 100 fm/c in light systems indicating the cold and separated matter for balance energies. Due to finite collision rate in heavier colliding nuclei, the emission of the nucleons and light charged particles continues till the end of reaction. The saturation of the FNs and LMFs and IMFs occurs earlier at higher incident energies, which indicates a faster disintegration of the matter at these energies. If one plots the final state multiplicity of the IMFs as a function of the Z_{bound}, one will observe the well known rise and fall when energy is 200 MeV/nucleon, whereas no such behavior is found around balance energies.

6.5.5 Incident energy dependence of multiplicity of fragments

The effect of different energies on the fragmentation pattern is presented in Fig.6.12. The collision of different nuclei at incident energy ranging from 35 to 200 MeV/nucleon is simulated for reduced isospin-dependent cross-section at $P_{clus} = 240$ MeV/c and $R_{clus} = 4$ fm. Here, we display the multiplicity of various fragments as a function of energy. As the energy increases i.e. for central collisions or we can say for smaller impact parameter, collisions will become more violent, creating compression zones and decreasing the Pauli blocking effect so more clusters fall into the range of light-mass fragments. At very low energy i.e. higher value of impact parameter or for peripheral collisions complete destruction does not take place, hence there is only an increase in the production of A_{max}. At very high energy,

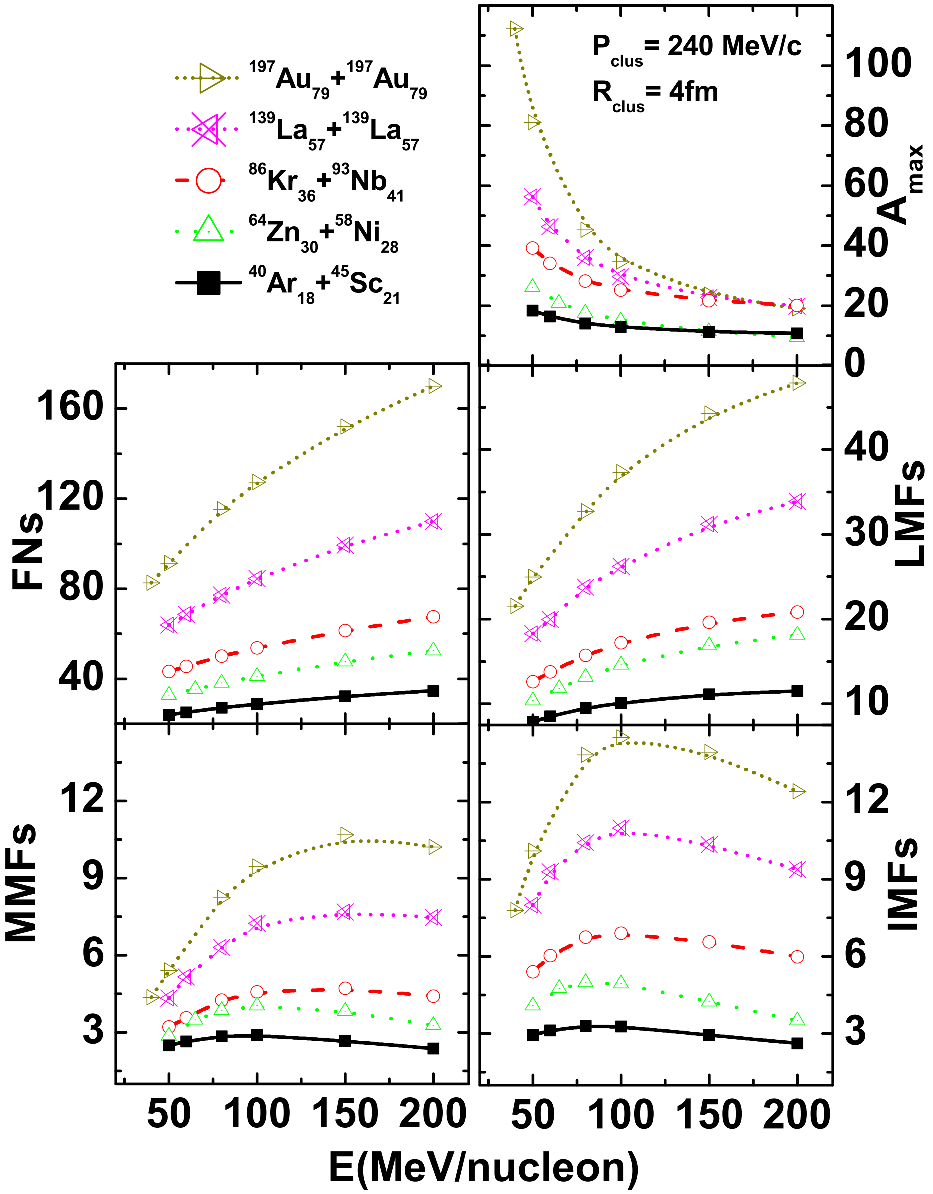

Figure 6.12: Multiplicity of various fragments as a function of incident beam energy for different systems.

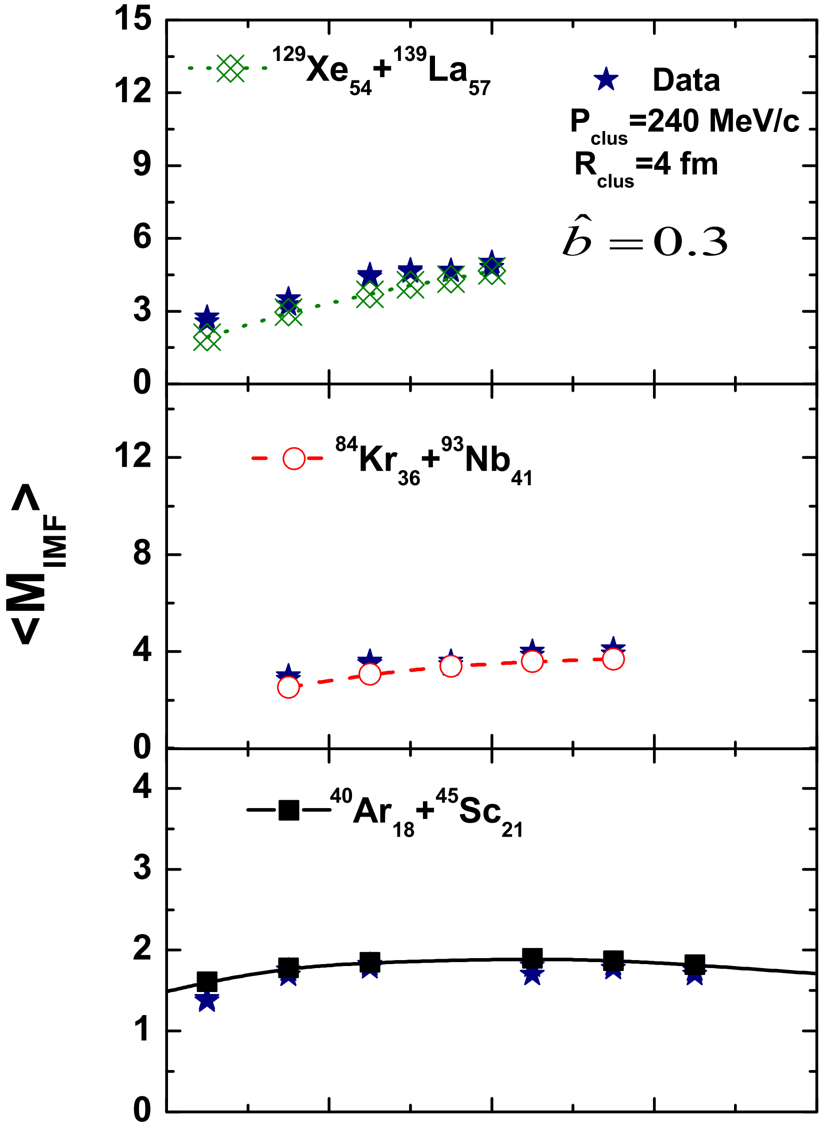

Figure 6.13: The average multiplicity of IMFs as a function of beam energy for the reactions of Xe+La, Kr+Nb, Ar+Sc. The star symbol represents NSCL experimental results [188]. Lines indicate theoretical results obtained for $P_{clus} = 240$ MeV/c and $R_{clus} = 4$ fm.

however, complete destruction take place, hence there is a decrease in the production of A_{max} and IMFs accompanied by an increase in the production of FNs, LMFs.

In other words at low incident energies, the excitation energy available to the system is very small. Therefore, a larger impact of collisions is needed to break the system into pieces of different sizes. At higher incident energies, excitation energy deposited in the system is very large. Therefore, central collisions break matter into much smaller pieces and rarely one sees intermediate mass fragments or heavy-mass fragments in these events. Also with an increase in the size of the system, multiplicity of fragments also increases as shown in the figure.

In Fig.6.13, asymmetric reactions of $^{131}Xe_{54}$ + $^{139}La_{57}$, $^{84}Kr_{36}$ + $^{93}Nb_{41}$, $^{40}Ar_{18}$ + $^{45}Sc_{21}$ are displayed as a function of the beam energy at scaled impact parameter $\hat{b} = 0.3$ (semicentral collisions) using ($\sigma = 0.9\sigma_{NN}$) for $P_{clus} = 240$ MeV/c and $R_{clus} = 4$ fm. Final state results are also compared with the NSCL experimental data [188]. We see that our results are in good agreement with the experimental data. For heavier systems like Kr+Nb and Xe+La, multiplicity of IMFs increases with an increase in beam energy but for Ar+Sc, $\langle M_{IMF} \rangle$ slightly decreases with increased beam energy. For lower energies, we see dominated role of mean field and hence increase in the intermediate mass fragments. For heavier systems, at these energies there are less collisions and hence increase in emission of IMFs whereas at very high energies multiplicity of IMFs decreases. One should note that in the first two reactions, incident energy is much less compared to the last reaction.

6.6 Summary

In the present chapter, we have carried out a detailed analysis of the role of spatial and momentum constraints on fragmentation using an IQMD model. We compared our theoretical results with the experimental data of ALADIN, study the variation of multiplicity of intermediate mass fragments with impact parameter and predict rise and fall behavior of multifragmentation. We observe that spatial distance of 4 fm with a realistic value of cut (240 MeV/c) are in agreement with experimental data. We also compared our theoretical results with the experimental data of NSCL, study the variation of multiplicity of intermediate mass fragments with incident beam energy for different systems. We find spatial distance of 4 fm with a momentum cut (240 MeV/c) are in good agreement with experimental data of NSCL. Several different system sizes and physical pictures were considered for deeper understanding. We studied the role of momentum cuts and spatial correlations (i.e., the range of clusterization) in fragment formation. The time evolution of nucleons was followed using an IQMD model. Two nucleons were deemed to be in the same fragment if their centroids were less than 4 fm, which is a condition of the MST method.

Our analysis indicated that the effect of a cut in the momentum space on fragment formation is stronger if the cut in the relative momenta of two nucleons is 240 MeV/c. For higher values of the cut production remains the same. We further found that the spatial distance of 4 fm with a realistic value of cut (240 MeV/c) was important in order to get the most bound structure of fragments in the central collisions. For a given set of input parameters, we found that the spatial correlation and momentum constraints had a sizable effect on fragmentation.

Chapter 7

Effect of Gaussian width on nuclear flow and multifragmentation

7.1 Introduction

The formation of fragments (and their size) needs a correct understanding of the nucleon-nucleon correlations and interactions among them which differs in different physical conditions depending on the system size and excitation energy available to nucleons. In the previous study, the longer interaction range in the semiclassical model, namely quantum molecular dynamics (QMD) is reported to give much fewer fragments than detected in experiments [5, 83, 84, 110, 137, 138, 226]. The width of the Gaussian distribution of nucleon determines the interaction range of the particles and influences the density distribution of finite systems. The equation of state for finite nuclear matter depends strongly on the value of Gaussian width chosen and different widths affects the fragmentation by 30-50% [30, 74]. For (homogeneous) infinite nuclear matter the density (and thus the potential energy) do not depend anymore on the extension of the Gaussian wavepackets. Thus, the equation of state of infinite nuclear matter is independent of Gaussian width L. In finite matter E/A also depends on L. Thus even two parametrization which yield the same EOS may produce different results for the reaction of two heavy ions. Therefore, we have to adjust L to have reasonable surface properties. In order to allow a physical interpretation L should be of the order of the size one expects for the range of the nuclear interaction. There exist a range of values for L, which allows to fix these properties. Larger values of L increase the effective range of interaction and thus leads to some smearing of fluctuations, which are stronger for more located wavepacket (small values of L).

The wave-packet width in AMD (antisymmetrized molecular dynamics), FMD (fermionic molecular dynamics) [120, 123, 227] and EQMD (extended quantum molecular dynamics) [228] models is dynamic because fermionic nature of the system is preserved, and in the

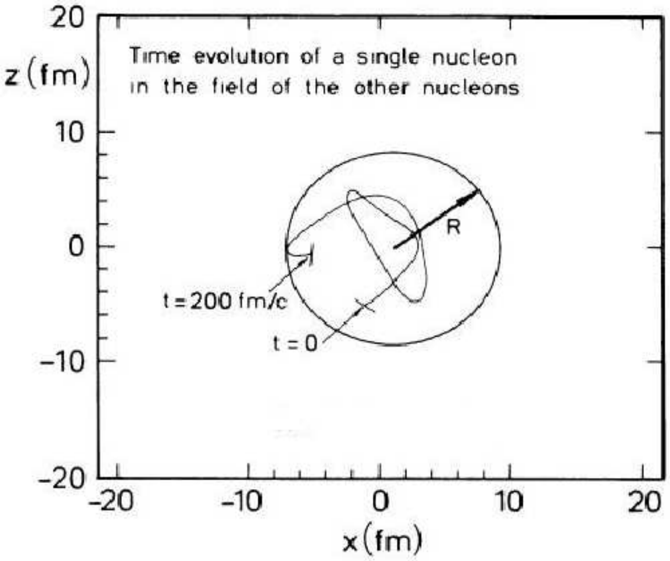

Figure 7.1: The trajectory of a single nucleon in the field of gold nucleus is displayed in the figure [20].

normal QMD model [5, 83, 84] it is constant and it lack the fermionic nature. But the value of width in the QMD calculations are quite different. For example, in Ref. [30] the Gaussian width was taken as L=4.33 fm^2 for reaction Ca+Ca and L=8.66 fm^2 for Au+Au. In Ref. [229] the authors took two different values of the width of the Gaussian wave packet for multifragmentation and fusion reaction in order to have reasonable results. Therefore, it seems to us that it is worth to conduct a further study of the influence of Gaussian width on the ground state properties of individual nuclei as shown in Fig.7.1 and the Coulomb barrier in fusion reactions. In isospin-QMD (IQMD) model the centroids of the nucleus are randomly distributed in a phase space sphere ($r \leq R$ and $p \leq p_f$) with $R = 1.12A^{1/3}$ fm corresponding to a ground state density of $\rho_0 = 0.17$ fm^{-3}. The Fermi momentum p_f depends on the ground state density. For $\rho_0 = 0.17$ fm^{-3} it has a value of about $p_f \approx 268$ MeV/c. As it has already been stated, the Gaussian width can be regarded as a description of the interaction range of a particle. Its influence disappears for infinite nuclear matter whereas for finite systems it may play a non negligible role. In IQMD the Gaussian width can be used as an optional input parameter. The system dependence of L in IQMD has been introduced in order to obtain maximum stability of the nucleonic density profiles. So, for this study we propose a system size dependent wave packet width.

The emission of neutrons in the fragmentation of excited Sn and La projectiles has been studied with the Large Neutron Detector LAND positioned forward of the ALADIN spectrometer at the SIS accelerator(GSI) [220, 230, 231]. The isotropy of the fragment emission in the decaying spectator rest-frame suggests an emission from a thermodynamical equilibrated source. In these collisions, energy deposition are reached which cover the range from particle evaporation to multifragment emission and further to total disassembly of the system, the so-called rise and fall of the fragment emission [43, 213]. The apparent absence of dynamical dependencies is the most prominent feature of the multifragmentation decay of excited spectator nuclei. The fragmentation patterns in $^{197}Au_{79}$ on $^{197}Au_{79}$ collision at beam energy E=600 MeV/nucleon is studied using the ALADIN spectrometer. They shows the correlation between the mean multiplicity of intermediate mass fragments $\langle M_{IMF} \rangle$ and Z_{bound} for the four bombarding energies [7, 42, 221].

As stated in the previous chapter, experimentalist studied the multiplicity of IMFs as a function of Z_{bound} and reported a rise and fall in production of IMFs with increase in the value of Z_{bound}. These findings pose a stringent test for any theoretical model designed for the study of multifragmentation.

In recent years much emphasis has been placed on the study of collective flow and several groups have performed experiments to study its disappearance [186, 232-236]. The disappearance of the collective flow is predicted to occur at an incident energy (termed the balance energy, E_{bal} [146, 147, 186, 232-236]) corresponding to the point where the attractive scattering balances the repulsive interactions [58, 146, 147, 186, 232-240]. Attractive scattering corresponds to negative scattering angles which can be related to partial orbiting of two nuclei. Repulsive scattering corresponds to positive scattering angle which can be visualized as the two nuclei bouncing off each other. The present measurements were carried out with the Michigan State University 4π Array [53] at the National Superconducting Cyclotron Laboratory (NSCL) using beams from the K1200 cyclotron.

Both multifragmentation and collective flow measured /predicted in heavy-ion collisions has been reported to be highly sensitive towards the several model ingredients such as size of the system, colliding geometry (i.e. the impact parameter), and the incident energy of projectile and also on the interaction range of particles. But there is no systematic study in the literature for optimization of Gaussian width for different nuclei using IQMD model. Our present study is carried out within the framework of isospin dependent quantum molecular dynamic model (IQMD).

7.2 Scaled Gaussian width

To analyze the result, we want to optimize the scaled Gaussian width (SGW) for different colliding nuclei. **Scaled Gaussian width (SGW) can be defined as the ratio of the Gaussian width used for any nuclei to the Gaussian width used for Au nuclei(i.e. 8.66 fm^2).** By doing so, correct mass dependence of the Gaussian width can be formulated. It is worth mentioning that the appropriate choice of the Gaussian width of the nucleonic wave packet is very important as it affects the collective flow and also the energy of the vanishing flow (EVF) and other phenomena in heavy-ion collisions. In the present study, we noted the range of the SGW from the time evolution of the largest fragment and see its effect on the balance energy. We also compared our theoretical results with experimental data of ALADIN [220, 230, 231] and NSCL [53].

7.3 Results and Discussion

Here, we simulate for different system size effect, excitation energy, colliding geometry and SGW using isospin-dependent reduced cross-section ($\sigma = 0.9\sigma_{NN}$) studied in ref. [81] and soft equation of state. If a system is in the ground state, the phase space is densely filled up to minimum value in the co-ordinate and momentum space. It is this property of the ground state which we employ to initialize the nucleus. In this chapter, we want to check the stability of a nucleus by initializing the nucleus at its ground state energy. The reactions were followed till 200 fm/c i.e. saturation time. The Gaussian width used in the literature for Au nuclei 8.66 fm^2 and for Ca it is 4.33 fm^2 [30]. But no systematic study is given in literature, in which Gaussian width show stability for all colliding nuclei in IQMD model.

7.3.1 Time evolution of radius and largest fragment for different nuclei

In Fig.7.2, we display the time evolution of the root mean square radius of a cold nucleus. In this figure, we check the stability for two nuclei one is lighter i.e. Ca and other is heavier i.e. Au. Then we change the scaled Gaussian width (SGW) by reducing and enhancing SGW from its normal value. From the figure, we see that $^{197}Au_{79}$ show maximum stability for 1.6 (SGW) and for $^{40}Ca_{20}$ maximum stability is at 0.7 (SGW). The reason for the stability for these Gaussian width is that these curves are closer to actual radius of $^{197}Au_{79}$ and $^{40}Ca_{20}$ respectively. For the heavy nuclei, we see oscillations around mean value, but no nucleons are emitted. So, light nuclei are little less stable compared to heavy one. One

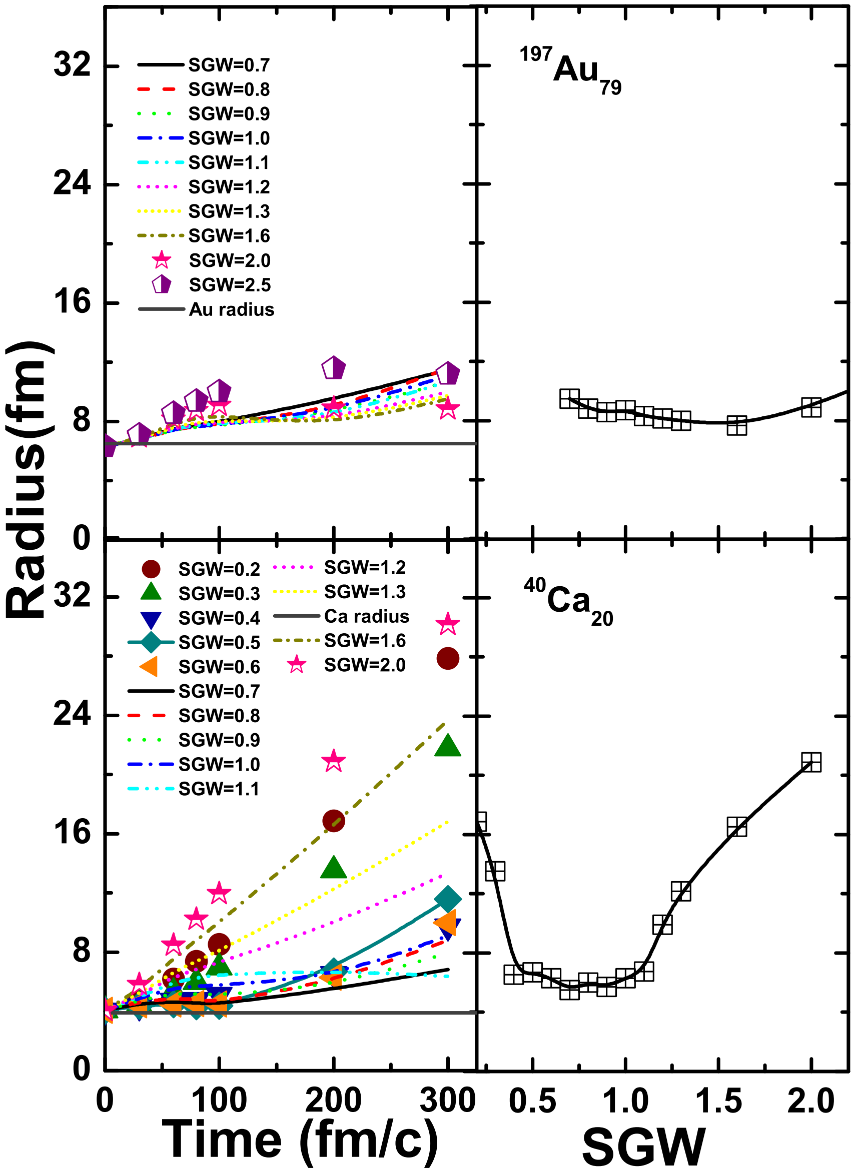

Figure 7.2: The root mean square radii of Ca and Au as a function of time (left panel) for different scaled Gaussian width (SGW). Right panel shows radius as a function of SGW at saturation time.

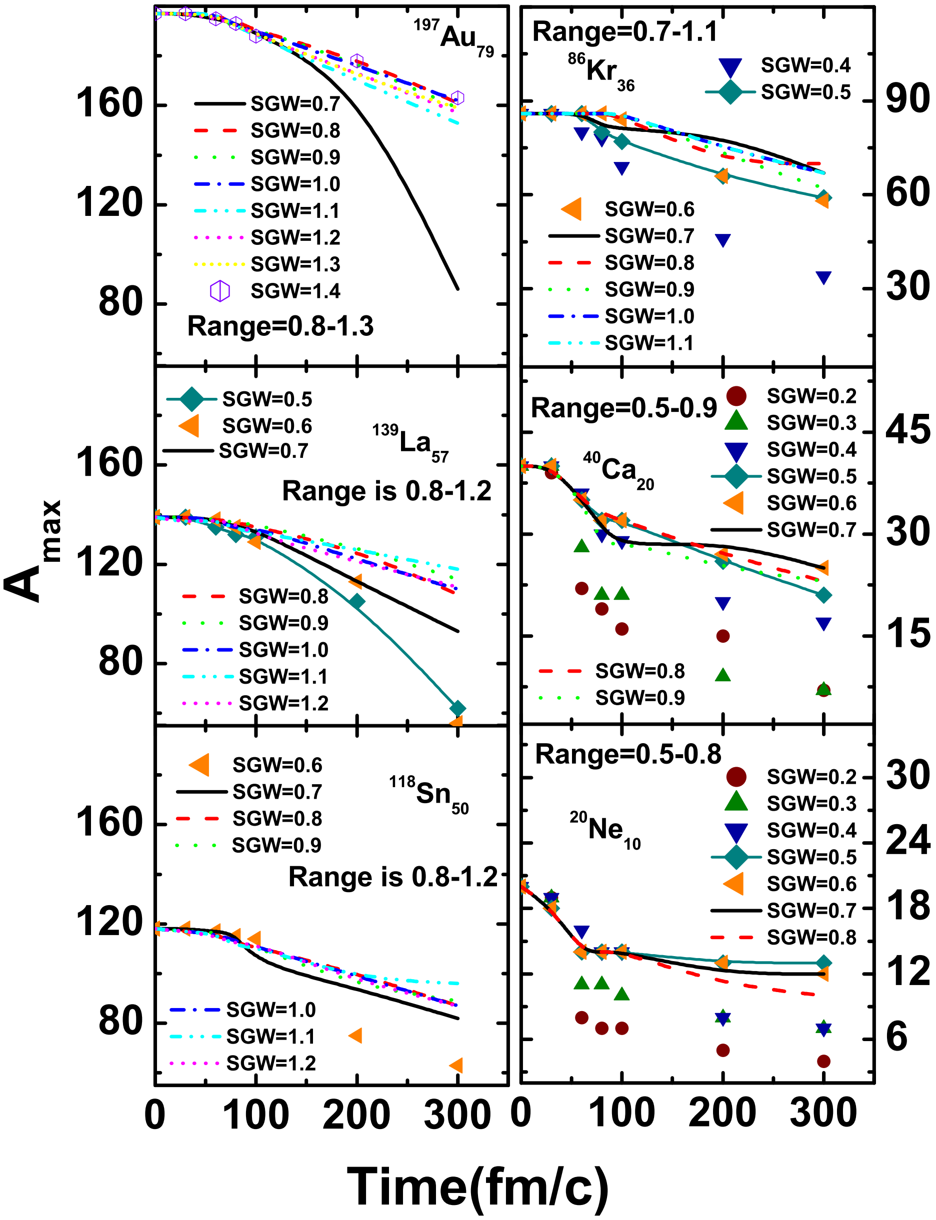

Figure 7.3: Time evolution of largest fragment for different nuclei $^{197}Au_{79}$, $^{139}La_{57}$, $^{118}Sn_{50}$, $^{86}Kr_{36}$, $^{40}Ca_{20}$, $^{20}Ne_{10}$ at their ground state.

or two nucleons are emitted in the time span of 200 fm/c. This happens due to the local density approximation which is not very good for the lighter nuclei [5, 83, 84]. In the right panels, we show the radius as a function of SGW. We obtain a parabola shape as SGW increases. It shows minima at 0.7 (SGW) which is suppose to be most stable in case of Ca. For heavier nuclei we do not obtain a complete parabola shape, which shows that heavier nuclei are most stable. As in Au nuclei minima at 1.6 (SGW) which appears to be most stable. It is worth mentioning that the change of the Gaussian width (interaction range) is very important since a choice of a different interaction range causes different density profiles of the ground-state nucleus which results in the different strengths of density gradient that in turn has strong influence on the variables such as flow, multifragmentation, pion, kaon production etc. [30, 165, 191] .

For further checking the stability of nuclei, in the Fig.7.3, we plot time evolution of largest fragment for different nuclei. Largest fragment is a remnant of the spectator matter and hence is detached from the rest of system much earlier. More extended wave packet i.e. broader Gaussian width leads to small number of fragments. These fragments are somewhat heavier than those fragments from simulations with smaller wave packet i.e. for narrow Gaussian. This is due to the fact that in the case of broader Gaussian, particles in a cluster are bound to large number of other nucleon inside a cluster. On the other hand, a reduced width leads to fluctuations that causes excited nucleus to dissolve easily. Broader Gaussian produces more excited fragments compared to narrow Gaussian. Broader Gaussian binds more nucleon into fragments. These nucleons have a large relative momentum and thus are bound to decay. We select SGW range (lower-higher) for different nuclei as shown in figure for $^{197}Au_{79}$ it is (0.8-1.3), $^{139}La_{57}$ (0.8-1.2), $^{118}Sn_{50}$ (0.8-1.2), $^{86}Kr_{36}$ (0.7-1.1), $^{40}Ca_{20}$ (0.5-0.9), $^{20}Ne_{10}$ (0.5-0.8). In this range, number of heaviest fragment produced is almost same. Several different system sizes and physical pictures were considered for deeper understanding.

7.3.2 The averaged $\langle P_x/A \rangle$ as a function of Y_{cm}/Y_{beam} and time evolution and energy dependence of directed flow for different SGW

There are two methods in the literature used to find the balance energy [146]. In the first case, balance energy is extracted from the $\langle P_x/A \rangle$ plots, The second method is to study the incident energy dependence of the directed transverse in-plane flow $\langle P_x^{dir} \rangle$ discussed in detail in **chapter 3**. The $\langle P_x^{dir} \rangle$ is defined over the entire rapidity region and therefore expected to present an easier way of measuring the in-plane flow rather than the complicated $\langle P_x/A \rangle$ plot. First, we will discuss in Fig.7.4 the distribution of transverse momentum versus the rapidity Y_{cm}/Y_{beam} at different incident energies from 45 to 1000 MeV/nucleon for $^{197}Au_{79} +^{197} Au_{79}$ system at b=3 fm. The different lines in the figure shows the variation for different SGW values. From the figure, we see that slope becomes less negative or more positive with an increase in the incident energy. However with a reduction in the SGW value slope gets less negative or more positive, while becomes less positive with enhanced SGW. This indicates that we see a change in slope with the incident energy and SGW. The energy at which slope of rapidity distribution $\langle P_x/A \rangle$ approaches to zero is the balance energy. This figure indicate two value of balance energy that is, E=45 MeV/nucleon (at 0.8 SGW) and around E=50 MeV/nucleon (at 0.9 SGW) for the Au+Au system. As the experimental balance energy for Au+Au is in the range 40-45 MeV/nucleon, so one expects that 0.8 is SGW for Au+Au system which can better explains the experimental data. In Fig.7.5, we display the time evolution of second parameter $\langle P_x^{dir} \rangle$ at different energies for $^{197}Au_{79} +^{197} Au_{79}$ system at reduced as well as enhanced SGW. For lower energy, the directed in-plane flow is negative during the initial phase of reaction. This becomes positive at sufficiently high incident energy. These result show that the interaction among the nucleons are attractive during the initial phase of reaction, which turns out to be repulsive with the increase in the incident energy. These interactions remain either attractive or repulsive throughout the time evolution, which depends on the incident energy and SGW. It is clear from the figure that directed flow becomes more positive or less negative with the incident energy and SGW. There is a sharp transition for Au+Au system from negative to positive directed flow at a particular SGW. This particular transition is not possible at higher incident energies and for higher SGW. Broadening of the Gaussian width L reduces the flow. This also corresponds to the fact that the density gradient to the high density region is smeared out. While smaller value of interaction range enhances the flow by about 10 MeV/c at 400 MeV/nucleon and by 20 MeV/c at 1 GeV/nucleon.

In order to check the influence of SGW on directed flow, we display in Fig.7.6, the incident energy dependence of the directed flow for different system. The flow at higher energies is found to be stronger if the initialization of the nucleus is more compact i.e. for lower value of SGW. At low incident energies, this difference vanishes instead the average Fermi momentum becomes important. But large Fermi momentum lowers the binding

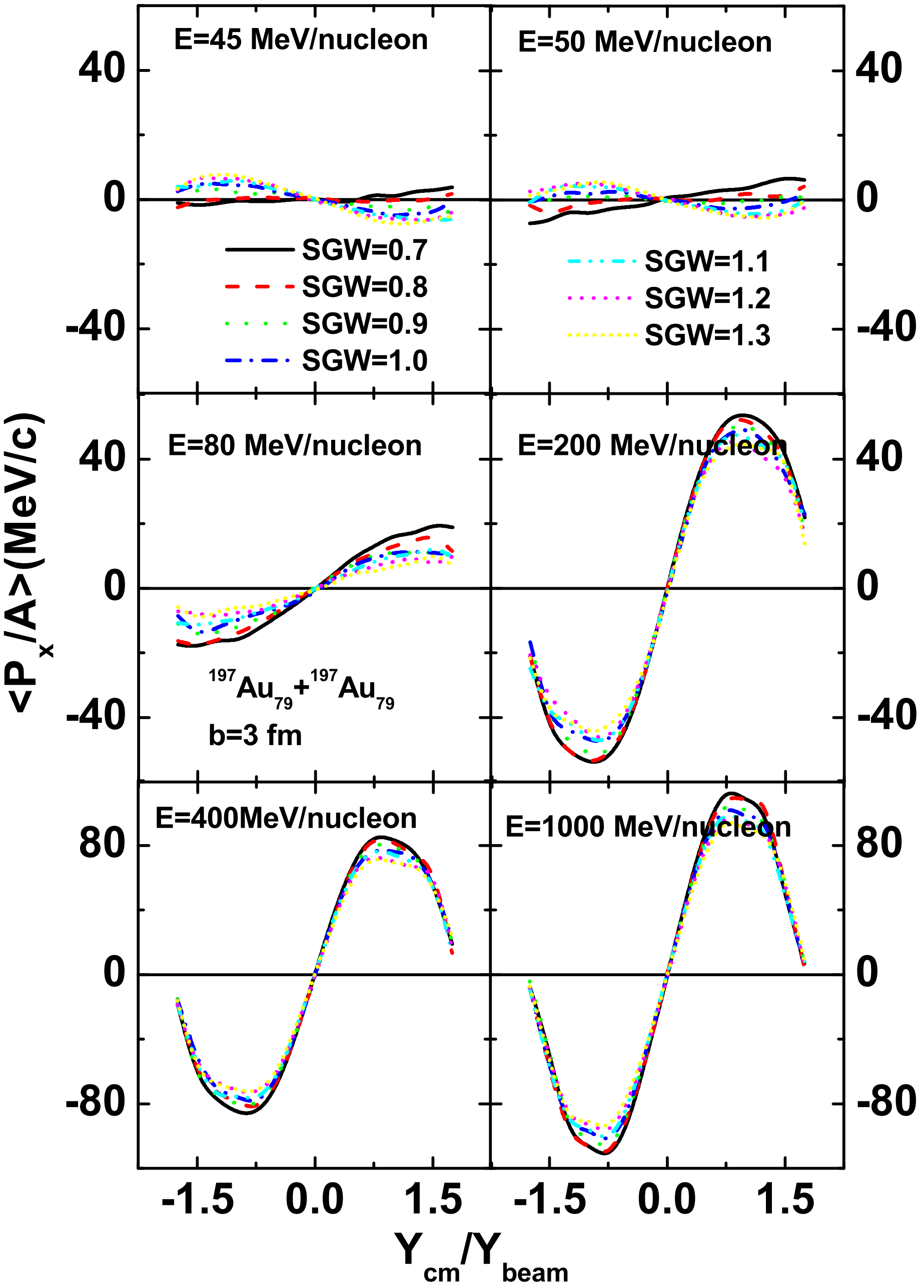

Figure 7.4: The average $\langle P_x/A \rangle$ as a function of rapidity distribution. Here we display the result for Au+Au system at different incident energies and at different SGW.

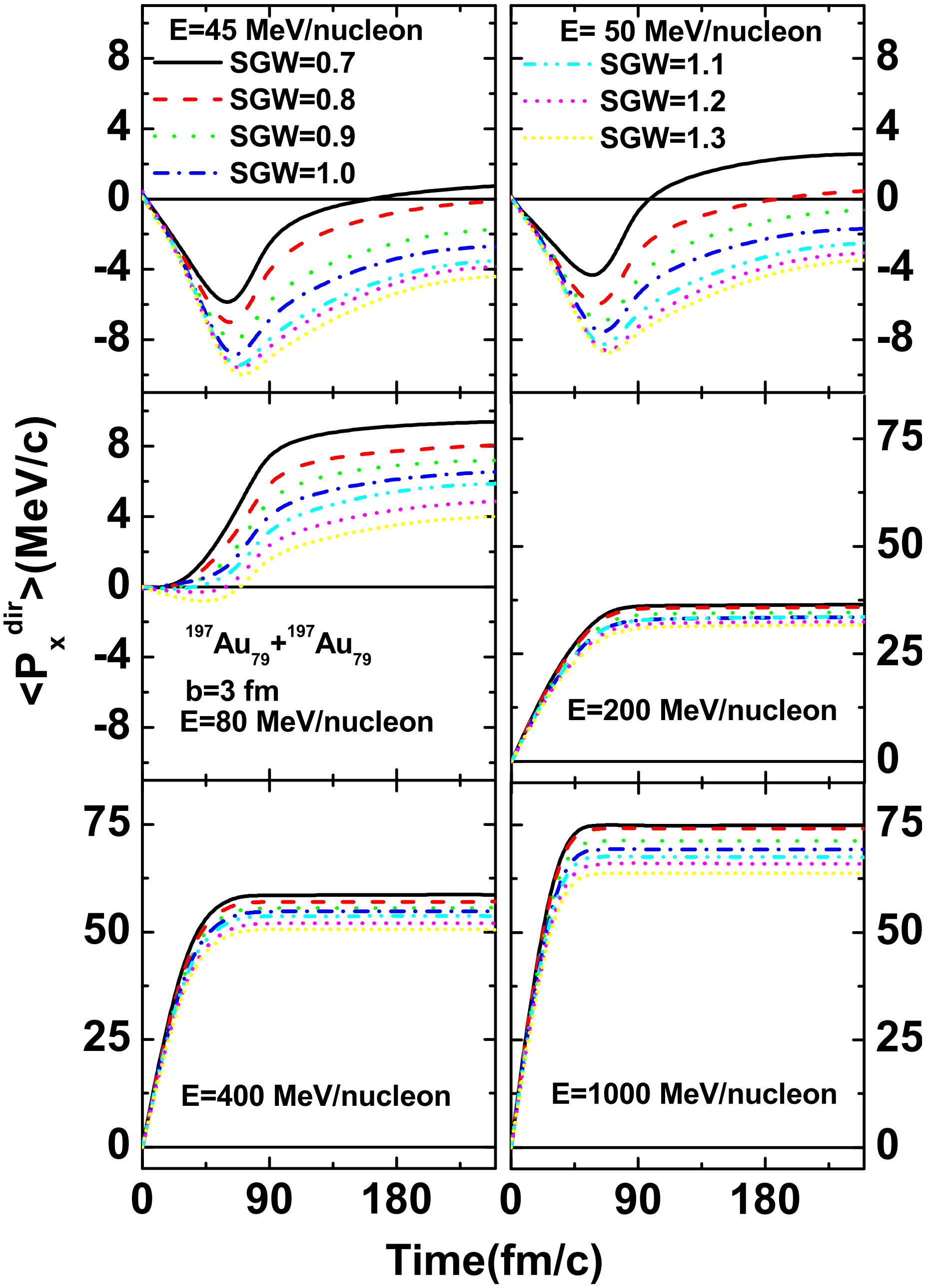

Figure 7.5: Time evolution of $\langle P_x^{dir} \rangle$ for the reaction of Au+Au at different energies. The different lines in the figure represent directed flow at different SGW.

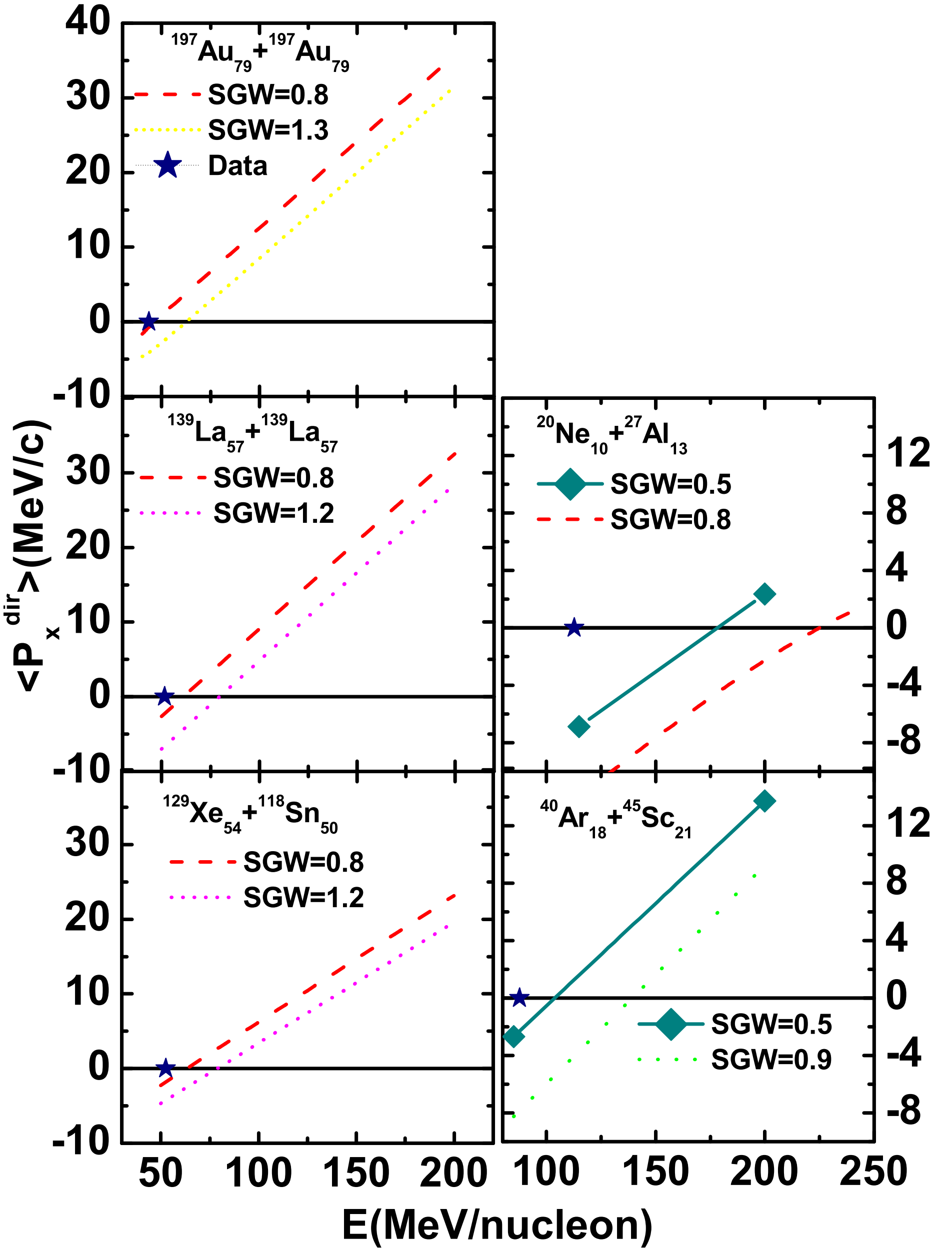

Figure 7.6: Energy dependence of the directed flow $\langle P_x^{dir} \rangle$ for different systems. The two different lines shows the SGW range for these systems.

energy. The binding energy of heavy nuclei is reproduced if local Fermi momentum is employed. The experimental data is represented by stars [146, 147]. The directed flow goes from negative to positive value with an increase in incident energy. This is a general trend and is explained many times in the literature by taking the concept of the mean field and NN cross-section. In this figure, we take the range of the SGW extracted from Fig.7.3. The lowest SGW gives more positive value of the flow compared to highest SGW. The reason is that, as we decrease the Gaussian width, the probability of a reaction taking part increases, which further results in an increase in NN collisions and hence more positive value of directed flow. This results in the decrease of the balance energy. The balance energy is also found to decrease with the composite mass of the system. Except for some lighter system, lowest range scaled Gaussian width (SGW) is found to explain the experimental balance energy nicely. It is studied many times in literature that, for heavier nuclei like Au (SGW=1.0) and for Ca (SGW=0.5), the QMD model can best explain the data [241]. On the contrary, calculations using the IQMD model demands a reduced value of SGW for nearly symmetric systems. The difference is due to the additional effect of isospin dependent cross-sections in IQMD model [30], which were absent in QMD model. As in QMD model, the strength of nn, np, pp cross-section is taken equal, while in IQMD, $\sigma_{np} = 3\sigma_{pp} \approx 3\sigma_{nn}$ [30]. Due to the different strength of np, pp, nn cross-section in IQMD, additional repulsion is produced compared to QMD model. This additional repulsion will force the directed flow to take earlier transition from negative to positive value and hence will lower the balance energy in IQMD model as compared to QMD for same Gaussian width value. That is why, the balance energy that was obtained with QMD for Au nuclei is at SGW=1.0 and in IQMD model it is SGW=0.8. This is first ever parametrization of the balance energy with soft equation of state and Gaussian width range in the presence of reduced cross-sections with experimental available balance energy.

7.3.3 Mean multiplicity of $< M_{IMF} >$ as a function of Z_{bound} and incident beam energy

Further, in the Fig.7.7 we shows the correlation between the mean multiplicity of intermediate mass fragment $< M_{IMF} >$ and Z_{bound} at 600 MeV/nucleon. The intermediate mass fragment (IMF) is defined as a fragment with mass range lies between $5 \leq A \leq A_{tot}/6$. The solid and dotted line is for theoretical result. The fragmentation patterns in $^{197}Au_{79}$+$^{197}Au_{79}$ collision also shown by experimentalist for the four bombarding energies [42]. The familiar rise and fall production is seen to be independent of the projectile energy within the exper-

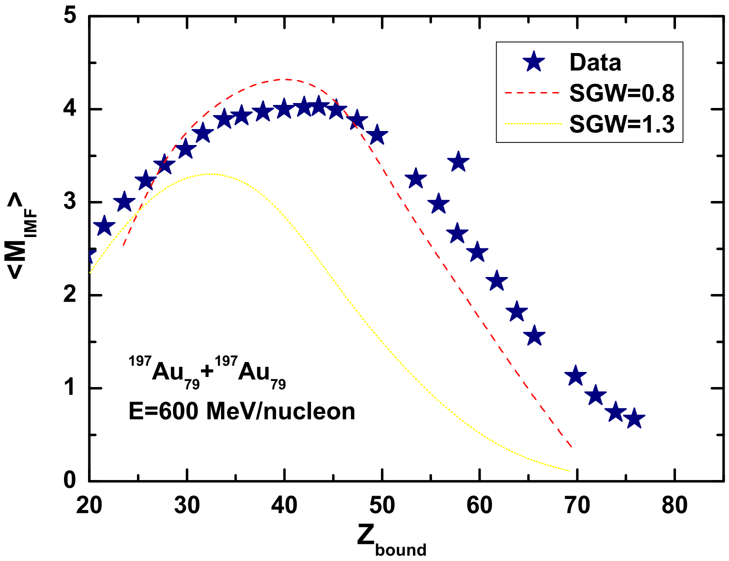

Figure 7.7: The mean multiplicity of intermediate mass fragment $\langle M_{IMF}\rangle$ as a function of Z_{bound} for the reaction $^{197}Au_{79}$ on $^{197}Au_{79}$ at E=600 MeV/nucleon for the experimental data and compared it with the interaction range of Au.

imental accuracy. At $Z_{bound} \approx 40$ the mean multiplicity $< M_{IMF} >$ reaches its maximum 4 to 4.5. It is clear from this figure that the mean multiplicity of IMF increases first with the decrease of Z_{bound} (i.e. with strength of violence of collision) and then starts to decrease after reaching a maximum at $Z_{bound} \approx 40$. It indicates the possible existence of various decay modes of the hot nucleus and the changing of decay modes from the pseudo-fission mode to the multifragmentation mode and then to the vaporization mode [242]. Due to the lack of access to filters, direct comparison with the data could not be made. These comparisons just indicate the trend within theoretical work. In the present work, we take range of the SGW for Au which is 0.8 to 1.3 SGW. We see data is nearly in between these limits. For lowest range Gaussian width, the probability of reaction taking place increases, which further results in an increase in NN collisions and hence $< M_{IMF} >$ increases. As for highest range Gaussian width, $< M_{IMF} >$ decreases compared to reduced SGW. So in symmetric system it is lowest range that nearly match with the experimental data from ALADIN collaboration [220, 230, 231].

In Fig.7.8, we show the $< M_{IMF} >$ vs. Z_{bound} scaling with normalization by Z_P (charge of projectile) for nearly symmetric reactions of $^{107}Sn_{50} +^{120} Sn_{50}$, $^{124}La_{57} +^{120} Sn_{50}$, $^{124}Sn_{50} +^{120} Sn_{50}$ at 600 MeV/nucleon and observe that multiplicities exhibit universal rise and fall of the fragment production. In this figure, study is conducted for neutron rich

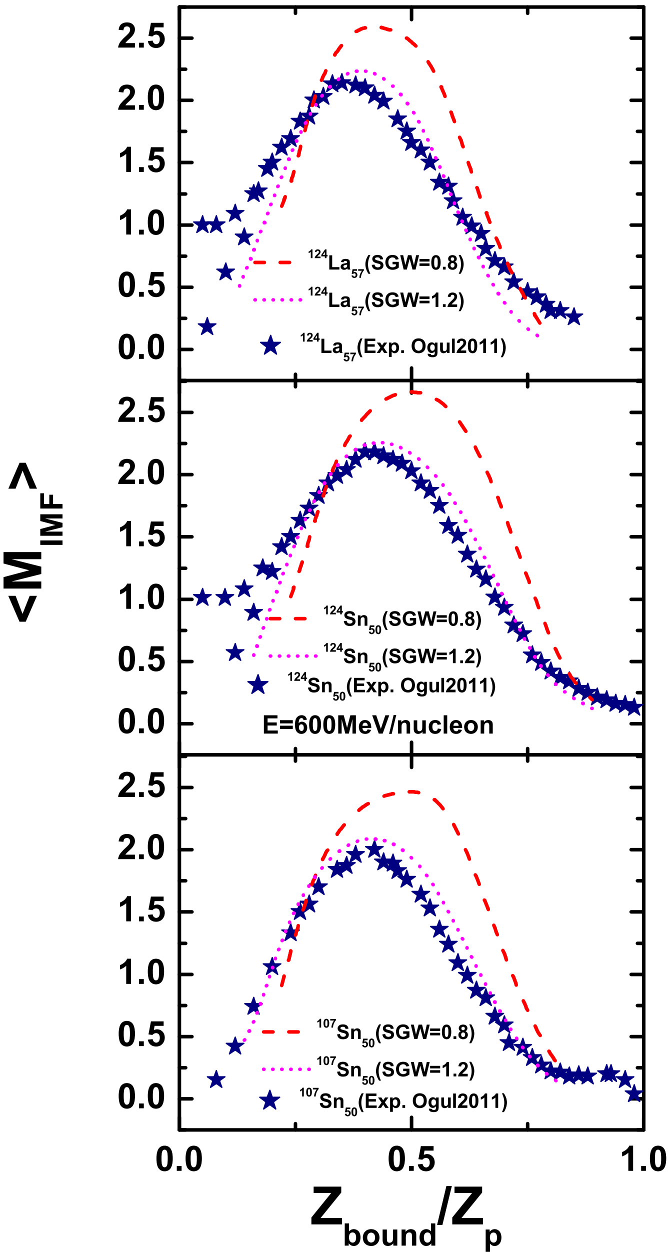

Figure 7.8: The mean multiplicity of intermediate-mass fragment as a function of Z_{bound}/Z_p for the reaction of $^{124}La_{57}+^{120}Sn_{50}$, $^{124}Sn_{50}+^{120}Sn_{50}$, $^{107}Sn_{50}+^{120}Sn_{50}$ at 600 MeV/nucleon. Experimental data are taken from Ogul et al. [220]. Solid and dash lines indicate the SGW for La and Sn.

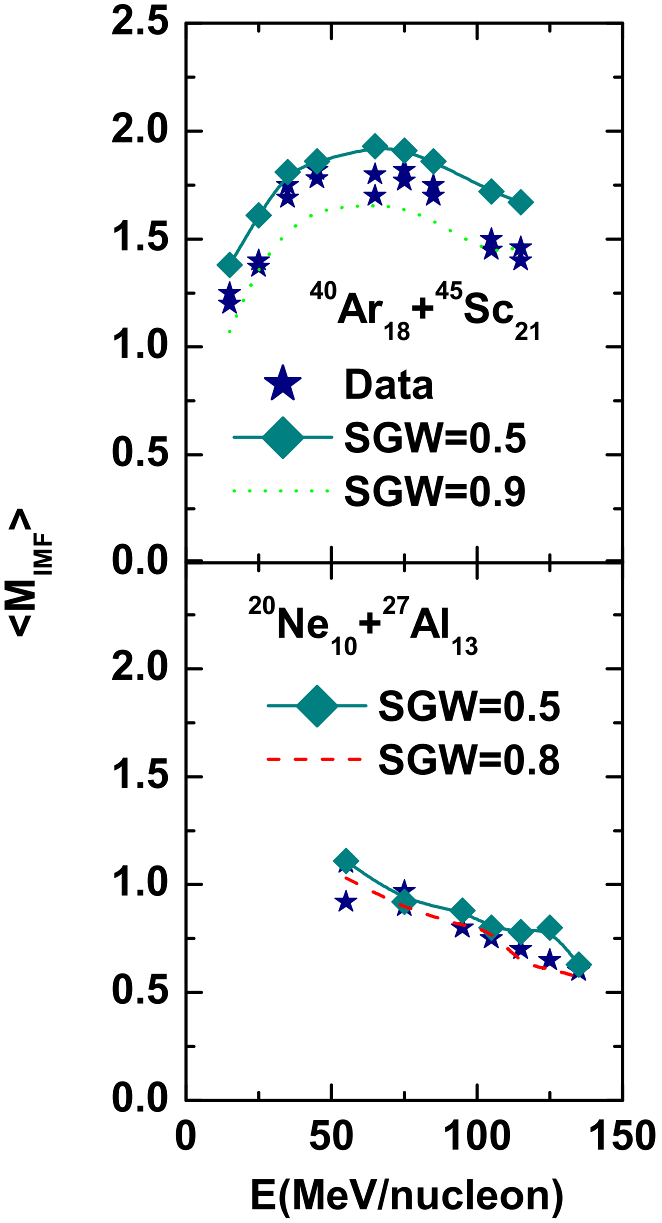

Figure 7.9: The average multiplicity of IMFs as a function of beam energy for the reactions $^{20}Ne_{10} +^{27} Al_{13}$, $^{40}Ar_{18} +^{45} Sc_{21}$. The symbols represent the NSCL experimental results, while solid and dash line represent the results obtained within IQMD model for two limiting value of SGW.

$^{124}Sn_{50}$ and neutron poor $^{124}La_{57}$ projectile. The difference of the isotope distribution between the neutron rich and neutron poor is shown in this figure. In particular, fragment yield on the neutron-rich side are larger in case of $^{124}Sn_{50}$. The range comes from plots of time evolution of maximum mass fragment for La and Sn 0.8-1.2 (SGW) is then compared with experimental data [220] and see that for these systems it is the highest range that matches with the experimental data taken from ALADIN collaboration. Again lesser number of $< M_{IMF} >$ are produced when we increase the Gaussian width compared to reduced Gaussian width. As we increase the system size the number of IMFs increases. Multiplicity of IMFs ($< M_{IMF} >$) is large for $^{124}La_{57} +^{120} Sn_{50}$ as compared to $^{107}Sn_{50} +^{120} Sn_{50}$. Out of $^{124}Sn_{50}$ and $^{107}Sn_{50}$, $^{124}Sn_{50}$ has larger multiplicity of IMFs because $^{124}Sn_{50} +^{120} Sn_{50}$ is more symmetric then $^{107}Sn_{50} +^{120} Sn_{50}$ or $^{124}La_{57} +^{120} Sn_{50}$.

In Fig.7.9, we analyze the effect of Gaussian width range in nearly symmetric reactions of $^{20}Ne_{10} +^{27} Al_{13}$, $^{40}Ar_{18} +^{45} Sc_{21}$ by plotting $< M_{IMF} >$ as a function of beam energy at scaled impact parameter $\hat{b} = 0.3$ using $\sigma = 0.9\sigma_{NN}$ [81]. We see that experimental data taken from NSCL collaboration [53] is in between these limits. One further sees that multiplicity of IMFs decreases in central Ne+Al reaction with increase in energy. At very low energy for Ne+Al system, there are no collision so no $< M_{IMF} >$ are produced below 50 MeV/nucleon. For the reaction of Ar+Sc, similar trend emerges above 55 MeV/nucleon, as in case of Ne+Al but for energies below 55 MeV/nucleon, we see dominant role of mean field and hence increase in intermediate mass fragments. Hence, Gaussian width range and incident energy effects the multiplicity of IMFs. Lesser number of fragments are produced for highest SGW and the contrary is true for narrow SGW.

In these figures experimental data taken from ALADIN and NSCL collaboration. The range of the SGW extracted from Fig.7.3, is then compared with the experimental data. It is predicted from the figures that lowest range of $^{197}Au_{79}$ nuclei and highest range of $^{124}La_{57}$, $^{120}Sn_{50}$, $^{124}Sn_{50}$ is in agreement with the data of ALADIN collaboration. But experimental data of NSCL collaboration lies in between the SGW range.

7.3.4 System mass dependence of balance energy for SGW range

In Fig.7.10, we display the energy of the vanishing flow or balance energy (E_{bal}) as a function of composite mass of a system that range from $^{20}Ne_{10}+^{27}Al_{13}$ to $^{197}Au_{79}+^{197}Au_{79}$. It is also well known that the mass dependence of the balance energy results from two competing factors: the competition between attractive mean field, which can be associated

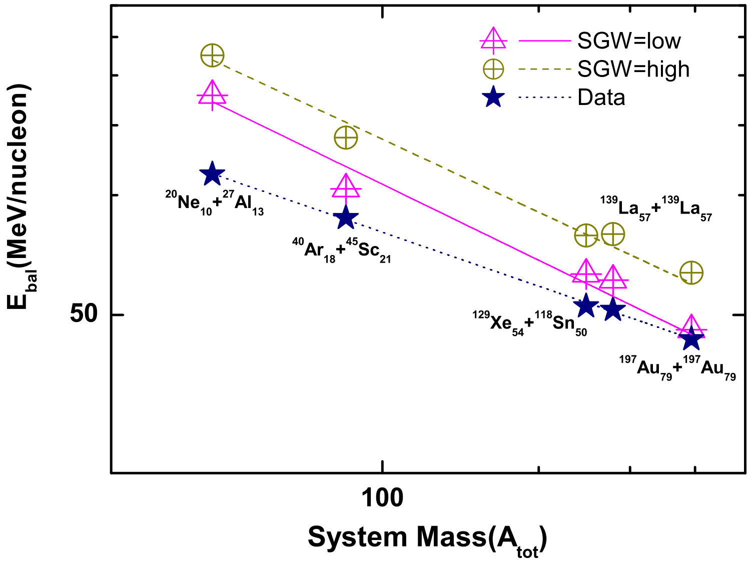

Figure 7.10: The balance energy as a function of the combined mass of the system. The experimental points are represented by stars and low range SGW by crossed triangle and high range SGW by crossed circle and lines are fitted with the power law of the form C$(A_{tot})^{\tau}$.

with the surface area of interacting nuclei and the repulsive nucleon-nucleon scattering potentials, which scales as number of nucleons (A) present. In this figure, E_{bal} is shown for the experimental data (open stars), Low range (SGW) by crossed triangle and High range SGW by crossed circle. High value of SGW range gives large balance energy compared to narrow value of SGW range. This is due to the fact that as Gaussian width increases, collision decreases and nucleon-nucleon cross-section increases so flow balances at higher energies compared to narrow Gaussian in which system balance at lower energies due to increase in nucleon-nucleon collisions. All curves are fitted with a power law of the form C$(A_{tot})^{\tau}$. The experimental data are fitted by $\tau = (-0.45 \pm 0.0076)$.

The balance energy is found to decrease with the increase in the composite mass of the system, which is well known trend discussed many times in the literature [146, 147]. The present calculation depicts τ value for the low range -0.63 ± 0.065 and for the high range -0.61 ± 0.046. The present IQMD model with a soft equation of state and low range scaled Gaussian width (SGW) along with $\sigma = 0.9\sigma_{NN}$ can influence the reaction dynamics drastically. The low range SGW explains the data for all nuclei, except for some lighter nuclei. The lighter nuclei, when checked out, demand for further reduction in Gaussian width. In this study, we find that low range SGW cannot explains the experimental data of all collaboration. Either it is the highest or lowest range which explains the experimental data of ALADIN. Experimental data of NSCL lies in between the SGW range. The further work in this direction is in progress.

7.4 Summary

By using the IQMD model, we have presented a detailed analysis of the role played by interaction range on fragmentation and collective flow. The interaction range for different system sizes comes from the time evolution of largest fragment and this range is then compared with the experimental data of ALADIN and NSCL. We showed that the collective flow due to mean field is attractive whereas it is repulsive for the collision part. The balancing of these two parts results in disappearance of flow. The value for E_{bal} for different systems scales as $A^{-1/3}$.

For a given set of model ingredients, we find that width has a sizable effect and optimum value for different nuclei $^{197}Au_{79}$, $^{139}La_{57}$, $^{118}Sn_{50}$, $^{86}Kr_{36}$, $^{40}Ca_{20}$, $^{20}Ne_{10}$ and for various systems. For $^{197}Au_{79}$ it is the lowest range value and for $^{124}La_{57}$, $^{120}Sn_{50}$, $^{124}Sn_{50}$ it is the highest range value that agree well with the experimental data. At the same time we know that different set of parameter can influence the reaction dynamics drastically. Hence, in our opinion it may not be possible to pin down the width to a very narrow level.

Chapter 8

Summary and outlook

8.1 Summary

In the present thesis, isospin-dependent quantum molecular dynamics (IQMD) model is used to generate the phase-space of nucleons. The phase space was then analyzed using different clusterization algorithms to get infomation about the collective flow as well as multifragmentation. These results were then compared with the experimental data.

In **chapter 1**, we presented a general introduction to the field of heavy-ion physics and various phenomena like isospin physics, nuclear equation of state, multifragmentation, elliptical flow and directed flow. The review of the experimental and theoretical attempts for collective flow and multifragmentation was also discussed in this chapter.

The various theoretical models in particular, IQMD model which was used for the present study was briefly discussed in **chapter 2**. The secondary models were then discussed in brief which were used to clusterize the nucleons and get fragments.

In **chapter 3**, using the IQMD model, we studied the effect of reduced as well as enhanced isospin-dependent cross-section (σ= 0.7 to 1.3 σ_{NN}) on the directed flow and balance energy. A large number of reactions were studied , ${}^{12}C_6$ + ${}^{12}C_6$, ${}^{20}Ne_{10}$ + ${}^{27}Al_{11}$, ${}^{40}Ar_{18}$ + ${}^{45}Sc_{21}$, ${}^{40}Ar_{18}$ + ${}^{51}V_{23}$, ${}^{86}Kr_{36}$ + ${}^{93}Nb_{41}$, ${}^{64}Zn_{30}$ + ${}^{58}Ni_{28}$, ${}^{93}Nb_{41}$ + ${}^{93}Nb_{41}$ ${}^{129}Xe_{54}$ + ${}^{118}Sn_{50}$, ${}^{139}La_{57}$ + ${}^{139}La_{57}$, and ${}^{197}Au_{79}$ + ${}^{197}Au_{79}$ where experimental balance energy is available. Our calculation with a stiff equation of state and reduced cross-section ($\sigma = 0.9\sigma_{NN}$) is in good agreement with the experimental findings, except for ${}^{12}C_6 +^{12} C_6$. The dependence of isospin-dependent cross-section weakens with the increase in the size of the system. The interactions among the nucleons remain either attractive or repulsive throughout the time evolution, which depends on the incident energy, isospin-dependent cross-section, as well as the composite mass of the system and it indicates the sharp transition for each system from negative to positive directed flow at a particular cross-section. The directed flow goes from a negative to positive value with an increase in the incident energy. This is the general trend and is explained many times in the literature by taking the concept of mean field and NN cross-section. Lighter systems remain in the environment of mean field compared to NN collisions at any given incident energy. It is also observed that a higher incident energy is needed in lighter cases to balance the attractive and repulsive forces compared to heavier systems. This is due to the dominance of Coulomb repulsion with an increase in the composite mass of the system. The balance energy is parametrized with the N/Z ratio in terms of a power law, which is quite similar with the parametrization of the composite mass of the system, but the τ values are different in both cases.

In **chapter 4**, using the IQMD model, we studied the fragment structure at, above and below the energy of vanishing flow for $^{197}Au_{79} + ^{197}Au_{79}$, $^{139}La_{57} + ^{139}La_{57}$, $^{93}Nb_{41} + ^{93}Nb_{41}$, $^{86}Kr_{36} + ^{93}Nb_{41}$, $^{64}Zn_{30} + ^{58}Ni_{28}$, $^{40}Ar_{18} + ^{45}Sc_{21}$. The corresponding energy of vanishing flow (EVF) for these system were reported to be 48, 58, 62, 56, 64, 80 MeV/nucleon respectively. In this chapter, mass dependent Gaussian width was employed. The free nucleons, light mass fragments (LMFs) are emitted from the participant source that scales with the size of the emitting source while medium mass fragments (MMFs) and intermediate mass fragments (IMFs) come from the spectator part showing well known universality in the multiplicity. Since for lighter system energy of vanishing flow is very high. The transition from the spectator to participant matter is swift and sudden. The reverse is true for heavy systems. Final results are compared with NSCL experimental data. Fragmentation produced due to two colliding nuclei does not follow any particular structure at the energy of vanishing flow.

In **chapter 5**, using the IQMD model, we have studied the correlation between transition energy E_{trans} and balance energy E_{bal}. We have investigated the elliptical flow of fragments for different reacting systems at incident energies between 40 and 1200 MeV/nucleon. The elliptical flow is found to show a transition from in-plane to out-of-plane at a certain beam energy in the midrapidity region. This is due to the fact that mean field at low energy, which contributes to the formation of a rotating compound system, becomes less important and the collective expansion process based on the nucleon-nucleon scattering starts to be predominant. This transition energy is found to depend on the size of the fragments, composite mass of the reacting system, and the impact parameter of the reaction. The free and light-charged particles feel the mean field directly, while heavy fragments have weaker sensitivity. The free particles and LMFs, which originate from the participant zone, show a systematic behavior with the beam energy and with the composite mass of the system. The heavier the system, greater the Coulomb repulsion and more is the elliptical flow. Our calculation with a stiff equation of state and a reduced isospin-dependent nucleon-nucleon cross section ($\sigma = 0.9\sigma_{NN}$) is in good agreement with the experimental findings of INDRA, FOPI, and PLASTIC Ball collaboration. The difference between the balance and transition energy decreases with the increase in the composite mass of colliding nuclei. This tells us that due to the increase of neutrons in colliding nuclei, the difference between the two energies decreases

In **chapter 6**, we have carried out a detailed analysis of the role of spatial and momentum constraints on fragmentation using an IQMD model. We compared our theoretical results with the experimental data of ALADIN and NSCL. Several different system sizes and physical pictures were considered for deeper understanding. We studied the role of momentum cuts and spatial correlations (i.e., the range of clusterization) in fragment formation. Two nucleons were deemed to be in the same fragment if their centroids were less than 4 fm apart, which is a condition of the MST method. For $R_{clus} = 4$ fm there is a systematic trend for different value of P_{clus} compared to other clusterization parameters. Our analysis indicated that the effect of a cut in momentum space on fragment formation is stronger if the cut in the relative momenta of two nucleons is 240 MeV/c. For higher values of the cut production remains the same. We further found that the spatial distance of 4 fm with a realistic value of cut (240 MeV/c) was important in order to get the most bound structure of fragments in the central collisions. For a given set of input parameters, we found that the spatial correlation and momentum constraints had a sizable effect on fragmentation.

In **chapter 7**, we presented a detailed analysis of the role played by interaction range on fragmentation and collective flow. We change the scaled Gaussian width (SGW) by reducing and enhancing SGW from normal SGW. In the case of broader Gaussian, particles in a cluster are bound to a large number of other nucleons inside a cluster. A reduced width leads to fluctuations which results in a large number of light and intermediate mass fragments. Broader Gaussian produces more excited fragments compared to narrow Gaussian. The interaction range for different system sizes comes from the time evolution of largest fragment and this range is then compared with the experimental data of ALADIN and NSCL. It is noted that either the highest or lowest range is in agreement with the experimental data. The lowest SGW gives more positive value of flow and also gives large multiplicity of IMF $\langle M_{IMF} \rangle$ as compared to highest SGW. The reason is that as we decrease the Gaussian width, the probability of a reaction taking place increases, which further enhances the NN collisions and hence more positive value of the directed flow. We showed that the collective flow due to the mean field is attractive whereas it is repulsive for the collision part. The balancing of these two parts results in the disappearance of flow. The value of E_{bal} for different systems scales as $A^{-1/3}$. For a given set of model ingredients, we find that width has a sizable effect and optimum value for different nuclei $^{197}Au_{79}$, $^{139}La_{57}$, $^{118}Sn_{50}$, $^{86}Kr_{36}$, $^{40}Ca_{20}$, $^{20}Ne_{10}$. At the same time we know that different set of parameter can influence the reaction dynamics drastically. Hence, in our opinion it may not be possible to pin down the width to a very narrow level.

Summarizing, we have attempted to understand the phenomena of multifragmentation, elliptical flow, directed flow in intermediate energy heavy-ion collisions. First of all, we find the isospin dependent reduced cross-section and see its effect on directed flow, elliptic flow and multifragmentation. Then we find the effect of different range of R/P cut on fragmentation depends on the mass, energy and impact parameter of the system. After that we find the effect of width of Gaussian wave packet on fragment flow and multifragmentation. The results obtained from these effort are then compared with the experimental data of different collaborations.

8.2 Outlook

One can try the balance energy prediction with an enhanced isospin-dependent cross-section in the presence of a momentum-dependent interaction for $^{12}C_6 +^{12} C_6$, which was earlier studied using the QMD in the presence of momentum-dependent interactions. Also it would be of interest to do these calculation with the density dependent symmetry energy. Once the balance energy is predicted for different system one can predict the transition energy for the various systems. The clusterization range and SGW range can be used further to analyze the data. One can try different method of clusterization to perform the calculation.

Bibliography

[1] R. Stock, Phys. Rep. **135**, 259 (1986).

[2] H. Stöcker and W. Greiner, Phys. Rep. **137**, 277 (1986).

[3] J. Stachel and G. R. Young, Annu. Rev. Nucl. Part. Sci. **42**, 537 (1992).

[4] P. Senger and H. Ströbele, J. Phys. G **25**, R59 (1999).

[5] J. Aichelin, Phys. Rep. **202**, 233 (1991).

[6] N. Herrmann, J. P. Wessels, and T. Wienold, Annu. Rev. Nucl. Part. Sci. **49**, 581 (1999); W. Reisdorf and H.G. Ritter, Annu. Rev. Nucl. Part. Sci. **47**, 663 (1997).

[7] W. Reisdorf *et al.*, Nucl. Phys. A **612**, 493 (1997).

[8] J. W. Harris and B. Müller, Annu. Rev. Nucl. Part. Sci **46**, 71 (1996).

[9] Empedocles, Fragment 12/6 and 17/109. (≈440BC), in Brad Inwood, The poem of Empedocles, University of Toronto Press (1991).

[10] N. K. Glendenning, Phys. Rev. D **46**, 1274 (1992).

[11] D. Q. Lamb, J. M. Lattimer, C. J. Pethick, and D. G. Ravenhall, Phys. Rev. Lett. **41**, 1623 (1978); H. Jaqaman, A. Z. Mekjian, and L. Zamick, Phys. Rev. C **27**, 2782 (1983); *ibid* **29**, 2067 (1984);

[12] P. J. Siemens, Nature London **305**, 410 (1983).

[13] A. L. Goodman, J. I. Kapusta, and A. Z. Mekjian, Phys. Rev. C **30**, 851 (1984).

[14] A. S. Parvan, Nucl. Phys. A **887**, 1 (2012).

[15] J. Pochodzalla, Prog. Part. Nucl. Phys. **39**, 443 (1997).

[16] J. P. Bondorf, S. I. A. Garpman, J. Zimanyi, Nucl. Phys. A **296**, 320 (1978).

[17] J. Cugnon, Phys. Lett. B **135**, 374 (1984); C. E. Aguiar, R. Donangelo, C. O. Dorso, R. S. Gomes, and N. Goncalves, Phys. Rev. C **46**, 1069 (1992); H. W. Barz, J. P. Bondorf, D. Idier, and I. N. Mishustin, Phys. Lett. B **382**, 343 (1996).

[18] B. K. Agarwal, R. Kumar, and S. K. Dhiman, Phys. Rev. D **77**, 087301 (2008).

[19] M. D. Voskresenskaya and S. Typel, Nucl. Phys. A **887**, 42 (2012).

[20] J. Aichelin, G. Peilert, A. Bohnet, A. Rosenhauer, H. Stöcker and W. Greiner, Phys. Rev. C **37**, 2451 (1988).

[21] S. A. Bass, C. Hartnack, H. Stöcker, W. Greiner, Phys. Rev. C **51**, 3343 (1995); J. P. Blaizot, Phys. Rep. **64**, 171 (1980).

[22] C. Hartnack and J. Aichelin, Phys. Rev. C **49**, 2801 (1994); J. Treiner, H. Krivine, and O. Bohigas, Nucl. Phys. A **371**, 253 (1981).

[23] G. Kortemeyer, W. Bauer, and G. J. Kunde, Phys. Rev. C **55**, 2730 (1997).

[24] T. T. S. Kuo, S. Ray, J. Shamanna, and R. K. Su, Int. J. of Mod. Phys. E **5**, 303 (1996).

[25] B. A. Li, C. M. Ko, and W. Bauer, Int. J. of Mod. Phys. E **7**, 147 (1998).

[26] D. V. Shetty and S. J. Yennello, Pramana J. Phys. **75**, 259 (2010).

[27] A. Bohr and B. R. Mottelson, Nuclear Structure **1**, (Benjamin, New York) (1969).

[28] C. F. v. Weizsäcker, Z. Physik **96**, 431 (1935); H. A. Bethe and R. F. Bacher, Rev. Mod. Phys. **8**, 82 (1936).

[29] B. A. Li and S. J. Yennello, Phys. Rev. C **52**, R1746 (1995); B. A. Li, Z. Ren, C. M. Ko, S. J. Yennello, Phys. Rev. Lett. **76**, 4492 (1996).

[30] C. Hartnack *et al.*, Eur. Phys. J. A **1**, 151 (1998); C. Hartnack, Li. Zhuxia, L. Neise, G. Peilert, A. Rosenhauer, H. Sorge, J. Aichelin, H. Stöcker, W. Greiner, Nucl. Phys. A **495**, 303 (1989); C. Hartnack Ph.D thesis, GSI- Report **93-5** (1993); C. Hartnack, J. Aichelin, H. Stöcker, and W. Greiner, Mod. Phys. Lett. A **9**, 1151 (1994); Phys. Lett. B **336**, 131 (1994); C. Hartnack *et al.*, Phys. Rep. **510**, 119 (2012).

[31] William A. Friedman, Phys. Rev. C **40**, 2055 (1989); D. Cebra, PhD. thesis, Michigan State University, 1990; T. Q. Li, PhD. thesis, Michigan State University, 1993.

[32] G. Bertsch and P. J. Siemens, Phys. Lett. B **126**, 9 (1983).

[33] J.E. Finn et al., Phys. Rev. Lett. **49**, 1321 (1982).

[34] D. J. Magestro, PhD. thesis, Michigan State University, 2000.

[35] B. Jakobsson, G. Jönsson, B. Lindkvist, A. Oskarsson, Z. Phys. A **307**, 293 (1982).

[36] H. A. Gustafsson *et al.*, Phys. Rev. Lett. **52**, 1590 (1984).

[37] R. E. Renfordt *et al.*, Phys. Rev. Lett. **53**, 763 (1984).

[38] H. Ströbele *et al.*, Phys. Rev. C **27**, 1349 (1983).

[39] A. Baden *et al.*, Nucl. Instrum. Methods **203**, 189 (1982).

[40] J. Hubele *et al.*, Z. Phys. A **340**, 263 (1991).

[41] P. Kreutz *et al.*, Nucl. Phys. A **556**, 672 (1993).

[42] A. Schüttauf *et al.*, Nucl. phys. A **607**, 457 (1996).

[43] C. A. Ogilvie *et al.*, Phys. Rev. Lett. **67**, 1214 (1991).

[44] see http://www-aladin.gsi.de.

[45] J. Pouthas *et al.*, Nucl. Instrum. Methods Phys. Res. A **357**, 418 (1995).

[46] N. Bastid *et al.*, Nucl. Phys. A **622**, 573 (1997).

[47] H. H. Gutbrod, K. H. Kampert, B. W. Kolb, A. M. Poskanzer, H. G. Ritter, H. R. Schmidt, Phys. Lett. B **216**, 267 (1989).

[48] D. Brill *et al.*, Z. Phys. A **355**, 61 (1996).

[49] W. Scheid, H. Müller, W. Greiner, Phys. Rev. Lett. **32**, 741 (1974).

[50] Y. Leifels *et al.*, Phys. Rev. Lett. **71**, 963 (1993).

[51] H. H. Heckman, D. E. Greiner, P. J. Lindstrom, and F. S. Bisser, Science **174**, 1130 (1971); H. A. Grunder, W. D. Hartsough, and E. J. Lofgren, Science **174**, 1128 (1971).

[52] The K500 & K1200, A Coupled Cyclotron Facility at the National Superconducting Cyclotron Laboratory, NSCL Report MSUCL-939, July, 1994.

[53] G. D. Westfall *et al.*, Nucl. Instrum. Methods Phys. Res. A **238**, 347 (1985).

[54] I. Weidenhöver, M. Steiner, D. J. Morrissey, B. M. Sherrill, D. Bazin, J. Stetson, A. Stolz, O. Tarasov, J. Yurkon, and the NSCL staff, AIP Conf. Proc. **610**, 937 (2001); A. Stolz, T. Baumann, T. N. Ginter, D. J. Morrissey, M. Portillo, B. M. Sherrill, M. Steiner, and J. W. Stetson, Nucl. Instrum. Methods Phys. Res. B **241**, 858 (2005).

[55] E. Schiller, H. Muther, P. Czerski, Phys. Rev. C **59**, 2934 (1999); P. Bozek, P. Czerski, Acta. phys. Polo. B **34**, 2759 (2003).

[56] V. Kaur, PhD. Thesis 2011, Thapar University, Patiala (India).

[57] J. P. Bondorf, R. Donangelo, I. N. Mishustin, C. J. Pethick, H. Schulz, and K. Sneppen, Nucl. Phys. A **443**, 321 (1985).

[58] J. P. Bondorf, A.S. Botvina, A.S. Lljinov, I.N. Mishustin, and K. Sneppen, Phys.Rep. **257**, 133 (1995).

[59] S. Pal, S. K. Samaddar, and J. N. De, Nucl. Phys. A **608**, 49 (1996), D. K. Srivastava *et al.*, Nucl-th/0506075 (2005); L. Satpathy, M. Mishra, A. Das, M. Satpathy, Phys. Lett. B **237**, 181 (1990); C. B. Das, A. Das, L. Satpathy, M. Satpathy, Phys. Rev. C **53**, 1833 (1996).

[60] J. P. Bondorf, R. Donangelo, I. N. Mishustin, H. Schulz, Nucl. Phys. A **444**, 460 (1985); H. W. Barz, J. P. Bondorf, R.Donangelo, I.N. Mishustin, H. Schulz, Nucl. Phys. A **448**, 753 (1986); G. A. Souliotis, A. S. Botvina, D. V. Shetty, A. L. Keksis, M. Jandel, M. Veselsky, S. J. Yennello, Phys. Rev. C **75**, 011601 (2007); S. Pal, S. K. Samaddar, J. N. de, and B. Djerroud, Phys. Rev. C **57**, 3246 (1998); A. Das, M. Mishra, M. Satpathy, and L. Satpathy, J. Phys. G: Nucl. and Part. Phys. **19**, 319 (1993).

[61] D. H. E. Gross, Rep. Prog. Phys. **53**, 605 (1990).

[62] W. Bauer, D. R. Dean, U. Mosel, and U. Post, Phys. Lett. B **150**, 53 (1985); W. Bauer, U. Post, D. R. Dean, and U. Mosel, Nucl. Phys. A **452**, 699 (1986).

[63] J. Pan, S. Das Gupta, Phys. Lett. B **344**, 29 (1995); J. Pan, S. D. Gupta, Phys. Rev. C **51**, 1384 (1995); S. D. Gupta and J. Pan, Phys. Rev. C **53**, 1319 (1996).

[64] W.A. Friedman, Phys. Rev. C **42**, 667 (1990).

[65] A. K. Kerman and S. E. Koonin, Ann. of Phys. **100**, 332 (1976); P. Bonche, S. Koonin and J. W. Negele, Phys. Rev. C **13**, 1226 (1976); K. T. R. Davies and S. E. Koonin, Phys. Rev. C **23**, 2042 (1981); M. D. Toro, G. Russo, and F. Duggan, Phys. Rev. C **21**, 2054 (1980).

[66] G.F. Bertsch, H. Kruse, and S. D. Gupta, Phys. Rev. C **29**, R673 (1984).

[67] J. J. Molitoris, H. Stocker, and B. L. Winer, Phys. Rev. C **36**, 220 (1987); W. Cassing, V. Metag, U. Mosel, and K. Niita, Phys. Rep. **188**, 363 (1990).

[68] C. Gale, G. M. Welke, M. Prakash, S. J. Lee, and S. D. Gupta, Phys. Rev. C **41**, 1545 (1990).

[69] H. Kruse, B. V. Jacak, and H. Stocker, Phys. Rev. Lett. **54**, 289 (1985).

[70] J. J. Molitoris, A. Bonasera, B. L. Winer, and H. Stoecker, Phys. Rev. C **37**, 1020 (1988).

[71] E. Suraud, Ch. Gregoire, and B. Tamain, Prog. Part. Nucl. Phys. **23**, 357 (1989).

[72] L. Wilets, Y. Yariv, and R. Chestnut, Nucl. Phys. A **301**, 359 (1978); A. R. Bodmer, C. N. Panos, and A. D. MacKellar, Phys. Rev. C **22**, 1025 (1980); A. Vicentini, G. Jacucci and V. R. Pandharipande, Phys. Rev. C **31**, 1783 (1985).

[73] J. Aichelin and H. Stöcker, Phys. Lett. B **176**, 14 (1986).

[74] G. Peilert, H. Stöcker, W. Greiner, A. Rosenhauer, A. Bohnet, and J. Aichelin, Phys. Rev. C **39**, 1402 (1989).

[75] M. Colonna, M. D. Toro, G. Fabbri, S. Maccarone, Phys. Rev. C **57**, 1410 (1998).

[76] B. A. Li, Phys. Rev. Lett. **88**, 192701 (2002).

[77] C. Hartnack, H. Oeschler, and J. Aichelin, Phys. Rev. Lett. **90**, 102302 (2003); J. Phys. G: Nucl. and Part. Phys. **35**, 044021 (2008).

[78] P.-B. Gossiaux and J. Aichelin, Phys. Rev. C **56**, 2109 (1997).

[79] J. Singh, S. Kumar and R. K. Puri, Phys. Rev. C **62**, 044617 (2000).

[80] J. Singh and R. K. Puri, Phys. Rev. C **65**, 024602 (2002); R. K. Puri and S. Kumar, *ibid.* **57**, 2744 (1998); S. Kumar and R. K. Puri, *ibid.* **58**, 2858 (1998); S. Kumar, S. Kumar, R. K. Puri, *ibid.* **78**, 064602 (2008).

[81] S. Kumar, Rajni, and S. Kumar, Phys. Rev. C **82**, 024610 (2010); S. Kumar and S. Kumar, Pramana J. of Physics **74**, 731 (2010); S. Kumar, S. Kumar and R. K. Puri, Phys. Rev. C **81** 014601 (2010); V. Kaur, S. Kumar and R. K. Puri, Phys. Lett. B **679**, 512 (2011).

[82] S. Kumar, PhD. Thesis 1999, Punjab University, Chandigarh (India).

[83] R. K. Puri, C. Hartnack, J. Aichelin, Phys. Rev. C **54**, R28 (1996).

[84] P. B. Gossiaux, R. K. Puri, Ch. Hartnack, and J. Aichelin, Nucl. Phys. A **619**, 379 (1997).

[85] A. A. Amsden, G. F. Bertsch, F. H. Harlow, J. R. Nix, Phys. Rev. Lett. **35**, 905 (1975).

[86] U. Katscher *et al.*, Z. Phys. C **346**, 209 (1993).

[87] W. Schmidt, U. Katscher, B. Waldhauser, J. A. Maruhn, H. Stöcker, and W. Greiner, Phys. Rev. C **47**, 2782 (1993).

[88] C. M. Hung, E. Shuryak, Phys. Rev. C **57**, 1891 (1998).

[89] J. Cugnon, Phys. Rev. C **22**, 1885 (1980).

[90] J. W. Negele, Rev. Mod. Phys. **54**, 913 (1982); F. Sakata, T. Kubo, T. Marumori, K. Iwasawa, Y. Hashimoto, Phys. Rev. C **50**, 138 (1994); D. Lacroix. and P. Chomaz, Phys. Rev. C **58**, 1604 (1998); A. S. Umar and V. E. Oberacker, Phys. Rev. C **74**, 024606 (2006); S. S. Chandel, S. K. Dhiman, R. Shyam, Phys. Rev. C **68**, 054320 (2003)

[91] J. Cugnon and C. Volant, Z. Phys. A **334**, 435 (1989); J. Cugnon, D. Kinet, and J. Vandermeulen, Nucl. Phys. A **379**, 553 (1982); J. Cugnon and D. L. Hote, Phys. Lett. B **149**, 35 (1984); H. Duarte, Phys. Rev. C **75**, 024611 (2007).

[92] G. F. Bertsch and S. Das Gupta, Phys. Rep. **160**, 189 (1988).

[93] W. Bauer, C. Gelbke and S. Pratt, Ann. Rev. Nucl. Part. Sci. **42**, 77 (1992).

[94] J. J Molitoris and H. Stöcker, Phys. Rev C **32**, R346 (1985).

[95] J. Aichelin and G. Bertsch, Phys. Rev. C **31**, 1730 (1985).

[96] C. Gregoire, B. Remaud, F. Sebille, L. Vinet, and Y. Raffray, Nucl. Phys. A **465**, 317 (1987).

[97] C. Gale, G. Bertsch, and S. D. Gupta, Phys. Rev. C **35**, 1666 (1987)

[98] J. Zhang, S. D. Gupta, and C. Gale, Phys. Rev. C **50**, 1617, (1994); V. Greco, A. Guarnera, M. Colonna, and M. D. Toro, Phys. Rev. C **59**, 810 (1999).

[99] Q. Pan and P. Danielewicz, Phys. Rev. Lett. **70**, 2062 (1993);

[100] *Total cross-sectios for reactions of High Energy particles*, edited by A. Baldini, V. Flaminio, W. G. Moorhead, and R. R. O. Morrison (Springer-Verlag, Berlin, 1988).

[101] B. Remaud, C. Grëgoire, F. Sebille, and P. Schuck, Nucl. Phys. A **488**, 423c (1988); M. Farine, T. Sami, B. Remaud, and F. Sebille, Z Phys. A **339**, 363 (1991); L. G. Sobotka, Phys. Rev. C **50**, R1272 (1994).

[102] P. E. Hodgson, *Nuclear Reactions and Nuclear Structure* (Clarendon, Oxford, 1971), Chap. 9.3.

[103] M. Colona *et al.,* in *Critical Phenomena and Collective observables,* edited by S. Costa *et al.,* (World Scientific, Singapore, 1997), p. 369.

[104] A. Bohnet, N. Ohtsuka, J. Aichelin, R. Linden, and A. Faessler, Nucl. Phys. A **494**, 349 (1989); L. Neise, M. Berenguer, C. Hartnack, G. Peilert, H. Stöcker and W. Greiner, Nucl. Phys. A **519**, 375 (1990); M. Berenguer, C. Hartnack, G. Peilert, H. Stocker, W. Greiner, J. Aichelin, and A. Rosenhauer, J. Phys. G: Nucl. and Part. Phys. **18**, 655 (1992).

[105] D. T. Khoa, N. Ohtsuka, A. Faessler, M. A. Matin, S. W. Huang, E. Lehmann, and Y. Lofty, Nucl. Phys. A **542**, 671 (1992); D. T. Khoa, N. Ohtsuka, S. W. Huang, M. Ismail, A. Faessler, M. E. Shabshiry, and J. Aichelin, *ibid.* **529**, 363 (1991); G. Q. Li, D. T. Khoa, T. Maruyama, S. W. Huang, N. Ohtsuka, A. Faessler, and J. Aichelin, *ibid.* **534**, 697 (1991); G. Peilert *et al.*, Mod. Phys. Lett. A **3**, 459 (1988).

[106] J. Aichelin, Phys. Rev. C **33**, 537 (1986); J. Aichelin and H. Stöcker, Phys. Lett. B **163**, 59 (1985).

[107] C. Hartnack and J. Aichelin, J. Phys. G: Nucl. and Part. Phys. **28**, 1649 (2002); *ibid.* **30**, s531 (2004).

[108] R. K. Puri and S. Kumar, Phys. Rev. C **57**, 2744 (1998).

[109] S. Kumar and R.K. Puri, Phys. Rev. C **60**, 054607 (1999); J. Aichelin, A. Rosenhauer, G. Peilert, H. Stoecker, and W. Greiner, Phys. Rev. Lett. **58**, 1926 (1987).

[110] S. Kumar and R. K. Puri, Phys. Rev. C **58**, 320 (1998); S. Kumar, R. K. Puri and J. Aichelin, Phys. Rev. C **58**, 1618 (1998).

[111] G.F. Peaslee *et al.*, Phys. Rev. C **49**, R2271 (1994); K. Hagel *et al.*, Phys. Rev. Lett. **68**, 2141 (1992); J. Hubele *et al.*, *ibid.* **46**, R1577 (1992).

[112] M. Begemann-Blaich *et al.*, Phys. Rev. C **48**, 610 (1993).

[113] N. T. B. Stone *et al.*, Phys. Rev. Lett. **78**, 2084 (1997).

[114] L. Jianye and Z. S. Guang, Z. Phys. A **348**, 31 (1994).

[115] G. Peilert, J. Randrup, H. Stöcker, and W. Greiner, Phys. Lett. B **260**, 271 (1991); G. Peilert *et al.*, Phys. Rev. C **46**, 1457 (1992).

[116] M. Belkacem *et al.*, Phys. Rev. C **58**, 1727 (1998); A. Dumitru, M. Bleicher, S. A. Bass, C. Spieles, L. Neise, H. Stöcker, and W. Greiner, Phys. Rev. C **57**, 3271 (1998)

[117] M. Trefz, A. Faessler, and W. H. Dickhoff, Nucl. Phys. A **443**, 499 (1985); N. Ohtsuka, R. Linden, A. Faessler, and F. B. Malik, Nucl. Phys. A **465**, 550 (1987).

[118] K. A. Waged, Phys. Rev. C **63**, 024618 (2001); J. Phys. G: Nucl. and Part. Phys. **28**, 2951 (2002).

[119] H. Feldmeier and J. Schnack, Prog. Part. Nucl. Phys. **39**, 393 (1997); H. Feldmeier, Nucl. Phys. A **515**, 147 (1990).

[120] A. Ono, H. Horiuchi, T. Maruyama, and A. Ohnishi, Phys. Rev. Lett. **68**, 2898 (1992); A. Ono and H. Horiuchi, Phys. Rev. C **51**, 299 (1995).

[121] A. Ono and H. Horiuchi, Phys. Rev. C **53**, 2958 (1996).

[122] N. Itagaki, S. Aoyama, S. Okabe, K. Ikeda, Phys. Rev. C **70**, 054307 (2004).

[123] M. Papa, T. Maruyama, and A. Bonasera, Phys. Rev. C **64**, 024612 (2001).

[124] R. K. Puri, E. Lehmann, A. Faessler, and S. W. Huang, J. Phys. G: Nucl. and Part. Phys. **21**, 583 (1995); H. Sorge, H. Stocker, and W. Greiner, Ann. Phys. **192**, 266 (1989).

[125] T. Maruyama, S. W. Huang, N. Ohtsuka, G. Q. Li, A. Faessler, and J. Aichelin, Nucl. Phys. A **534**, 720 (1991); T. Maruyama, G. Q. Li, and A. Faessler, Phys. Lett. B **268**, 161 (1991); S. W. Huang, A. Faessler, G. Q. Li, R. K. Puri, E. Lehmann, D. T. Khoa, and M. A. Matin, Phys. Lett. B **298**, 41 (1993).

[126] E. Lehmann, R. K. Puri, A. Faessler, G. Batko, and S. W. Huang, Phys. Rev. C **51**, 2113 (1995); H. Sorge, Phys. Rev. C **52**, 3291 (1995).

[127] Y. Yariv and Z. Fraenkel, Phys. Rev. C **20**, 2227 (1979).

[128] R. K. Puri, N. Ohtsuka, E. Lehmann, A. Faessler, M. A. Matin, D. T. Khoa, G. Batko, and S. W. Huang, Nucl. Phys. A **575**, 733 (1994).

[129] S. Kumar, PhD. Thesis 2010, Thapar University, Patiala (India).

[130] S. A. Bass, C. Hartnack, H. Stocker, and W. Greiner, Z. Phys. A **352**, 171 (1995).

[131] P. Danielewicz and G. F. Bertsch, Nucl. Phys. A **533**, 712 (1991).

[132] J. Cugnon, T. Mizutani, and J. Vandermeulen, Nucl. Phys. A **352**, 505 (1981).

[133] S. Huber and J. Aichelin, Nucl. Phys. A **573**, 587 (1994).

[134] J. Singh and R. K. Puri, *ibid.* **62**, 054602 (2000).

[135] Y. K. Vermani and R. K. Puri, Eur. Phys. Lett. **85**, 62001 (2009).

[136] R. K. Puri and R. K. Gupta, Phys. Rev. C **45**, 1837 (1992); R. K. Puri, M. K. Sharma and R. K. Gupta, Eur. Phys. J. A **3**, 277 (1998); R. K. Puri, P. Chattopadhyay and R. K. Gupta, Phys. Rev. C **43**, 315 (1991); R. Arora, R. K. Puri and R. K. Gupta, Eur. Phys. J. A **8**, 103 (2000); I. Dutt and R. K. Puri, Phys. Rev. C **81**, 047601 (2010); *ibid.* **81**, 044615 (2010); *ibid* **81**, 064608 (2010); R. K. Puri and N. K. Dhiman, Eur. Phys. J. A **23**,429 (2005).

[137] Y. K. Vermani, J. K. Dhawan, S. Goyal, R. K. Puri and J. Aichelin, J. Phys. G **37**, 015105 (2010).

[138] R. K. Puri and J. Aichelin, J. Comp. Phys. **162**, 245 (2000).

[139] H. Sorge, Phys. Rev. Lett. **78**, 2309 (1997); P. Danielewicz, R.A. Lacey, P.-B. Gossiaux, C. Pinkenburg, P. Chung, J. M. Alexander and R. L. McGrath, Phys. Rev. Lett. **81**, 2438 (1998).

[140] G. Q. Li, C. M. Ko and B. A. Li, Phys. Rev. Lett. **74**, 235 (1995); G. Q. Li and C. M. Ko, Nucl. Phys. A **594**, 460 (1995); G. Q. Li and C. M. Ko, Phys. Rev. C **54** 1897 (1996).

[141] D. J. Magestro, W. Bauer and G. D. Westfall, Phys. Rev. C **62**, 041603(R) (2000).

[142] D. J. Magestro, W. Bauer, O. Bjarki , J. D. Crispin, M. L. Miller, M. B. Tonjes, A. M. Vander Molen, G. D. Westfall, R. Pak, E. Norbeck, Phys. Rev. C **61**, 021602(R) (2000).

[143] G. D. Westfall *et al.*, Phys. Rev. Lett. **71**, 1986 (1993).

[144] R. Pak *et al.*, Phys. Rev. C **53**, R1469 (1996). R. Pak *et al.*, Phys. Rev. Lett. **78**, 1022 (1997); *ibid.* **78**, 1026 (1997); R. Pak, PhD. thesis, Michigan State University, 1996.

[145] A. D. Sood and R. K. Puri, Eur. Phys. J. A **30**, 571 (2006); Phys. Rev. C **73**, 067602 (2006); *ibid.* **79**, 064618 (2009); *ibid.* **70**, 034611 (2004).

[146] A. D. Sood and R. K. Puri, Phys. Rev. C **69**, 054612 (2004).

[147] A. D. Sood, R. K. Puri and J. Aichelin, Phys. Lett. B **594**, 260 (2004).

[148] C. Liewen, Z. Fengshou and J. Genming, Phys. Rev. C **58**, 2283 (1998); S. Gautam, A. D. Sood, R. K. Puri, J. Aichelin, Phys. Rev. C **83**, 014603 (2011); *ibid.* **83**, 034606 (2011); S. Goyal and R. K. Puri Nucl. Phys. A **853**, 164 (2011).

[149] B. A. Li and A. T. Sustich, Phys. Rev. Lett. **82**, 5004 (1999).

[150] Y. M. Zheng, C. M. Ko, B. A. Li and B. Zhang, Phys. Rev. Lett. **83**, 2534 (1999).

[151] C. A. Ogilvie *et al.*, Phys. Rev. C **40**, 2592 (1989).

[152] B. Blättel, V. Koch, A. Lang, K. Weber, W. Cassing, U. Mosel, Phys. Rev. C **43**, 2728 (1991).

[153] A. Andronic *et al.*, Phys. Rev. C **67**, 034907 (2003).

[154] V. Ramillien *et al.* (FOPI Collaboration), Nucl. Phys. A **587**, 802 (1995).

[155] G. F. Bertsch, W. G. Lynch and M. B. Tsang, Phys. Lett. B **189**, 384 (1987).

[156] J. Lukasik *et al.* (INDRA and ALADIN Collaboration), Phys. Lett. B **608**, 223 (2005).

[157] W. M. Zhang *et al.*, Phys. Rev. C **42**, R491 (1990).

[158] D. Beavis *et al.*, Phys. Rev. C **45**, 299 (1992).

[159] J. Lukasik and W. Trautmann, Proc. International Nuclear Physics Conference **2**, 513 (2007).

[160] B. Hong *et al.* (FOPI Collaboration), Phys. Rev. C **66**, 034901 (2000).

[161] J. J. Molitoris and H. Stöcker, Phys. Lett. B **162**, 47 (1985).

[162] D. Krofcheck *et al.*, Phys. Rev. C **46**, 1416 (1992).

[163] C. A. Ogilvie *et al.*, Phys. Rev. C **42**, R10 (1990).

[164] W. Bauer, Phys. Rev. Lett. **61**, 2534 (1988).

[165] D. Klakow, G. Welke, and W. Bauer, Phys. Rev. C **48**, 1982 (1993).

[166] H. Zhou, Z. Li, Y. Zhuo, G. Mao, Nucl. Phys. A **580**, 627 (1994).

[167] S. Soff, S. A. Bass, C. Hartnack, H. Stöcker, and W. Greiner, Phys. Rev. C **51**, 3320 (1995).

[168] F. Daffin, K. Haglin, W. Bauer, Phys. Rev. C **54**, 1375 (1996); M. J. Huang *et al.*, Phys. Rev. Lett. **77**, 3739 (1996); S.A. Bass *et al.*, Prog. Part. Nucl. Phys. **41**, 225 (1998).

[169] W. K. Wilson, PhD. thesis, Michigan State University, 1991.

[170] R. K. Gupta, S. Singh, R. K. Puri and W. Scheid, Phys. Rev. C **47**, 561 (1993); R. K. Gupta, S. Singh, R. K. Puri, A. Sandulescu, W. Greiner and W. Scheid, J. Phys. G: Nucl. and Part. Phys. **18**, 1533 (1992); S. S. Malik, S. Singh, R. K. Puri, S. Kumar, R. K. Gupta, Pramana J. of Physics **32** 419 (1989); R. K. Puri, S. S. Malik and R. K. Gupta, Eur. Phys. Lett.**9**, 767 (1989); R. K. Puri and R. K. Gupta J. Phys. G: Nucl. and Part. Phys. **18**, 903 (1992); R. K. Gupta, M. Balasubramaniam, R. K. Puri and W. Scheid, J. Phys. G: Nucl. and Part. Phys. **26** L23 (2000).

[171] Z. Y. He *et al.*, Nucl. Phys. A **598**, 248 (1996).

[172] J. P. Sullivain *et al.*, Phys. Lett. B **249**, 8 (1990).

[173] D. Krofcheck *et al.*, Phys. Rev. C **43**, 350 (1991).

[174] D. Cussol *et al.* (INDRA Collaboration), Phys. Rev. C **65**, 044604 (2002).

[175] R. Chugh and R. K. Puri, Int. J. Mod. Phys. E, **19**, 2009 (2010).

[176] S. Gautam, R. Chugh, A. D. Sood, R. K. Puri, Ch. Hartnack and J. Aichelin, J. phys. G: Nucl. Part. Phys. **37**, 085102 (2010).

[177] S. Kumar and S. Kumar, Chin. Phys. Lett. **27**, 062504 (2010).

[178] Y. K. Vermani and R. K. Puri, J. Phys. G **36**, 105103 (2009).

[179] V. Kaur and S. Kumar, Pramana J. Phys. **78**, 237 (2012); S. Gautam, Eur. Phys. J. A **48**, 1 (2012).

[180] F. H. Liu, Y. Yuan, D. H. Zhang, H. L. Li, Acta Phys. Pol. B **39**, 1969 (2008).

[181] B. A. Li and D. H. E. Gross, Nucl. Phys. A **554**, 257 (1993); H. M. Xu, C. A. Gagliardi, R. E. Tribble, and C. Y. Wong, Nucl. Phys. A **569**, 575 (1994); V. de la Mota, F. Sebille, M. Farine, B. Remaud, and P. Schuck, *ibid.* **46**, 677 (1992).

[182] J. Aichelin, A. Rosenhauer, G. Peilert, H. Stoecker, and W. Greiner, Phys. Rev. Lett. **58**, 1926 (1987); T. Maruyama, K. Niita, T. Maruyama, and A. Iwamoto, Prog. Theor. Phys. **98**, 87 (1997).

[183] B. Jakobsson *et al.*, Nucl. Phys. A **509**, 195 (1990).

[184] M. Begemann-Blaich *et al.*, Phys. Rev. C **58**, 1639 (1998).

[185] S. C. Jeong *et al.*, Nucl. Phys. A **604**, 208 (1996).

[186] B. A. Li, L. W. Chen, C. M. Ko, Phys. Rep. **464**, 113 (2008).

[187] D. T. Khoa, N. Ohtsuka, M. A. Matin, A. Faessler, S. W. Huang, E. Lehmann, R. K. Puri, Nucl. Phys. A **548**, 102 (1992).

[188] W. J. Llope *et al.*, Phys. Rev. C **51**, 1325 (1995).

[189] H. Stöcker, J. A. Maruhn and W. Greiner, Phys. Rev. Lett. **44**, 725 (1980).

[190] H. Stöcker, L. P. Csernai, G. Graebner, G. Buchwald, H. Kruse, R. Y. Cusson, J. A. Maruhn, W. Greiner, Phys. Rev C **25**, 1873 (1982).

[191] Ch. Hartnack *et al.*, Nucl. Phys. A **538**, 53 (1992); Mod. Phys. Lett. **A9**, 1151 (1994); C. Hartnack, J. Jaenicke, L. Sehn, H. Stöcker, J. Aichelin, Nucl. Phys. A **580**, 643 (1994).

[192] J. Y. Ollitrault, Phys. Rev. D **48**, 1132 (1993).

[193] J. Y. Ollitrault, Phys. Rev. D **46**, 229 (1992); A. M. Poskanzer and S. A. Voloshin, Phys. Rev. C **58**, 1671 (1998).

[194] S. Voloshin and Y. Zhang, Z. Phys. C **70**, 665 (1996).

[195] Y. G. Ma, G. H. Liu, X. Z. Cai, D. Q. Fang, W. Guo, W. Q. Shen, W. D. Tian and H. W. Wang, Phys. Rev. C **85**, 024618 (2012).

[196] P. Declan and G. Charles, Phys. Rev. C **65**, 064611 (2002).

[197] L. P. Csernai and D. Röhrich, Phys. Lett. B **458**, 454 (1999); C. M. Hung and E. V. Shuryak, Phys. Rev. Lett. **75**, 4003 (1995); D. H. Rischke, Nucl. Phys. A **610**, 88C (1996); H. Heiselberg and A. M. Levy, Phys. Rev. C **59**, 2716 (1999); J. Brachmann, S. Soff, A. Dumitru, H. Stöcker, J. A. Maruhn, W. Greiner, L. V. Bravina, and D. H. Rischke, Phys. Rev. C **61**, 024909 (2000); J. Brachmann, A. Dumitru, H. Stöcker, and W. Greiner, Eur. Phys. J. A **8**, 549 (2000). B. Zhang, M. Gyulassy, and C. M. Ko, Phys. Lett. B **455**, 45(1999). M. Bleicher and H. Stöcker, Phys. Lett. B **526**, 309 (2002).

[198] J. Gosset, H. H. Gutbrod, W. G. Meyer, A. N. Poskanzer, A. Sandoval, R. Stock, G. D. Westfall, Phys. Rev. C **16**, 629 (1977); J. Gosset *et al.*, Phys. Rev. Lett. **62**, 1251 (1989).

[199] R. E. Renfordt *et al.*, Phys. Rev. Lett. **53**, 763 (1984).

[200] Zi.-W. Lin and C. M. Ko, Phys. Rev. C **65**, 034904 (2002).

[201] R. J. M. Snellings (STAR Collaboration), Nucl. Phys. A **698**, 193 (2002).

[202] A. Andronic *et al.* (FOPI Collaboration), Nucl. Phys. A **679**, 765 (2001); Phys. Lett. B **612**, 173 (2005).

[203] P. Crochet *et al.* (FOPI Collaboration), Nucl. Phys. A **624**, 755 (1997).

[204] H. Sorge, Phys. Rev. C **52**, 3291 (1995).

[205] D. Teaney, J. Lauret, and E. V. Shuryak, Phys. Rev. Lett. **86**, 4783 (2001); Nucl. Phys. A **698**, 479 (2002).

[206] K. H. Ackermann *et al.* (STAR Collaboration), Phys. Rev. Lett. **86**, 402 (2001).

[207] G. Roland *et al.* (PHOBOS Collaboration), Nucl. Phys. A **698**, 54 (2002); I. Park *et al.* (PHOBOS Collaboration), *ibid.* **698**, 564 (2002).

[208] M. Colona, M. D. Toro, G. Ferini, and V. Greco, *Catania workshop on nucleon and neutrino astrophysics*, 15-16 Feb., (2007); M. Di Toro, S. J. Yennello, and B. -A. Li, Eur. Phys. J. A **30**, 153 (2006).

[209] T. Z. Yan, Y. G. Ma, X. Z. Cai, D. Q. Fang, W. Guo, C. W. Ma, W. Q. Shen, W. D. Tian, K. Wang, Chin. Phys. **16**, 2676 (2007).

[210] Y. Zhang and Z. Li, Phys. Rev. C **74**, 014602 (2006).

[211] H. W. Barz *et al.*, Nucl. Phys. A **548**, 427 (1992).

[212] M. B. Tsang, Y. Zhang, P. Danielewicz, M. Famiano, Z. Li, W. G. Lynch, A. W. Steiner, Phys. Rev. Lett. **102**, 122701 (2009).

[213] J. Hubele *et al.*, Phys. Rev. C **46**, R1577 (1992).

[214] F. H. Liu, Q. W. Lü, B. C. Li and R. Bekmirzaev, Chin. J. Phys. **49**, 601 (2011).

[215] S. Fredriksson, G. Eilam, G. Berlad, L. Bergström, Phys. Rep. **144**, 187 (1987).

[216] R. T. de Souza *et al.*, Phys. Lett. B **268**, 6 (1991).

[217] C. Williams *et al.*, Phys. Rev. C **55**, R2132 (1997); K. Hagel *et al.*, Phys. Rev. Lett. **68**, 2141 (1992); S. R. Souza, L. de Paula, S. Leray, J. Nemeth, C. Ngo, and H. Ngo, Nucl. Phys. A **571**, 159 (1994).

[218] M. B. Tsang *et al.*, Phys. Rev. Lett. **71**, 1502 (1993).

[219] A. S. Botvina, N. Buyukcizmeci, M. Erdogan, J. Lukasik, I. N. Mishustin, R. Ogul, W. Trautmann, Phys. Rev. C **74**, 044609 (2006).

[220] R. Ogul *et al.*, Phys. Rev. C **83**, 024608 (2011).

[221] J. Pochodzalla *et al.*, Phys. Rev. Lett. **75**, 1040 (1995).

[222] A. S. Botvina and I. N. Mishustin, Phys. Lett. B **294**, 23 (1992); B. A. Li, A. R. DeAngelis, and D. H. E. Gross, Phys. Lett. B **303**, 225 (1993); A. H. Raduta and A. R. Raduta, Phys. Rev. C **61**, 034611 (2000).

[223] H. F. Zhang, U. Lombardo and W. Zuo, Phys. Rev. C **82**, 015805 (2010).

[224] H. F. Zhang, Z. H. Li, U. Lombardo, P. Y. Luo, F. Sammarruca and W. Zuo, Phys. Rev. C **76**, 054001 (2007).

[225] G. C. Yong, W. Zuo and X. C. Zhang, Phys. Lett. B **705**, 240 (2011).

[226] R. Nebauer et al., Nucl. Phys. A **658**, 67 (1999).

[227] H. Feldmeier and J. Schnack, Rev. Mod. Phys. **72**, 655 (2000).

[228] T. Maruyama, K. Niita and A. Iwamoto, Phys. Rev. C **53**, 297 (1996).

[229] T. Maruyama, A. Bonasera, M. Papa and S. Chiba, Eur. Phys. J. A **14**, 191 (2002).

[230] W. Trautmann *et al.*, Int. J. Mod. Phys. E **17**, 1838 (2008).

[231] C. Sfienti *et al.* (ALADIN Collaboration), Phys. Rev. Lett. **102**, 152701 (2009).

[232] A. S. Botvina, O. V. Lozhkin and W. Trautmann, Phys. Rev. C **65**, 044610 (2002).

[233] P. Bonche, S. Levit and D. Vautherin, Nucl. Phys. A **436**, 265 (1985).

[234] J. Besprosvany and S. Levit, Phys. Lett. B **217**, 1 (1989).

[235] H. Q. Song and R. K. Su, Phys. Rev. C **44**, 2505 (1991).

[236] M. Baldo, L. S. Ferreira and O. E. Nicotra, Phys. Rev. C **69**, 034321 (2004).

[237] D. H. E. Gross, Zhang Xiao-ze and Xu Shu-yan, Phys. Rev. Lett. **56**, 1544 (1986).

[238] P. Wang, D. B. Leinweber, A. W. Thomas, A. G. Williams, Nucl. Phys. A **748**, 226 (2005).

[239] J. B. Natowitz, K. Hagel, R. Wada, Z. Majka, P. Gonthier, J. Li, N. Mdeiwayeh, Phys. Rev. C **52**, R2322 (1995).

[240] J. B. Natowitz, R. Wada, K. Hagel, T. Keutgen, M. Murray, A. Makeev, L. Qin, P. Smith, C. Hamilton, Phys. Rev. C **65**, 034618 (2002).

[241] N. Wang, Z. Li and X. Wu, Phys. Rev. C **65**, 064608 (2002).

[242] Ben-Hao Sa, Yu-Ming Zheng and Xiao-Ze Zheng, Int. J. Mod. Phys. A **5**, 843 (1990); Y. M. Zheng, H. Massmann, S. Y. Xu, D. H. E. Gross, X. Z. Zhang, Z. Q. Lu and B. H. Sa, Phys. Lett. B **194**, 183 (1987); D. H. E. Gross, Y. M. Zheng and H. Massmann, Phys. Lett. B **200**, 397 (1988).